

FAU-PI1-DISS-08-001  
FAU-ECAP-DISS-08-001

# Experimental Studies within ANTARES towards Acoustic Detection of Ultra-High Energy Neutrinos in the Deep-Sea

Den Naturwissenschaftlichen Fakultäten  
der Friedrich-Alexander-Universität Erlangen-Nürnberg  
zur  
Erlangung des Doktorgrades



vorgelegt von  
Kay Graf  
aus Fürth

Als Dissertation genehmigt von den Naturwissenschaftlichen Fakultäten  
der Universität Erlangen-Nürnberg

Tag der mündlichen Prüfung:	7. Mai 2008
Vorsitzender der Promotionskommission:	Prof. Dr. Eberhard Bänsch
Erstberichterstatter:	Prof. Dr. Ulrich F. Katz
Zweitberichterstatter:	Prof. Dr. Klaus Helbing

# Contents

<b>1</b>	<b>Introduction</b>	<b>1</b>
<b>I</b>	<b>Acoustic Detection of Ultra-High Energy Neutrinos</b>	<b>3</b>
<b>2</b>	<b>The Ultra-High Energy Regime</b>	<b>5</b>
2.1	Cosmic Ray Flux . . . . .	6
2.2	UHE Neutrinos . . . . .	7
2.3	Acoustic Detection . . . . .	9
<b>3</b>	<b>Experimental Verification of the Thermo-Acoustic Sound Generation</b>	<b>11</b>
3.1	The Thermo-Acoustic Model . . . . .	11
3.2	Comparison of Measured Signals to Simulation . . . . .	12
3.3	Analysis Results . . . . .	14
3.3.1	Variation of the Sensor Position and Pulse Energy . . . . .	14
3.3.2	Variation of the Temperature . . . . .	15
<b>4</b>	<b>Simulation of Acoustic Neutrino Detectors</b>	<b>17</b>
4.1	Calculation of the Expected Signal . . . . .	17
4.2	Signal Propagation . . . . .	19
4.3	Sensitivity Studies of Acoustic Detectors . . . . .	20
4.3.1	Background for Acoustic Neutrino Detection . . . . .	20
4.3.2	Detector Sensitivity . . . . .	23
<b>II</b>	<b>ANTARES and AMADEUS</b>	<b>27</b>
<b>5</b>	<b>Acoustic Particle Detection in ANTARES</b>	<b>29</b>
5.1	The ANTARES Experiment . . . . .	29
5.1.1	Physics Program . . . . .	29
5.1.2	Detector Design . . . . .	30
5.2	Acoustic Particle Detection in ANTARES . . . . .	35
5.2.1	The AMADEUS-0 Project . . . . .	36

<b>6</b>	<b>The AMADEUS Project</b>	<b>39</b>
6.1	The AMADEUS Setup . . . . .	39
6.1.1	Acoustic Sensors . . . . .	40
6.2	The AcouADC Board . . . . .	44
6.2.1	Analogue part . . . . .	46
6.2.2	Digital part . . . . .	48
6.3	Data-taking Scheme and Standard Settings . . . . .	48
<b>III</b>	<b>Characterisation of the AcouADC Board</b>	<b>51</b>
<b>7</b>	<b>Calibration Setup</b>	<b>53</b>
7.1	Calibration Setup . . . . .	53
7.2	Input Stimuli . . . . .	55
7.2.1	$\delta$ -Pulse . . . . .	55
7.2.2	Gaussian White Noise . . . . .	56
7.2.3	Sine Waveform . . . . .	57
<b>8</b>	<b>System Transfer Functions</b>	<b>59</b>
8.1	ADC Transfer Curve . . . . .	59
8.2	Frequency Response of the Filter . . . . .	63
8.3	Gain Settings . . . . .	68
<b>9</b>	<b>System Characteristics</b>	<b>71</b>
9.1	Dynamic Range and Frequency Distortion . . . . .	71
9.2	Inherent Noise and Channel Crosstalk . . . . .	73
9.3	Electromagnetic Compatibility . . . . .	76
9.4	System Stability . . . . .	78
9.5	System Response to Acoustic Signals . . . . .	79
9.5.1	Bipolar Pulse Input . . . . .	79
9.5.2	Gaussian Noise Input . . . . .	81
<b>IV</b>	<b>Data Taking with the AMADEUS System</b>	<b>83</b>
<b>10</b>	<b>System Characteristics and Performance in the Laboratory</b>	<b>85</b>
10.1	System Stability . . . . .	85
10.2	Inherent Noise . . . . .	87
10.2.1	Equivalent Noise Level . . . . .	87
10.2.2	Noise Power Spectra . . . . .	88

---

<b>11 Commissioning of AMADEUS on IL07</b>	<b>91</b>
11.1 Determination of Standard Settings . . . . .	92
11.2 Comparison of Sensors . . . . .	93
11.3 System Stability . . . . .	95
<b>12 Analysis of Sea Data</b>	<b>97</b>
12.1 Transient Signals . . . . .	97
12.1.1 Acoustic Positioning Signals . . . . .	97
12.1.2 Exemplary Transient . . . . .	100
12.2 Ambient Noise . . . . .	101
12.2.1 Noise Spectra . . . . .	102
12.2.2 Correlations in Ambient Noise . . . . .	104
12.2.3 Correlation of the Noise Level with Weather Conditions . . . . .	106
<b>13 Summary and Conclusion</b>	<b>113</b>
<b>14 Zusammenfassung</b>	<b>117</b>
<b>A Distribution of Gain Factors</b>	<b>125</b>



# Chapter 1

## Introduction

Astroparticle physics studies elementary particles of astronomical origin (e.g. *cosmic rays*, *gamma rays* and *neutrinos*) employing detection methods developed in the field of particle physics, e.g. for detectors at particle accelerators, but also using new detection methods. The major questions of the origin and the acceleration processes of *cosmic rays* in the ultra-high energy regime, surpassing the EeV scale, have not been successfully answered even after almost a century since V.F. Hess's discovery of what was at that time called *Höhenstrahlung*. The detection of cosmogenic neutrinos in the same energy range would open a new window to study the highest-energy phenomena in the cosmos and thus provide additional information from the less well explored weak sector of the Standard Model.

For the exploration of the ultra-high energy regime with neutrinos, new detection techniques and new detector designs have to be developed. It is most probably not feasible to scale up current or planned neutrino telescopes to the instrumented volumes of tens of cubic-kilometres needed to study ultra-high energy neutrinos. These are produced e.g. in *Active Galactic Nuclei* or via the *Greisen-Zatsepin-Kuzmin* effect in the interaction of protons of extreme energies with the cosmic microwave background. An *acoustic detection method* is a promising option for future neutrino deep-sea telescopes operating in this energy regime. Acoustic neutrino detection utilises the effect that a cascade evolving from a neutrino interaction generates a coherently emitted sound wave with main frequency components between 1 and 50 kHz with a peak emission at 10 kHz. This approach allows for a wider sensor spacing and possibly simpler sensor design and read-out electronics than the currently used optical Cherenkov technique.

Presented in this work is an experimental study on the feasibility of detecting ultra-high energy neutrinos with an acoustic detector in sea water. A short motivation of the physics case for such a detector is given. After this an experimental verification of the *thermo-acoustic model* which describes the signal generation mechanism is presented. Based on this sound generation mechanism, the sound wave produced in a neutrino interaction can be simulated and the response of an acoustic detector can be evaluated. The major conclusion of simulation studies in this field is the primary dependency of the detection efficiency on the sensor spacing in the detector and on the unambiguous identification of the neutrino signal in the acoustic background of the sea down to small signal amplitudes.

To study the acoustic detection method in an adapted array of sensors with characteristics

comparable to what would be needed in a possible future detector, the *AMADEUS*<sup>1</sup> project was initiated with the objective of installing 36 acoustic sensors within the *ANTARES*<sup>2</sup> neutrino telescope in the Mediterranean Sea. The aim of this project is to contribute to the question of the feasibility of an acoustic detector, especially by assessing the rate of irreducible background events and the threshold to detect the acoustic signal of neutrinos in the prevailing ambient noise conditions. The inter-sensor spacing in the setup ranges from below 1 m in 6 local sensor clusters to 350 m between individual clusters. With this setup also the ambient noise in the deep-sea, the behaviour of transient signals and correlation lengths of the background will be studied over several years of continuous data taking. This comprehensive set of data allows also for the study of the necessarily highly efficient on- and off-line data filtering techniques. As many of the recorded signals will be of technical, anthropogenic or marine life origin, an investigation of the sea acoustical environment with no relevance to acoustic neutrino detection will be also possible. The operation within a running neutrino telescope permits to study a possible hybrid detection method, using both the optical and acoustical technique at the same time.

One essential part of the project is the off-shore data-acquisition hardware, whose development, calibration and performance is presented. The hardware is implemented in form of the *AcouADC board* which is designed to match the requirements of acoustic particle detection with a flexible system. The board amplifies, filters and digitises the signal of the acoustic sensors and sends the data to shore via the *ANTARES* data-acquisition hardware. Many settings of the board in amplification, sampling rate and digitisation range are adjustable from the on-shore detector control, to study acoustic signals and ambient noise with a huge dynamic range both in amplitude and frequency. A programmable processor on the board allows for off-shore data preprocessing. Due to the small input signals down to the  $\mu\text{V}$  range, the board has a low inherent noise level. The design, calibration and characterisation of the board is described as well as tests showing that after calibration of the data the uncertainties due to the processing in the board are insignificant. It is also shown that the system can be operated stably and without degeneration due to external noise over large times scales, which is essential as the DAQ hardware is not accessible during its years of operation in the deep-sea.

In December 2007 the first phase of the *AMADEUS* project successfully started to take data with 18 sensors on three local clusters. An analysis of the data recorded in the first month of data taking is presented. The system was found to operate stably and to be able to take data continuously over the whole period. With these data the potential of the system to give clues about the major questions in acoustic particle detection is proven on exemplary topics.

A detailed summary and conclusion of the experimental studies performed in this work are given at the end of this work (in Chap. 13 and also in more detail in German in Chap. 14).

---

<sup>1</sup>Abbr. for *ANTARES Modules for Acoustic DEtection Under the Sea*.

<sup>2</sup>Abbr. for *Astronomy with a Neutrino Telescope and Abyss environmental RESearch*.



## **Part I**

# **Acoustic Detection of Ultra-High Energy Neutrinos**



## Chapter 2

# The Ultra-High Energy Regime

Even though almost a century has passed since they were discovered by V.F. Hess in 1912 [1], *cosmic rays*<sup>1</sup> still have not unambiguously revealed their origins, composition and acceleration mechanisms. The cosmic ray spectrum measured at Earth follows a power law behaviour for energies above  $10^{10}$  eV with a spectral index of  $\approx -3$ , particles are detected up to energies exceeding  $10^{20}$  eV. Charged cosmic rays (especially protons and nuclei) with energies below  $10^{11}$  eV can be detected and identified with magnetic spectrometers in balloons or space-crafts above the atmosphere. For higher energies ground based arrays have to be used due to the diminishing flux and particle identification becomes complicated. For energies below  $10^{18}$  eV the charged cosmic rays lose all pointing accuracy due to deflection in magnetic fields in the galaxy. Although there are many open questions concerning cosmic rays in the energy region below  $10^{18}$  eV, like the composition, the point of take-over of extra-galactic sources, etc., it seems to be justified to claim galactic supernovae and their remnants, respectively, as their sources [2,3]. However, at ultra-high energies (*UHE*) exceeding  $10^{18}$  eV even the sources are not known unambiguously – although there are indications that they are *Active Galactic Nuclei* (*AGN*) [4]. The paths of charged cosmic rays through the cosmos are almost straight for these energies [5]. Protons at that energies interact on their propagation via the *Greisen-Zatsepin-Kuzmin* (*GZK*) [6,7] effect, producing amongst other particles also neutrinos.

Thus, in interactions during the acceleration at the sources and in the propagation of cosmic ray primaries – especially protons – the production of a significant flux of ultra-high energy neutrinos is expected. Taking this into account, together with their properties as weakly interacting, uncharged and almost massless ( $m_\nu < 1$  eV [8]) elementary particles<sup>2</sup>, those neutrinos provide a unique probe for the mechanisms acting in the universe at extreme energies. The detection of neutrinos in that energy range could lead to unmatched insights to the question of the sources of UHE cosmic rays and their propagation through the universe.

---

<sup>1</sup>The term *cosmic rays* comprises elementary particles (both charged and uncharged) and nuclei originating in the cosmos and reaching the Earth.

<sup>2</sup>As a consequence neutrinos virtually do not interact in their propagation and are not deflected.

## 2.1 Cosmic Ray Flux

In the ultra-high energy regime above  $10^{18}$  eV, the spectrum of charged cosmic rays shows two distinct features deviating from the overall power law with a spectral index of  $\approx -3$ : a dip starting at just below  $10^{18}$  eV and a steepening above  $10^{19}$  eV. The dip can be interpreted as the signature of a transition to an extra-galactic source population, but also other interpretations can be found. For energies above  $\approx 10^{19.5}$  eV the shape of the flux is not unambiguously determined, mainly due to the extremely low event rate of the order of 1 per  $\text{km}^2$  and century. The Pierre Auger Collaboration, for example, rejects with a  $6\sigma$  significance that the cosmic ray spectrum continues beyond  $10^{19.5}$  eV with the same spectral index of  $-2.62 \pm 0.03 \pm 0.02$  (stat./syst.) as on the rising edge of the dip from  $10^{18.6}$  eV to  $10^{19.5}$  eV [9] (cf. Fig. 2.1(a)). Thus, even if no spectral index is published, this experiment sees a significant reduction in the flux above  $\approx 30$  EeV. The HiRes Collaboration claims a steepening from a spectral index of  $-2.81 \pm 0.03$  to  $5.1 \pm 0.7$  at a break point of  $10^{19.8}$  eV with a  $5\sigma$  significance [10] (cf. Fig. 2.1(b)).

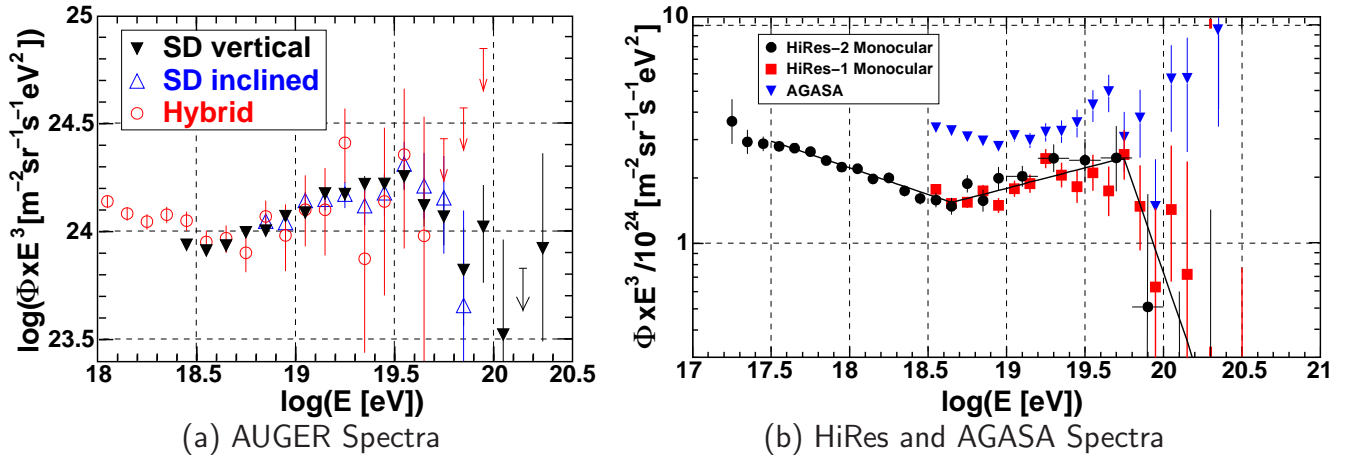


**Figure 2.1:** The highest energies in the cosmic ray spectrum as measured by the AUGER experiment (a) and in the two phases of the HiRes experiment (*HiRes-1*, *HiRes-2*) compared to the AGASA results (b). The Pierre Auger Observatory measures extensive air showers with surface detectors (*SD*) for vertical and inclined showers and in a hybrid detection mode (*SD* and fluorescence measurements, *Hybrid*). In the figures adapted from [9] and [10], respectively, the flux is multiplied by the energy to the power of three.

The HiRes Collaboration identifies this steepening with an effect proposed in 1966 by Greisen [6] Zatsepin and Kuzmin [7], who stated that cosmic ray protons with energies exceeding 50 EeV should interact with the cosmic microwave background (*CMB*) and produce mostly the excited proton state  $\Delta^+(1232)$ . This resonance decays almost exclusively into pions whereby charged pions among them subsequently decay into UHE neutrinos (cf. next section).

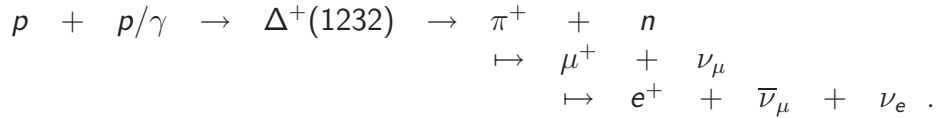
The existence of the GZK effect is under debate especially as there is no hint for it in the data of the AGASA experiment [11]. However, not only the measured spectrum but also correlation studies of cosmic rays with nearby extra-galactic objects conducted by the AUGER

collaboration [4] (cf. next section) hint towards the existence of this effect and thus towards the production of GZK neutrinos.

Caution has to be applied to the interpretation of the results as at those energies the flux of cosmic rays is so feeble that even the largest experiment – the Pierre Auger Observatory, which covers an area of 3000 km<sup>2</sup> – has only observed about 50 events above 10<sup>19.6</sup> eV in over 3 years of data-taking. Additionally the systematic uncertainty in the estimation of the energy of the cosmic ray primary is high, as it has to be derived from simulation of the complex shower evolution in the atmosphere. As pointed out e.g. in [12] by allowing for a systematic shift in energy of the order of 25%, the spectra measured by AGASA, Hi-Res and Auger can be brought into close agreement. Such an energy shift is of the same order as e.g. the systematic uncertainty in the energy scale of 22%, stated by AUGER [9].

## 2.2 UHE Neutrinos

As elaborated in the last section, a flux of UHE cosmogenic neutrinos is guaranteed if the GZK effect exists. Theoretical predictions of the flux of GZK neutrinos are, as well as that of neutrinos from other sources, shown in Fig. 2.3. The major production mechanisms for UHE neutrinos is via a proton/proton (hadron) or proton/gamma interaction, a delta resonance and a subsequent pion and lepton decay:



This neutrino production mechanism holds for most bottom-up scenarios, not only in the propagation of the cosmic rays through the universe, but also at the sources, where cosmic ray primaries are accelerated from low energies and interact with the photon field or hadrons in or near these accelerators. One of the prime candidates of extra-galactic sources of UHE cosmic rays and thus neutrinos are *Active Galactic Nuclei (AGN)*. AGNs [13] are galaxies that are active in the sense that very high energy output is emitted from a relatively small volume at the centre of the galaxy. The centre is assumed to be formed by a super massive black hole (10<sup>7</sup> – 10<sup>9</sup> solar masses), accreting matter from its host galaxy. In this extremely energetic environment – especially in jets associated with the accretion – particles might be accelerated to ultra-high energies by Fermi acceleration [14] in consecutive shock fronts.

Recent observations by the Pierre Auger Collaboration [4] found an anisotropy in the arrival direction of the cosmic rays of highest-energy. The arrival directions are found to be correlated with the position of AGNs with a distance below 100 Mpc, with an angular separation between event and AGN position with less than 6°. The strongest correlation was found for energies above 57 EeV (10<sup>19.8</sup> eV). A sky map with the resulting 27 events of highest energies is shown in Fig. 2.2, where the correlation of the reconstructed event directions with the super-galactic plane is clearly observable. Thus, the events are considered to be of extra-galactic origin, the more as no correlation to the galactic plane is observable.

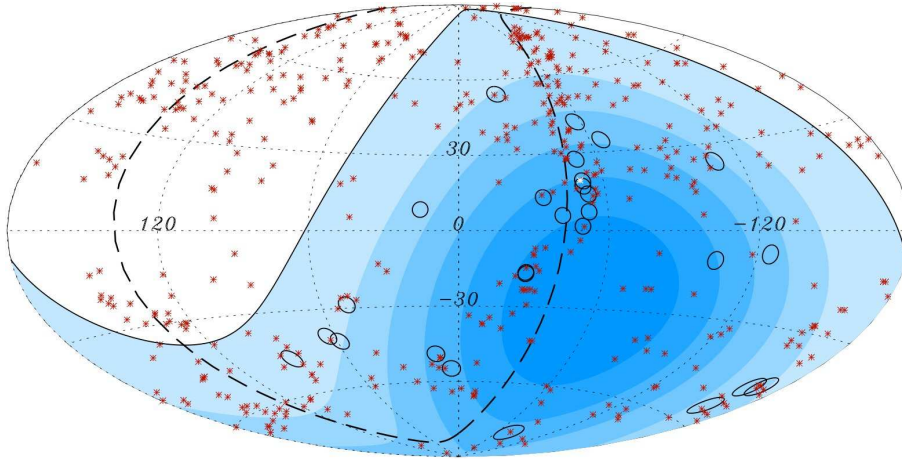


**Figure 2.2:** Sky map in galactic coordinates of cosmic rays detected by the Pierre Auger Observatory. Positions of AGNs with distances lower than 75 Mpc are shown as red asterisks (white asterisk for Centaurus A, one of the closest AGNs) and the arrival directions of the 27 cosmic rays with the highest energies are marked with circles of radius  $3.1^\circ$  around the reconstructed direction. The super-galactic plane is marked by the dashed line and the field of view of the observatory by the solid one, the relative exposure is colour-coded in blue. Figure from [4].

Caution has to be applied in the interpretation of the observed correlation as the analysis is not totally unbiased. However, the observation is a clear indication that those cosmic rays either come from AGN or other (unknown) objects with a similar spatial distribution. The observation is also consistent with the GZK effect as the correlation is seen to increase abruptly at energies above  $10^{19.8}$  eV – the point where the flux of cosmic rays reduces substantially, as seen in the last section. That suggests that the cosmic rays of highest energies are indeed protons from nearby, but extra-galactic, sources.

Thus at both the source and the propagation of cosmic rays at the highest energies neutrinos are produced. A significant neutrino flux is virtually guaranteed from the GZK effect and if UHE neutrinos are produced in the surrounding of AGNs it would be possible to search for those objects even beyond the GZK horizon<sup>3</sup>. Thus the detection and investigation of ultra-high energy cosmogenic neutrinos could lead to a new opening to the almost 100 years old question of the origin of cosmic rays. Also due to their unique features – production in or very close to the source and almost unhindered propagation out of them – neutrinos give tremendous insights into the sources and the production/acceleration mechanisms therein. This is the basic idea of the multi-messenger approach in astroparticle physics, where different types of particles (messengers) are used to study the same objects and mechanisms in it, to gain information which one type alone cannot provide.

<sup>3</sup>Defined in [4] to be 200 Mpc at energies above 60 EeV.

However, there are a lot of additional models predicting ultra-high energy neutrinos also from other sources which have not been described here. An overview of the neutrino fluxes from those models is shown in Fig. 2.3.

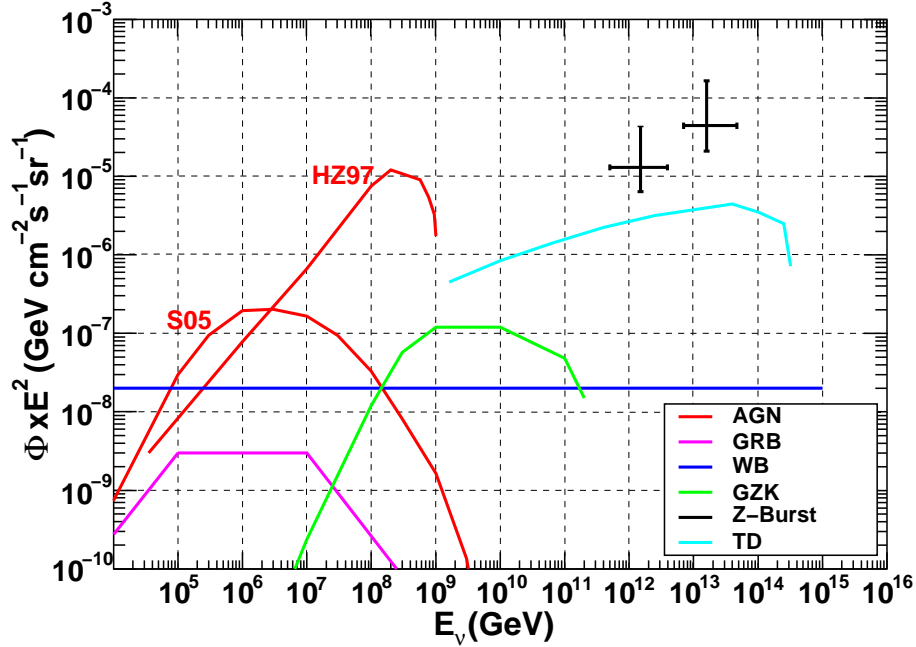


**Figure 2.3:** Predictions of the all flavour flux of cosmogenic neutrinos spanning energies from  $10^{13}$  to  $10^{25}$  eV ( $10^4$  to  $10^{16}$  GeV). Sources included are AGNs, GRBs, neutrinos from the GZK process, Z-Bursts and top-down scenarios (TD). For comparison the Waxman-Bahcall (WB) upper limit is shown. The figure is adapted from [15], where the various theoretical models are explained further.

## 2.3 Acoustic Detection

As motivated in the last sections, major questions in the ultra-high energy regime of cosmic rays are still not answered satisfactorily. The detection of neutrinos in that energy range would open a new window to study the acceleration and interaction mechanisms of the protons and nuclei and therefore could provide unchallenged information from the less well explored weak sector in the Standard Model.

However, the detection of these UHE neutrinos marks an experimental challenge as new detection methods and detector designs have to be devised to study the small fluxes expected e.g. from the models displayed in Fig. 2.3. Neutrino telescopes that are currently operating or planned (cf. Chap. 5) collect the Cherenkov light of neutrino interaction secondaries and analyse it to deduce the energy and arrival direction of the primary. These are not easily – if at all – scalable to the required volumina of more than  $10 \text{ km}^3$  to detect a significant rate of UHE neutrinos and furthermore technically complicated and thus cost intensive in construction.

In this work an acoustic detection method is presented, which is a promising option for future neutrino telescopes operating at energies above 100 PeV. This method is investigated in the medium of sea water but it is also applicable in ice or salt. Other options are studied world wide as well, e.g. based on the measurements of radio emission from neutrino induced cascades<sup>4</sup>. The acoustic method is based on the effect that a cascade evolving from a neutrino interaction generates a sound wave. Two major advantages over the optical neutrino telescopes make this method worth studying. The first one is the fact that the attenuation length, which is approximately one order of magnitude higher for acoustic signals of cascades than for the Cherenkov light ( $\approx 1$  km to  $\approx 100$  m, when taking into account the main frequency band of the emissions). The second advantage is the much simpler sensor design and read-out electronics, caused by the acoustic nature and the longer time scales of the signals: in the  $\mu$ s range for acoustics and in the ns range for optics. This allows for the on-line implementation of advanced signal processing techniques. Efficient data filters are essential, as the signal amplitude is relatively small compared to the acoustic background in the sea, which complicates the unambiguous determination of the signal.

Intensive studies are performed all over the world to explore the potential of this technique. Therefore it is only possible to present the basic concepts of that detection method, while going into more detail, where studies were conducted within the limits of the presented work. All presented topics are viewed in the framework of the integration of acoustic sensors into the ANTARES optical neutrino telescope in the Mediterranean Sea – the AMADEUS project – to study the feasibility of a future large-scale acoustic neutrino detector.

---

<sup>4</sup>An overview of the current activities for ultra-high energy neutrino detection can be found in [16,17].



## Chapter 3

# Experimental Verification of the Thermo-Acoustic Sound Generation

The first step when conducting studies towards the acoustic detection of ultra-high energy neutrinos is the verification and understanding of the *thermo-acoustic model*, which describes the generation mechanism that is expected to lead to a detectable acoustic pulse. Towards this goal, experiments to investigate the sound generation in fresh water caused by the energy deposition of pulsed particle and laser beams have been performed by the Erlangen Acoustics group at a proton accelerator and an infrared laser facility at the ECAP<sup>1</sup>. The used proton beam had particle energies of 177 MeV leading to a Bragg peak at a penetration depth of 22 cm, the laser beam had a wavelength of 1064 nm and thus an attenuation length in water of 6.0 cm. Typical beam diameters were in the order of 1 cm. These parameters permitted a compact setup of the experiments, with a water tank of 0.5 m<sup>3</sup> volume. The results of these experiments are shortly reviewed and a new refined analysis based on [18] is presented. For the realization of the experiments, the data processing of the signals and more results cf. the original work [19,20].

With the obtained results, it could be demonstrated that the sound generation mechanism of intense pulsed beams is well described by the thermo-acoustic model. In almost all aspects investigated, the signal properties are consistent with the model. Relying on the model allows for the calculation of the characteristics of sound pulses generated in the interaction of high energy particles in water. As input to the model only water parameters and the energy deposition of the cascade resulting from the interaction are needed. Simulations of the acoustic pressure waves generated in ultra-high energy neutrino interactions will be presented in the following chapter.

### 3.1 The Thermo-Acoustic Model

The production of hydrodynamic radiation in form of ultrasonic pressure waves by fast particles passing through liquids was first predicted as early as 1957 leading to the development of the

---

<sup>1</sup>Abbr. for *Erlangen Centre for Astroparticle Physics*.

so-called *thermo-acoustic model* in 1970s [21–23]. This model was developed to describe the production mechanism of the bipolar shaped acoustic signals measured in an experiment with proton pulses in fluid media [24]. According to the model, the energy deposition of particles traversing liquids leads to a local heating of the medium which can be regarded as instantaneous with respect to the hydrodynamic time scale. Because of the temperature change the medium expands or contracts according to its volume expansion coefficient  $\alpha$ . The accelerated motion of the heated medium forms a pressure pulse – a micro-explosion – which propagates through the volume. The wave equation describing the pulse is [22]

$$\vec{\nabla}^2 p(\vec{r}, t) - \frac{1}{c_s^2} \cdot \frac{\partial^2 p(\vec{r}, t)}{\partial t^2} = -\frac{\alpha}{C_p} \cdot \frac{\partial^2 \epsilon(\vec{r}, t)}{\partial t^2} \quad (3.1)$$

and can be solved using the Kirchoff integral [25] to

$$p(\vec{r}, t) = \frac{1}{4\pi} \frac{\alpha}{C_p} \int_V \frac{dV'}{|\vec{r} - \vec{r}'|} \frac{\partial^2}{\partial t^2} \epsilon \left( \vec{r}', t - \frac{|\vec{r} - \vec{r}'|}{c_s} \right). \quad (3.2)$$

Here  $p(\vec{r}, t)$  denotes the hydrodynamic pressure at a given place and time,  $c_s$  the speed of sound in the medium,  $C_p$  its specific heat capacity and  $\epsilon(\vec{r}, t)$  the energy deposition density of the particles. Attenuation of the signal during the propagation can be introduced by substituting  $\vec{\nabla}^2 p$  by  $\vec{\nabla}^2 \left( p + \frac{1}{\omega_0} \cdot \frac{\partial p}{\partial t} \right)$ , with a characteristic attenuation frequency  $\omega_0$  in the GHz range. Resulting attenuation lengths for the acoustic signals exceed 100 m, so that attenuation is negligible for this analysis with distances below 1 m.

The resulting pressure field is determined by the spatial and temporal distribution of  $\epsilon$  and by  $c_s$ ,  $C_p$  and  $\alpha$ , the latter three exhibiting a substantial temperature dependence. A controlled variation of these parameters in laboratory experiments and a study of the resulting pressure signals allows therefore a precise test of the thermo-acoustic model. One decisive test is the disappearance of the signal at 4°C in water, the medium considered in this work, due to the vanishing  $\alpha$  at this temperature. This is a unique feature of the thermo-acoustic sound generation. In this regard, the observed pulses could not be unambiguously verified as thermo-acoustical in previously conducted experiments that investigated this effect in different liquids [24,26–31]. If studied in those articles, the variation of the pulse amplitude with the water temperature either did not distinctly show the predicted form or the measurement was afflicted with significant uncertainties. Particularly the disappearance of the signal was not found at 4°C but at higher temperatures.

The two experiments performed by our group enabled us to study the sound generation mechanism using different spatial and temporal distributions of the energy deposition as well as two different kinds of energy transfer into the medium, i.e. by excitation of the water molecules by both beams, and additionally by ionisation by the proton beam.

## 3.2 Comparison of Measured Signals to Simulation

In the analysis performed in [19,20] the measured signal shape (after processing) was found to be in fairly good agreement with the expectations. To better understand the signal shape

and include the frequency response of the sensors in the analysis, a simulation based on a numeric solution of Eq. 3.2 was developed. A scan of the input parameter ranges within their experimental uncertainties was carried out. The best fit of the simulation to exemplary recorded signals is shown in Fig. 3.1. The sensor position and beam parameters of the shown signals were chosen for the signal least distorted by external effects (cf. the original studies); the agreement between simulation and measurement is not as good for other positions.

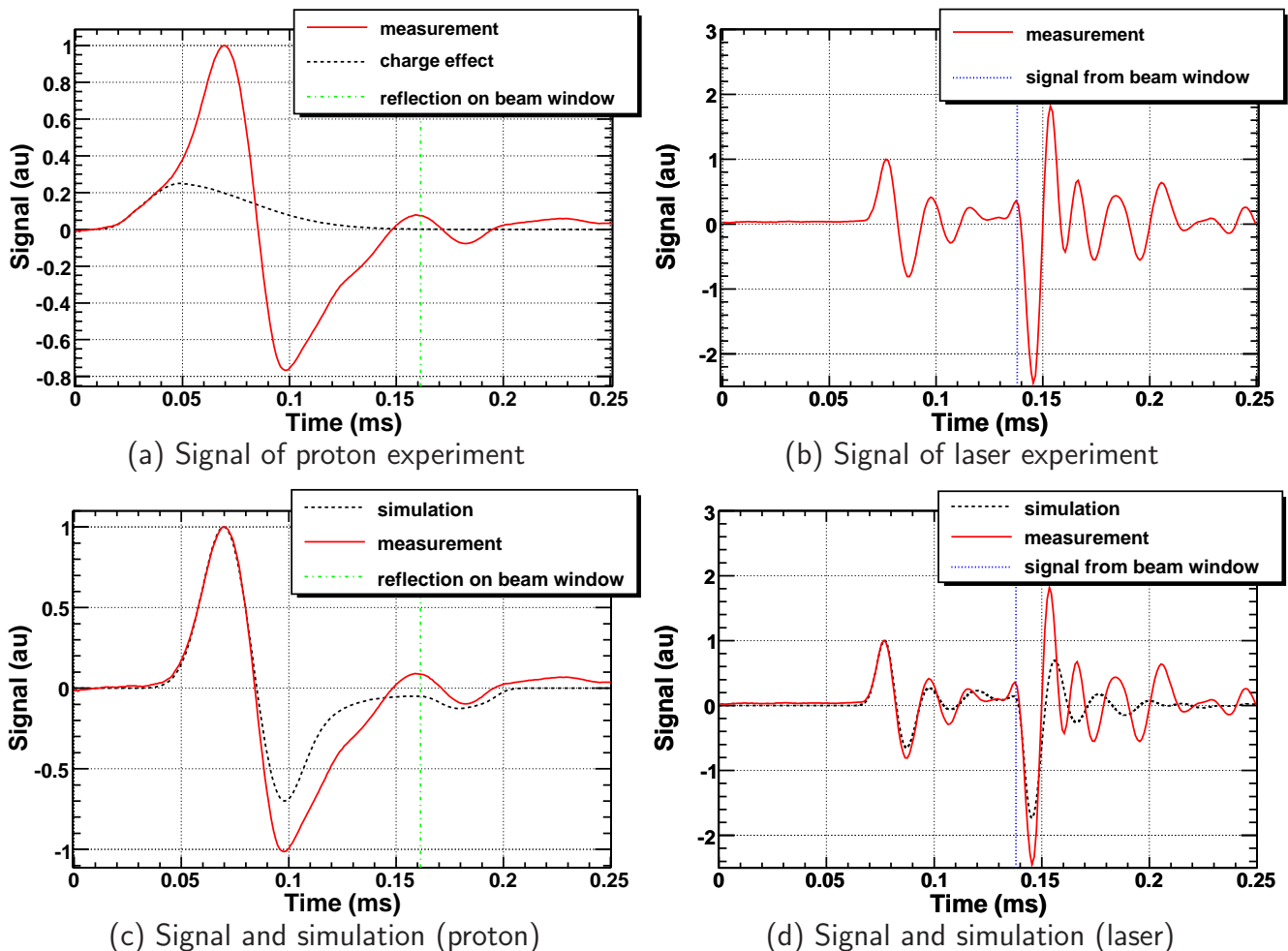


**Figure 3.1:** Exemplary signals measured in the proton experiment (a) and the laser experiment (b) and the same signals compared to simulation results (c and d). For better comparability the signals were filtered and normalised to unity at the first maximum. Both signals (solid lines) were recorded at a sensor position 10 cm along and 20 cm perpendicular to the beam axis. The black dashed line in (a) marks the charge effect described in the text, which has been subtracted in (c). The vertical dashed lines mark the arrival time of signals or reflections originating at the beam window.

The signals measured in both experiments are reproduced well by the simulation. While a typical signal for the proton beam (Fig. 3.1(a)) shows a bipolar signature, the one for the laser

deviates from this shape. The laser signal is distorted by the resonant sensor response to the higher frequency components in the acoustic wave, given by the short pulse time of  $\approx 9$  ns as compared to  $\approx 30$   $\mu$ s for the proton spill. Also, the shape of the energy deposition of the laser beam has a point of discontinuity at the beam entry into the water. Most of the energy is deposited in a small volume at that point. This leads to the two separate signals visible in Fig. 3.1(b), the first is produced at the same region along the beam axis as the sensor placement, the second at the beam entry. The signal of the proton beam is distorted primarily by two factors: a non-acoustic effect at the beginning of the signal (marked by a dashed black line in Fig. 3.1(a)) and reflections on the surfaces of the tank and the beam entry window. The former effect was found to be consistent with an electric charge effect in the sensors caused by the charged particles in the pulse, its shape is consistent with an integration of the temporal beam pulse profile with a subsequent exponential decay. The remaining differences between simulation and experiment are attributed to the uncertainties in the sensor response and in the beam characteristics.

### 3.3 Analysis Results

In the following, the major results obtained in a refined analysis of the experiments are presented, especially with a systematic treatment of errors. To minimise the impact of the signal distortions to the analysis, given by the effects described above, the same robust characteristics were used as in the original work. In particular, the peak-to-peak amplitude and the arrival time of the signal were studied; for the laser experiment the characteristics were calculated for the first signal only.

#### 3.3.1 Variation of the Sensor Position and Pulse Energy

Two fundamental characteristics of the thermo-acoustic sound generation are the speed of the wave propagation, i.e. the speed of sound, and the linearity of the signal amplitude with the total energy in the pulse or particle cascade. The results of the analysis for those two characteristics are shown in Fig. 3.2.

To verify the hydrodynamic origin of the measured signals the variation of the arrival times for different sensor positions perpendicular to the beam axis were investigated. Figure 3.2(a) shows the measured data and a linear fit for each beam type, yielding values of  $c_s = (1458 \pm 4) \frac{\text{m}}{\text{s}}$ , and  $c_s = (1514 \pm 4) \frac{\text{m}}{\text{s}}$ , in perfect agreement with the theoretical values [32] for the speed of sound at the water temperatures at the respective measurement. The observable offset between proton and laser beam is due a different delay time between trigger and arrival time of the different beam types in the water.

As shown in Fig. 3.2(b) the linear rising of the signal amplitude with pulse energy was observed in both experiments yielding a zero-crossing of the pulse energy at  $(-4.1 \pm 5.3)$  mPa for the proton beam and  $(42 \pm 87)$  mPa for the laser beam. The gradient is dependent on the energy deposition and the sensor positioning along the beam axis and cannot be compared between the two beam types.

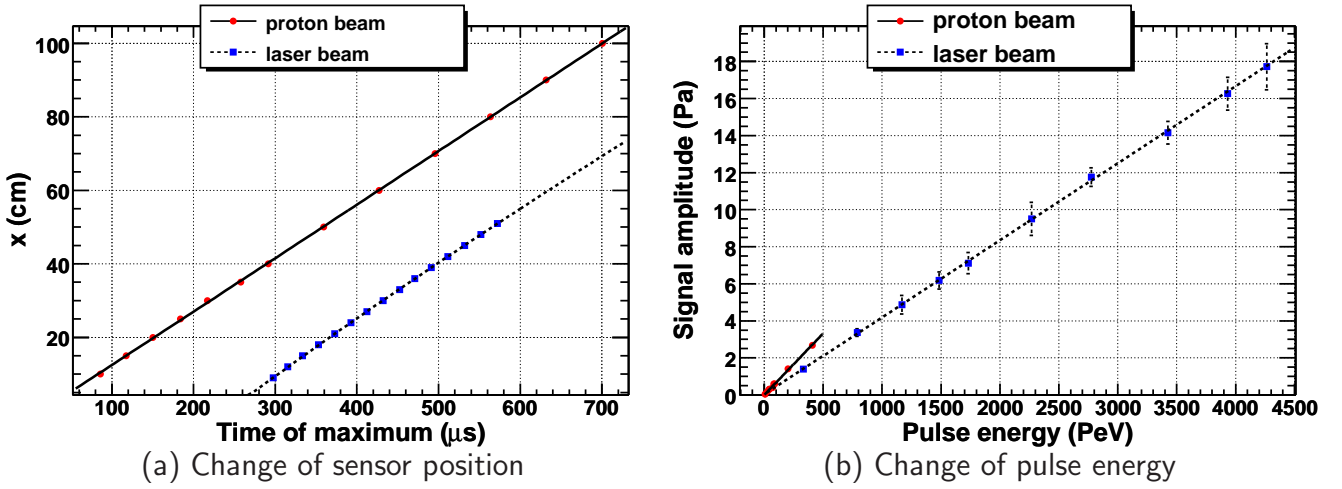


**Figure 3.2:** Left plot (a): Arrival time of the signal maximum for different sensor position perpendicular to the beam axis. The linear fit (solid and dashed line) yields sensible values for the speed of sound (see text).

Right plot (b): Peak-to-peak amplitude of the signal for different pulse energies. The errors in amplitude are enhanced by a factor of 10 for visibility. There is a ten percent systematic uncertainty in the absolute determination of the pulse energy. The lines are a linear fit to the data points yielding a zero-crossing of the amplitude compatible with no energy in a pulse.

### 3.3.2 Variation of the Temperature

The dependence of the signal amplitude on the water temperature is the main feature in the verification of the thermo-acoustic mechanism, because it is unique among models that have been proposed for the sound generation (cf. [22]). Figure 3.3 shows this dependence for the two experiments, with a positive (negative) sign denoting a leading positive (negative) peak of the signal.

The laser beam signal shown in Fig. 3.3(a) changes its polarity at around  $4.0^{\circ}\text{C}$ , as expected from the thermo-acoustic model. The model expectation for the signal amplitude, which is proportional to  $\alpha/C_p$ , is fitted to the experimental data. In the fit, an overall scaling factor and a shift in temperature (for the experimental uncertainty in the temperature measurement) were left free as fit parameters. The fit yielded a zero-crossing of the amplitude at  $(3.9 \pm 0.1)^{\circ}\text{C}$ , in good agreement with the expectation of the model of  $4.0^{\circ}\text{C}$ .

The first analysis of the proton data from [19] yielded a shape of the curve deviating from the model expectation, and a zero-crossing significantly different from  $4.0^{\circ}\text{C}$  at  $(4.5 \pm 0.1)^{\circ}\text{C}$ . Taking into account the results from the laser beam measurements, we subtracted the residual signal at  $4.0^{\circ}\text{C}$  from all signals. This was done assuming a small non-temperature dependent effect on top of the thermo-acoustic signal which is described by Eq. 3.1. The signal at  $4.0^{\circ}\text{C}$  has an amplitude of  $\approx 5\%$  of the signal at  $15.0^{\circ}\text{C}$  and is of tripolar shape. The resulting amplitudes after the subtraction, shown in Fig. 3.3(b), are well described by the model prediction.

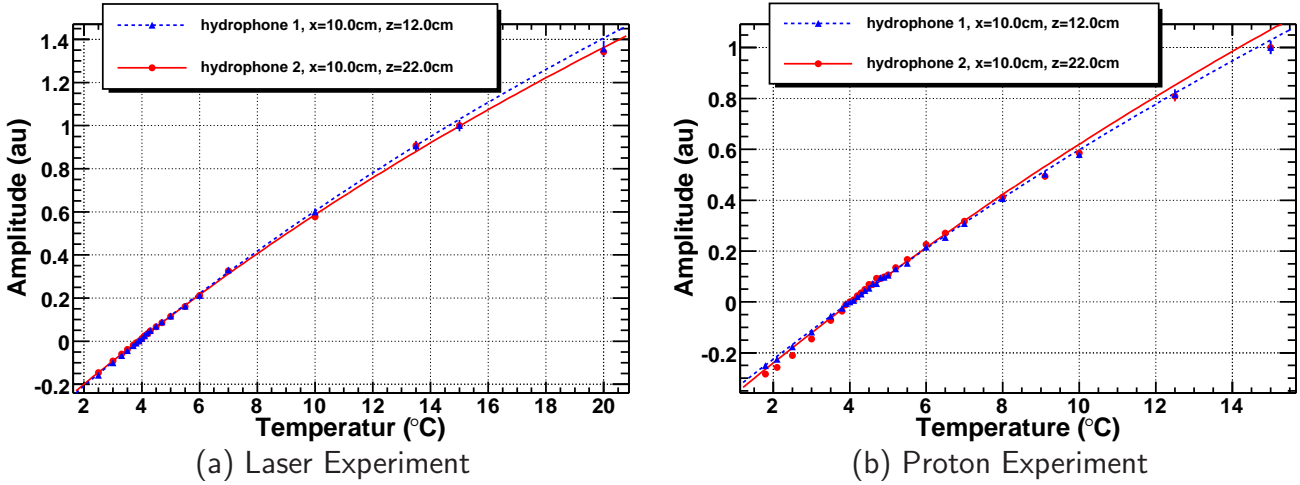


**Figure 3.3:** Measured signal amplitude of the bipolar acoustic signal produced by laser pulses (a) and proton spills (b) at different water temperatures fitted with the model expectation as described in the text. For better comparability all data points were scaled such that the amplitudes at  $15.0^{\circ}\text{C}$  are normalised to unity. For the proton experiment, a non-thermo-acoustic signal at  $4.0^{\circ}\text{C}$  was subtracted at every temperature before the determination of the signal amplitude.

The production mechanism of the underlying signal at  $4.0^{\circ}\text{C}$ , which was only observed at the proton experiment, could not be unambiguously determined with the performed measurements. Non-linear effects not included in the source term of Eq. 3.1, near-field effects or dipole radiation could contribute significantly near the disappearance of the volume expansion coefficient [33]. Also other non-thermo-acoustic signal production mechanism have been discussed in the literature which could give rise to an almost temperature independent signal, see e.g. [22]. The obvious difference to the laser experiment are the charges involved both from the protons themselves and the ionisation of the water which could lead to an interaction with the polar water molecules. In the case of a neutrino-induced particle cascade no net charge is introduced into the water, however, ionisation of the water molecules and a fast recombination of positrons leads to a negative charge excess in the cascade during its evolution in the water. Thus, if the observed underlying signal is of non-thermal origin, it could be generated in a particle cascade as well. From the observations of the proton experiment, the contribution of this signal to the total acoustic pulse is considered small for the water temperatures of the Mediterranean deep-sea ( $\approx 13^{\circ}\text{C}$ ) and thus of no direct impact to the acoustic detection method. However, also the minor contributions to the signal production mechanisms of particles in fluids should be studied further to allow for a precise prediction of the expected signal.

## Chapter 4

# Simulation of Acoustic Neutrino Detectors

In the previous chapter the thermo-acoustic sound generation was proven to be the main source of an acoustic signal generated in a high energy neutrino interaction. The evolution of the pressure pulse as described by the thermo-acoustic model depends strongly on the energy deposition of the particle interaction in the medium. In the case of an UHE neutrino interaction, a hadronic and – depending on the reaction type – also an electro-magnetic *cascade* or *shower* of secondary particles evolves which deposit their energy into the water mainly via ionisation. Due to lack of experimental data in the ultra-high energy regime, the energy deposition along the cascade axis must be simulated by Monte-Carlo simulations and the parameters of the interactions extrapolated from lower energies. Several studies have been performed based e.g. on GEANT and CORSIKA simulation software (cf. [15,34–36] and references therein). For this work, the latest simulation study [36] is used as a reference, where the CORSIKA simulation package for extensive air showers was adapted to describe the shower evolution in water or ice and compared to other studies [34,35]. The advantage of that package over e.g. GEANT4 is the applicability up to the energy range of interest, whereas the GEANT4 package, which is usually used to simulate accelerator experiments has to be extrapolated in energy over several orders of magnitude and additional effects – like the Landau-Pomeranchuk-Migdal (LPM) [37,38] effect – have to be included (cf. [35]).

### 4.1 Calculation of the Expected Signal

Basis for the calculation of the pressure pulse is the simulated energy deposition of the cascade, which is in good approximation rotationally symmetric around the cascade axis. The resulting acoustic signal can be calculated from a simplified form of Eq. 3.2, where an instantaneous deposition with respect to the acoustical time scale is assumed and the cylindrical symmetry of the cascade is used [36]:

$$p(\vec{r}, t) = \frac{E}{4\pi} \frac{\alpha}{C_p} \int_V \frac{dV'}{|\vec{r} - \vec{r}'|} \varepsilon \frac{\partial}{\partial t} \left[ \delta \left( t - \frac{|\vec{r} - \vec{r}'|}{c_s} \right) \right]. \quad (4.1)$$

The result of this equation is a *bipolar pressure pulse*  $p$  at a given point  $\vec{r}$  and time  $t$  of a cascade with total energy  $E$  and a relative energy density  $\varepsilon = (1/E)(1/2\pi r)\partial^2 E/\partial r'\partial z'$  (in cylindrical coordinates  $r'$  and  $z'$ ).

An acoustic pulse of bipolar shape, resulting from the simulation of a  $10^{20}$  eV cascade, is shown in Fig. 4.1(a) as a function of time and in Fig. 4.1(b) its spectrum in the frequency domain. The shown pulse was calculated in a plane perpendicular to the cascade axis at the  $z$  value of the maximum energy deposition density in the longitudinal profile.

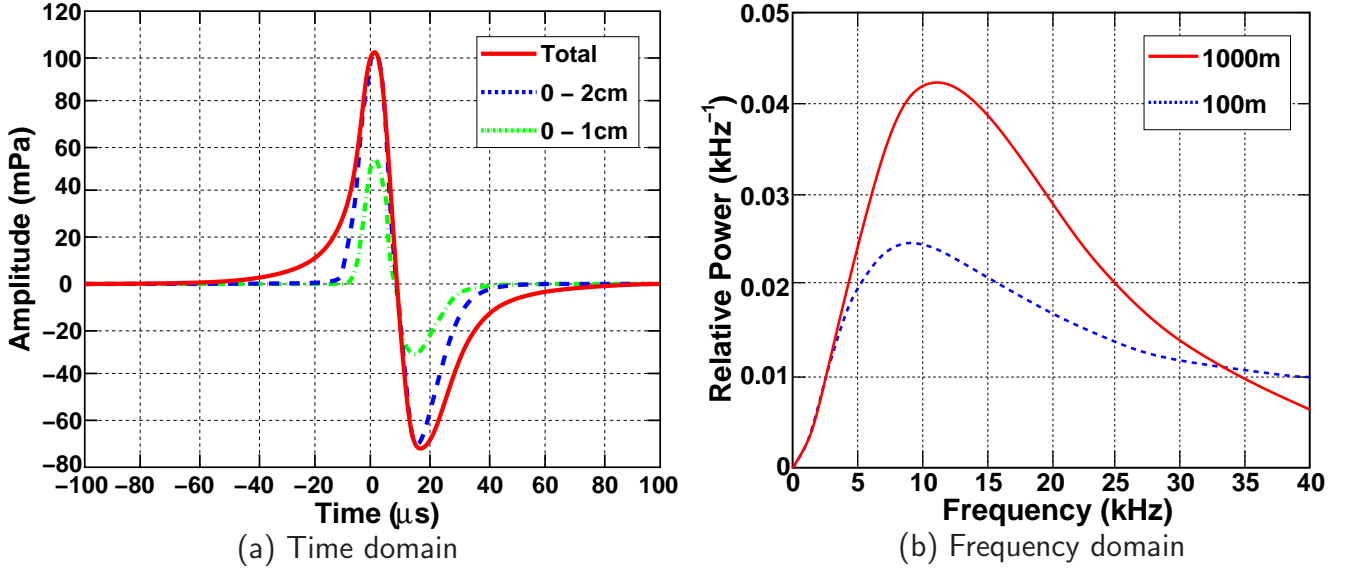


**Figure 4.1:** Simulated acoustic pulse for a  $10^{20}$  eV shower at 1 km distance from the shower centre. For the signal in the time domain (a) the contribution of the radial distribution up to 1 cm and 2 cm from the shower core and for the whole shower is plotted. In the frequency domain (b) the relative power spectrum is plotted for a distance of 100 and 1000 m from the shower. Both figures have been adapted from [36].

The main contribution to the signal amplitude is generated from within the inner part of the cascade ( $r' < 2$  cm), the shower core. Therefore the exact simulation of the lateral distribution of the energy deposition is crucial for the accurate calculation of the signal. The uncertainties in this distribution, governed by the not well measured properties of inelastic scattering in extremely forward direction, are mainly responsible for the different signal shapes and amplitudes in other studies on acoustic particle detection (cf. e.g. [39]).

The calculated signal (cf. Fig. 4.1(a)) has a peak-to-peak amplitude of  $\approx 170$  mPa/ $10^{20}$  eV<sup>1</sup> and a temporal length from the maximum to the minimum of  $\approx 15$  μs. The frequency spectrum (cf. Fig. 4.1(b)) peaks at  $\approx 9$  kHz for small distances (100 m) with a steep rise from lower frequencies and a long tail towards high frequencies. At higher distances (1000 m) the signal propagation through the medium alters the spectrum. The peak of the spectrum shifts to  $\approx 11$  kHz and an attenuation of the higher frequency components becomes observable.

<sup>1</sup>The signal amplitude evolves linearly with energy.



## 4.2 Signal Propagation

After generation of the acoustic signal, the pressure wave propagates through the medium – in the case of this work sea-water. Here major features with respect to acoustic particle detection arise: the propagation in a *disc-like shape* and the long attenuation length, both depicted in Fig. 4.2.

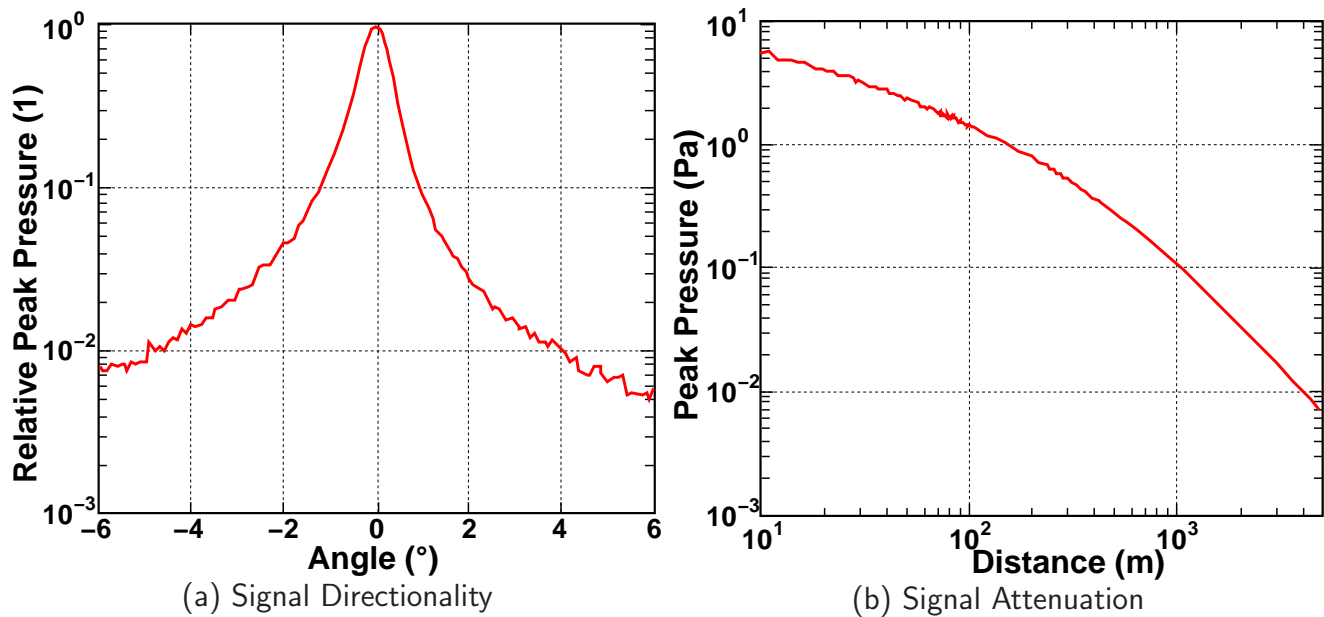


**Figure 4.2:** Simulated signal directionality (a) for a  $10^{20}$  eV shower at 1 km distance from the origin, with the peak pressure as a measure, normalised to the peak pressure at  $0^\circ$  (perpendicular to the shower axis). Evolution of the peak pressure with distance from a shower (b) of same energy. Both figures are adapted from [36] and described in the text.

The first feature is a consequence of the cylindrical energy deposition: the sound wave adds up coherently perpendicular to the shower axis. Therefore, the emission is highly peaked in this direction (cf. Fig. 4.2(a)) and the sound propagates through the water in a ring or disc shape (cylindrical wave). This directed emission is one property which can be used – if reconstructed in a detector – to distinguish neutrino induced events from transient background signals of bipolar shape which are assumed to emit spherical waves. The coherent emission from the cascade also keeps the signal form stable over distances up to several kilometres, whereas the coherence length of background signals is assumed to be much smaller – a feature which has to be thoroughly studied in a prototype setup for an acoustic detector like the AMADEUS project. Also due to the cylindrical wave emission, the signal amplitude, being the value recorded by acoustic sensors, drops only as  $1/\sqrt{r}$  and  $1/r$  for near and far field, respectively (where  $r$  is the distance from the source) (cf. Fig. 4.2(b)). The crossover between near and far field is in the order of 100 m. The attenuation length of acoustic signals in water, which is taken into account in the plot, in the respective frequency ranges of interest is more than one order of

magnitude higher than that of light, ranging from 70 km at 1 kHz to 100 m at 100 kHz [40,41]. At the maximum relative signal power around 10 kHz the attenuation length exceeds 3 km. Additionally the signal is also refracted due to a changing sound velocity with depth, an effect only becoming important for distances exceeding 1 km (cf. [34]).

## 4.3 Sensitivity Studies of Acoustic Detectors

The sensitivity of an acoustic detector for UHE cosmic neutrinos depends on a variety of variables. One major question is the threshold for the unambiguous identification of the neutrino signal in the acoustic background, another is the detector layout.

Each of the variables can be estimated and their impact on the detector sensitivity can be simulated. But mainly due to the difficult signal identification and the not well-known background situation, such simulations have to be tested in experimental studies with sensor arrays in the sea.

### 4.3.1 Background for Acoustic Neutrino Detection

The background for the acoustic detection of UHE neutrinos can be divided in two classes: *ambient noise* and *transient signals* or *transients*.

Ambient noise is the superposition of broadband signals produced by a variety of sources, which are not individually identifiable. It has been studied extensively (see e.g. [42,43] for reviews on noise in the sea) and can be divided roughly in three frequency bands [15]:

- **below 200 Hz:**

Without relevance to acoustic detection, the ambient noise below 200 Hz is dominated by sea current and turbulences in the water. Additionally anthropogenic sources, such as ship noise, contribute to this highly variable band. Transients in that frequency range are expected e.g. from seismic activity, ships and marine life. The noise power spectrum is assumed to decrease steeply with frequency by  $-8$  to  $-10$  dB per octave.

- **200 Hz to 50 kHz:**

This band is the most important one for neutrino detection, because here their acoustic signals are expected. The noise is falling with frequency by  $-5$  to  $-6$  dB per octave and is primarily dependent on the weather conditions on the sea-surface and the resulting agitation of the surface. The wind activity dominates the noise level over the whole band, creating noise via turbulences, motion of the sea surface, surface wave interactions, spray and cavitation (air bubbles near the surface). Rain is predicted to lead to a peak around 15 kHz [44]. Sources for transient signals in that region are again marine life and anthropogenic/technical.

- **above 50 kHz:**

Here the thermal motion of the water molecules colliding with the sensor starts to dominate the noise spectrum. The spectral power of the noise rises with frequency by roughly

6 dB per octave. The actual minimum in the spectrum is dependent on the weather conditions.

As the ambient noise in the deep-sea in the frequency range of interest with respect to acoustic neutrino detection is assumed to be dominated by the agitation of the sea surface (see below), this parameter can be used to describe the noise situation. The relation between the wind speed at a given location and the agitation of the sea-surface (*sea-state*) at the same location is defined by the US Navy and Beaufort Sea-State Codes [45] as described in Tab. 4.1.

Sea-State (SS)	Beaufort Number	Wind Speed (knots)	Wind description
0	0	< 1	Calm
0	1	1 – 3	Light air
1	2	4 – 6	Light breeze
2	3	7 – 10	Gentle breeze
3	4	11 – 16	Moderate breeze
4	5	17 – 21	Fresh breeze
5	6	22 – 27	Strong breeze
6	7	28 – 33	Near gale
7	8	34 – 40	Gale
8	9	41 – 47	Strong gale
9	10	48 – 55	Storm
9	11	56 – 63	Violent storm
9	12	≥ 64	Hurricane

**Table 4.1:** Definition of the sea-state by the wind speed at the surface (in knots (kt), 1 kt  $\hat{=}$  0.5144 m/s).

An, on average, representative parametrisation of the ambient noise in the deep-sea is shown in Fig. 4.3. The parametrisation was derived in [42] for prediction purposes; in the frequency range from 400 Hz to the set-in of the thermal noise, i.e. where the curves exhibit a  $f^{-5/3}$  behaviour, the spectra are known as *Knudsen spectra* [46]. It does not take into account any local variations or particular sources of noise and can thus be only regarded as a rough approximation of the noise conditions to be expected at any specific site.

In this ambient noise parametrisation, the shape of the wind induced part of the noise spectrum is peaked at  $\approx 300$  Hz, independent of the wind speed. Only the level of the spectrum rises with higher agitation of the surface. The wind level also influences the point of crossing over to the rise in the spectrum due to the thermal noise at high frequencies. For the lowest possible agitation of the sea surface at sea-state 0 (SS0), the minimum of the ambient noise spectrum lies as low as 35 kHz, for SS1 already at 70 kHz and above SS1 beyond 100 kHz.

In Fig. 4.3 the spectrum of an expected neutrino signal is also plotted in arbitrary units, which rises up to roughly 10 kHz to fall off again beyond that value. As seen in the previous section, the shape of the spectrum is not much dependent on the signal energy or sensor position with respect to the shower axis (as long as it is inside the acoustic disc). The power level of the

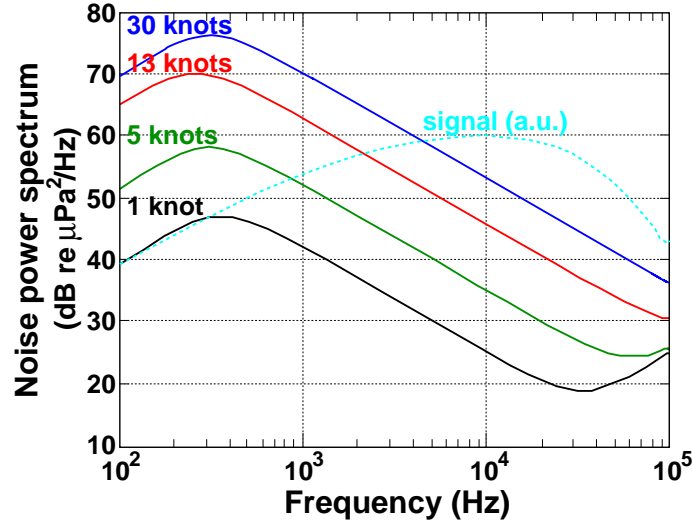


**Figure 4.3:** Ambient noise spectra for different wind speeds (1 knot  $\hat{=}$  SS0, 5 knots  $\hat{=}$  SS1, 13 knots  $\hat{=}$  SS3, 30 knots  $\hat{=}$  SS6) and the expected spectrum of a neutrino signal. The absolute signal amplitude is dependent the neutrino energy and distance between shower and sensor. Adapted from [47] and valid for at depths of  $\approx$  1500 m.

signal, however, depends on the cascade energy, the distance from the source and time window for the power spectrum calculation.

One interesting feature is that the maximum spectral density of the neutrino signal lies almost in the spectral minimum of the noise for low sea-states, and for all conditions in the falling edge of the noise spectra. It can be deduced that the frequency band of interest for acoustic particle detection lies somewhere between 1 kHz and 100 kHz. The optimal range for observation depends on the level of the ambient noise and its individual features at the detector site.

The signal to noise ratio (*SNR*) is used to compare the power spectral density of a persistent signal, like the ambient noise, with constant signal power but unlimited signal energy (*power signal*) to a transient signal with evanescent power but finite signal energy (*energy signal*). The *SNR* is defined here as peak-to-peak amplitude of the energy signal divided by the standard deviation ( $\sigma$ ) of the power signal. For the later value, the power spectral density (*PSD*)<sup>2</sup> has to be integrated within a predefined frequency band – here, 1 to 50 kHz was chosen. For the plotted sea-states SS0, SS1, SS3 and SS6, the RMS of the ambient noise, defined in this fashion, is 6.2, 17, 52 and 126 mPa, respectively. At a 1 km distance from a cascade evolving in a neutrino interaction, this would lead to an *SNR* of unity at energies of 3.5, 10, 33 and 63 EeV inside the sonic disc. From this coarse estimate, the typical detection threshold of an acoustic detector becomes already palpable to be in the ultra-high energy regime.

It is pointed out that a comparison of a power signal with an energy signal in the frequency domain cannot be unambiguously defined. The power spectral density for a transient signal

<sup>2</sup>The definition of the power spectral density used here follows the one in [48], where it was normalised such that the integral of the PSD over the whole frequency range gives the  $\sigma$  of the signal.

is a function of the analysed time window, whereas for a persistent signal it is constant or varying only with changing conditions. As the ambient noise is the main point of interest and always present at the experimental studies conducted in this work, it was chosen to present also transients in the frequency domain by their PSD, but always with an indication of the used time window.

The efficiency for the identification of the neutrino signal in the ambient noise is not only dependent on the noise level but also on the correlation length of the noise and random transients in it, which could mimic neutrino signals in a detector if their correlation length is high enough. The thermal noise is expected to have very short correlation lengths, thus random correlations in it can be already suppressed by searching for correlations on short sensor distances. However, the surface generated noise could exhibit much longer correlation lengths, rendering a distinction between signal and background transients challenging. The correlation lengths in the background have to be thoroughly studied when determining the efficiency of the signal identification.

### 4.3.2 Detector Sensitivity

To simulate the sensitivity and performance of acoustic detectors, several studies have been performed, out of which two [15,49] are considered here. Both simulation studies yield similar results and are using the same, somewhat conservative assumptions to assess the sensitivity of an acoustic detector. Only those results are presented which are considered essential for the understanding of the layout of the AMADEUS setup (which is detailed in Chap. 6).

One basic assumption concerns the threshold  $p_{th}$  at which a sensor is assumed to trigger, i.e. where the acoustic signal of a neutrino is identified in the acoustic background. This was calculated [49] to be  $p_{th} = 35$  mPa to allow for one falsely triggered event in 10 years with a five-fold coincidence in the sensors. In [15] a possibility to lower this threshold was presented by introducing *acoustic clusters*, i.e. local clusters of acoustic sensors, where local coincidences can be used to suppress spurious correlations. In the case of a completely uncorrelated background, the threshold would then fall by  $1/\sqrt{N}$ , where  $N$  is the number of sensors in the cluster. The concept of sensor clusters has also advantages in the processing of the signal, as will be detailed later on in this work.

As a reference detector for the determination of the sensitivity,  $1 \text{ km}^3$  of instrumented volume with randomly distributed sensor clusters were chosen, with neutrino interactions generated in a can of  $5700 \text{ km}^3$  around the detector, determined from refraction considerations. For energies above several hundreds of TeV the Earth is opaque to neutrinos, i.e. only UHE neutrinos from the upper hemisphere are considered. The neutrino directions and interaction points are randomly distributed within the can and the events are then detected with the array of sensors.

The dependence of the effective volume  $V_{eff}$  ( $V_{eff} = \frac{N_{det}}{N_{gen}} V_{gen}$ , with  $N_{det}$  detected neutrinos out of  $N_{gen}$  generated ones which interact in a volume of  $V_{gen}$ ) on the sensor threshold is given in Fig. 4.4(a), whereas its dependence on the local cluster density is shown in Fig. 4.4(b). No quality cuts have been applied on the data for these plots.

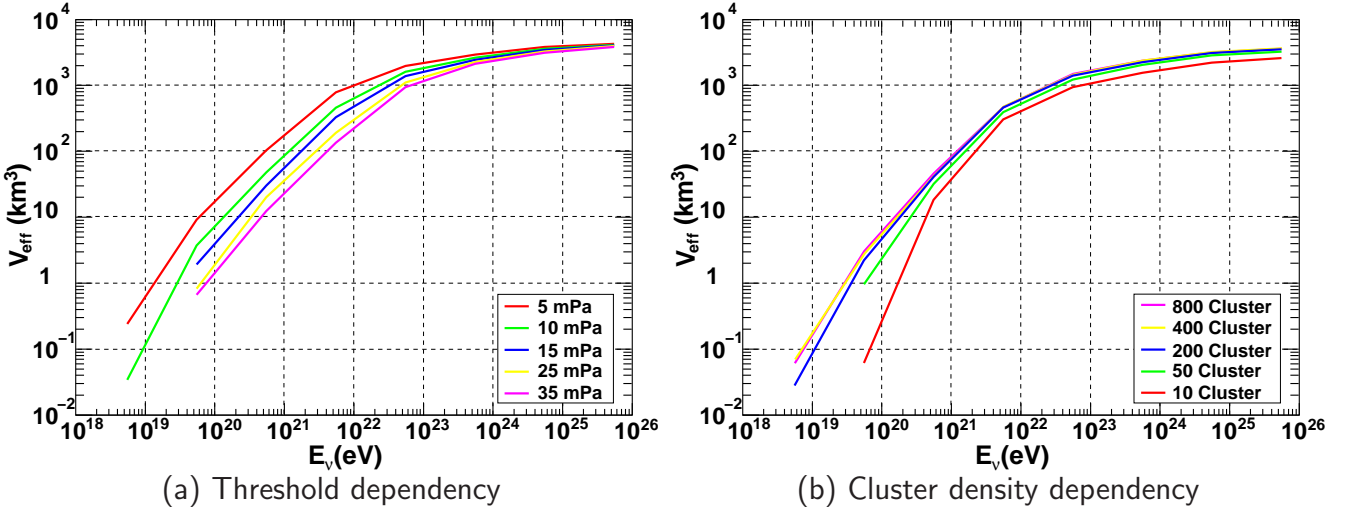


**Figure 4.4:** Simulated effective volumes for different sensor thresholds (a) and acoustic cluster densities (b). The instrumented volume for both plots is  $1 \text{ km}^3$ , the detector in (a) consists of 200 clusters, the threshold in (b) is set to 5 mPa. Both figures adapted from [15].

The following considerations are based on a reference acoustic detector of  $1 \text{ km}^3$  instrumented volume with 200 randomly distributed sensor clusters, which are triggered at a signal threshold of 5 mPa (consistent with the top red curve in Fig. 4.4(a)). The effective volume of such a detector exceeds its instrumented one at 20 EeV and rises steeply with energy. At a one order of magnitude higher energy, already an effective volume of  $20 \text{ km}^3$  is reached. The effective volume approaches the can volume of  $5700 \text{ km}^3$  asymptotically with rising energy. Thus, with this detector mainly events can be reconstructed which occur outside the detector. For those events, the sound waves propagate into the detector through its surfaces (*surface detector*). The potential of an acoustic neutrino detector can be assessed when considering that these effective volumes are already possible with as little as 200 sensor clusters per cubic kilometre, as compared to the new generation Cherenkov telescopes IceCube [50] and KM3NeT [51] with a sensor density of roughly 5000 optical sensors per cubic kilometre and are optimised for energy thresholds of 10 – 100 GeV. The effective volume for cascades of e.g. the  $1 \text{ km}^3$  sized IceCube neutrino telescope is  $\approx 3 \text{ km}^3$  at 1 EeV and rises from there only by  $\approx 0.15 \text{ km}^3$  per decade in energy [52].

The instrumented volume of the reference detector is not sufficient for detecting neutrinos from the GZK effect or from AGNs for which, as presented in Sec. 2.2, much larger detectors with instrumented volumes exceeding several tens or even hundreds of cubic-kilometres have to be considered – a fact that renders optical detection<sup>3</sup> of UHE neutrinos at least challenging, if not infeasible<sup>3</sup>. In these huge – up to now hypothetical – detectors the parameters, such as the can volume, change dramatically with respect to the presented small reference detector, as by

<sup>3</sup>An interesting option is a hybrid detector using optical, acoustical and radio methods in one array [53].

the huge detector more events occurring inside the instrumented volume are detected (*volume detector*). Especially the reconstruction precision of the neutrino direction and energy for those events are much improved compared to interactions outside the instrumented volume, as more information can be gathered in the sensors.

As becomes obvious from Fig. 4.4(b) not much efficiency is gained by increasing the sensor density above 200 clusters per  $1 \text{ km}^3$ , which means an average inter-cluster spacing of roughly 200 m. This is the length scale, where a feasibility study should position sensors, or better, clusters of sensors. The idea of local clusters of sensors is not only interesting for simple trigger conditions like a threshold. All filter strategies can profit from small clusters, as the complexity of data filtering algorithms scale more than linearly with the number of data samples and can be calculated much faster and more efficient at smaller time windows and thus length scales. Consequently, a preselection or even prereconstruction can be done in short time and the results from the different clusters combined to a global event reconstruction.

The efficiency of such an acoustic detector is, however, highly dependent on the trigger conditions, as shown in Fig. 4.4(a). For the simple threshold trigger used in the simulation studies, the effective volume at  $10^{20} \text{ eV}$  is roughly inversely proportional to the threshold. The study of efficient filter algorithms thus provides a means to increase the detection efficiency profoundly. Such studies were and are performed with much more elaborated strategies than a simple threshold trigger, using e.g. cross- and autocorrelation, singular value decomposition and independent component analysis [54,55]. For overviews on data filtering and processing in acoustic detection see also [16,17]. Of course, a high efficiency of such filter algorithms is necessarily coupled to an extremely good understanding of the background conditions.

A point not studied in the simulations, as it is presently unknown, is the dependency of the detector performance on the rate of neutrino-like background transients. If those exist and exhibit a long correlation length, it could render an acoustic detector unfeasible as such signals could – if at all – only be distinguished from neutrinos by their different sound wave propagation. This rate has to be determined with experimental setups as e.g. the AMADEUS project described in the next part of this work.





## **Part II**

# **ANTARES and AMADEUS**



# Chapter 5

## Acoustic Particle Detection in ANTARES

The potential of the acoustic method to detect UHE cosmogenic neutrinos was motivated in the previous chapter. As pointed out, there is a variety of open questions that need to be investigated in experimental studies. In this chapter the ANTARES neutrino telescope, its techniques and the physics programme are briefly introduced. Furthermore, the integration of an acoustic extension to the detector is motivated: The AMADEUS project to study the feasibility of a future large scale neutrino detector for ultra-high energy neutrinos. The AMADEUS experiment itself is described in the next chapter.

### 5.1 The ANTARES Experiment

The ANTARES collaboration<sup>1</sup> aims for the detection of high-energy cosmic neutrinos. Towards this goal the ANTARES neutrino telescope [56] is currently build in the Mediterranean Sea, about 40 km south of the city of Toulon (France). The site of the detector is at a water depth of 2500 m and a location of 42°50'N, 6°10'E (cf. Fig. 5.1).

At the time of writing, over 80% of the detector are installed and operational. The full detector with 885 photo-sensors in an instrumented volume of  $\approx 200 \times 200 \times 400 \text{ m}^3$  is expected to be completed and operational by mid 2008.

#### 5.1.1 Physics Program

The main goal of the ANTARES experiment is the detection and study of high-energy cosmic neutrinos in the energy range from a few 100 GeV to roughly 100 TeV, where the expected fluxes of cosmic neutrinos become too low to amount for a measurable rate of events in the detector. One of the major questions addressed is the origin of the cosmic rays and their acceleration processes. Under study are both astrophysical point sources - such as Supernova Remnants,

---

<sup>1</sup>A European collaboration incorporating scientists and technicians from 24 institutes in seven countries.

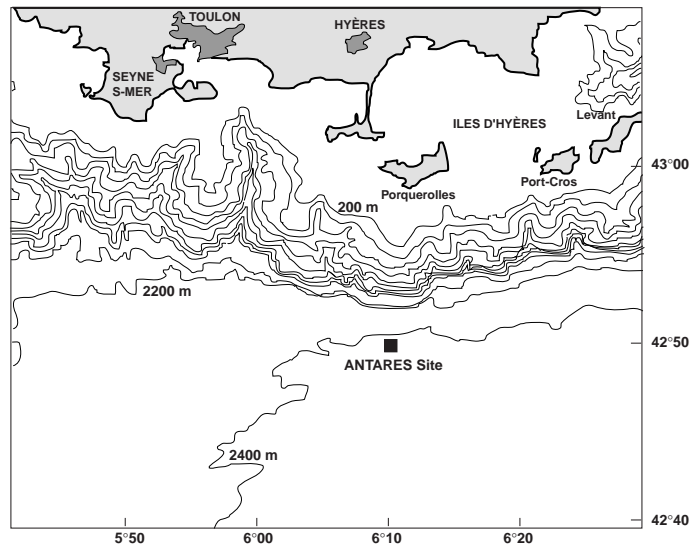


**Figure 5.1:** Map showing the location of the ANTARES site in the Mediterranean Sea, including the French southern coast area around the city of Toulon in gray and the water depths. Figure from [56].

Active Galactic Nuclei, the Galactic Centre or Gamma Ray Bursts - and diffuse fluxes from a superposition of many sources or the interaction of cosmic rays during their propagation. Yet a neutrino telescope also provides the possibility to search for phenomena outside the standard model of particle physics, e.g. topological defects, magnetic monopoles and dark matter in form of neutralino annihilation. The physics programme of ANTARES is comparable to that of an acoustic detector, but at more than three orders of magnitude lower energies. However, rare events may be seen coincidentally with both detection types in a hybrid mode.

In addition to the astroparticle physics programme, the ANTARES detector serves as a platform for the investigation of the deep sea environment by oceanologists, geologists and physicists (among others).

### 5.1.2 Detector Design

The detector is based on the optical technique, utilising Cherenkov light [57] emitted by charged secondaries which are produced in neutrino interactions. The sensor array is optimised to reconstruct the long tracks of muons generated in a  $\nu_{\mu}$  charged current interaction, but the detection of the other neutrino flavours is also possible using the Cherenkov light emitted by charged particles in a neutrino induced hadronic or electromagnetic cascade.

To suppress the several orders of magnitudes ( $\approx 6$ ) higher background of atmospheric muons coming from above (down-going), all high-energy neutrino detectors<sup>2</sup> currently operational or planned detect mainly neutrinos coming from below (up-going) and thus utilise the Earth as a

<sup>2</sup>AMANDA/IceCube [50,58], ANTARES [59], BAIKAL [60], KM3NeT [51], NEMO [61] and Nestor [62].

shield for cosmic rays and their interaction products.

The design of the detector is adapted to this prerequisite and its location in the deep sea. To withstand the hostile environment, all mechanical detector components are made of either Titanium, glass or special plastics, and all sensitive electronics is shielded in containers.

### The Detection Lines

The basic detector design, shown in Fig. 5.2, consists of 12 vertical structures (*detection lines*) with a height of 480 m and an inter-line spacing of 60 to 75 m.

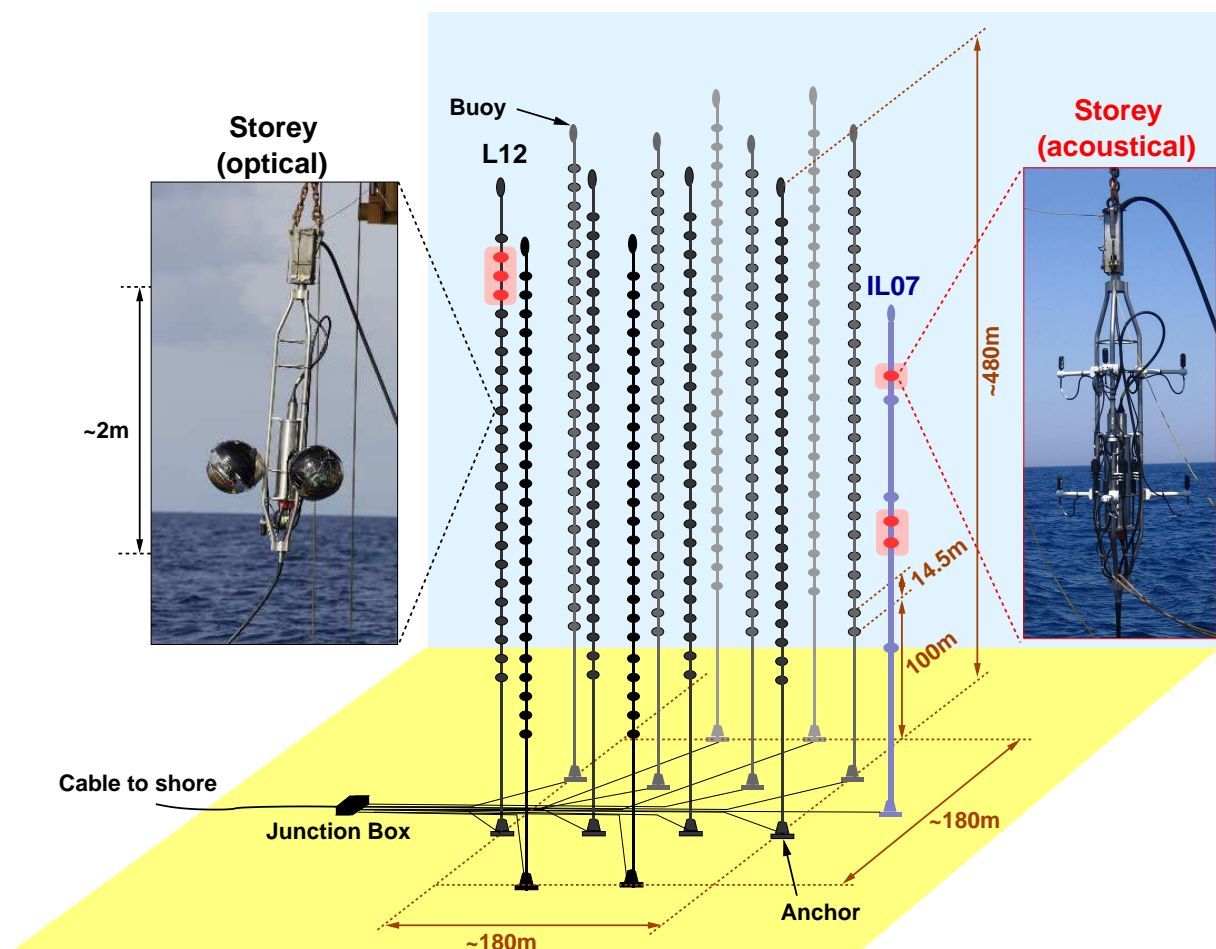


**Figure 5.2:** Schematic of the ANTARES detector (not to scale) with its acoustic extension (cf. Chap. 6) marked red. All 12 detection lines (in black) and the instrumentation line (in blue) are shown with positions of the storeys marked as circles. As additional basic structures the BSSes (anchors), buoys, junction box and interconnection cables are displayed - for details see text. Inserts show pictures of an optical and an acoustical storey at their installation at the site. Adapted from [63].

Those lines comprise an *electro-mechanical cable (EMC)*, which is put under tension by a dead weight at the *bottom string socket (BSS)*, an anchor module with electronics and instruments,

and a buoy at the top of the line. The EMC does not only act as a mechanical structure, but also provides the power to the electronics and the optical data transfer between the elements of the detector. With a vertical separation of 14.5 m, 25 *storeys* – the active parts of the detector holding the photo-sensors – are fixed to a line. Due to their flexible setup, the lines are floating in the sea current with typical speed of below 10 cm/s.

All lines are connected to the *junction box* and the data transmission and power supply to the shore is established via a deep sea communication cable. At the shore the data arriving from the detector is processed in a PC farm, where it is filtered on-line and selected events with neutrino or muon signature are stored for later off-line analysis. In addition to the detection lines which are labelled L1 – L12, an *instrumentation line (IL07)* for environmental monitoring and deep sea research is currently part of the detector.

With the three-dimensional array of photo-sensors, the arrival times of the Cherenkov photons are recorded and the track of the secondary – typically a muon – is reconstructed from the known angular distribution of the light emission. Additionally the energy of the secondary or secondaries in a cascade can be estimated and thus both direction and energy of the neutrino can be deduced. The Cherenkov light is detected in the wavelength band from  $\approx 300$  to  $\approx 600$  nm with 10" *photo-multiplier tubes (PMTs)* [64] with  $500\text{ cm}^2$  of photo-cathode area. Each PMT is housed in a 40 cm diameter pressure tight glass sphere, forming together the *optical module (OM)* [65]. Three optical modules are grouped on the metal frame of each storey – see the left insert in Fig. 5.2. The OMs are mounted looking downwards at a  $45^\circ$  angle from the horizontal plane, with an angular separation of  $120^\circ$  around the vertical axis. The sensors are sensitive up to angles of  $\pm 60^\circ$  around their optical axis and thus overlap in the downward hemisphere suited for optical neutrino detection.

The sensors are read out by electronics inside a Titanium container (*local control module (LCM)*) at the centre of the storey. The sensor data is digitised there and is converted to a data stream transmitted optically through the line and the junction box to the shore station. A detailed description of the data-acquisition (*DAQ*) hardware in the ANTARES detector is given in the next but one section.

### Instrumentation Line and Detector Calibration

For an efficient operation of the ANTARES detector, its deep-sea environment has to be studied and monitored, and a variety of calibration parameters has to be measured.

The first objective has been met by up to now three instrumentation lines which have been devised and have been consecutively used in conjunction with the detection lines. After the so-called *Mini Instrumentation Line (MIL)*, deployed in 2003) and the *Mini Instrumentation Line with Optical Modules (MILOM)*, 2005) [66], the *Instrumentation Line 2007 (IL07)* [67] is installed at the ANTARES site at the time of writing.

With this line environmental parameters which are needed for the understanding of the detector or of interest with respect to deep-sea environmental research are recorded using the ANTARES slow control system. This system handles all data which are not directly needed for the data-taking in the detector, i.e. the read-out of the PMTs, and which are therefore not read out at a sub-nanosecond precision. Additionally this system transmits the settings from the on-

shore detector control to all off-shore devices. Examples for the parameters measured with the instrumentation line are the sea current velocity and direction, which is correlated to the position and orientation of the lines in the water.

For the calibration of the detector, additional devices are located throughout the experiment. As the lines are floating freely around the fixed location of the BSS, the position of the sensors has to be measured at time intervals of a few minutes. This is done by the positioning system, which is used to determine the position of the individual photo-multipliers to a precision of roughly 10 cm – consistent with the 0.5 ns time resolution of the optical sensors. The acoustical part of the positioning system [68] consists of several acoustic *transducers* (devices able to transmit and receive acoustical signals) on the BSSes of each line and in pyramidal structures located around the detector and *hydrophones* (devices able to receive acoustical signals under water) on roughly every fifth storey of each line. The transducers, also called *pingers*, whose positions are measured at their installation at the site via GPS positioning, emit acoustic signals with frequencies ranging from 50 kHz to 60 kHz. The position of the acoustic sensors can be triangulated using the time difference between the emission of the pinger signals and their reception at the hydrophones. Together with the alignment of the storey – measured by an electronic compass in the LCM – the position of each storey and each OM on it can be deduced.

For timing and sensitivity calibration of the photo-multipliers and their read-out, several light sources are integrated: lasers at BSSes, beacons with blue LEDs in roughly every fifth storey of each line [69] and LEDs in every OM.

### The ANTARES DAQ System

The ANTARES data-acquisition (*DAQ*) system [70] consists of a distributed network of processing units with a significant part located off-shore. A PC farm located at the shore station controls the detector and filters the data preprocessed at the storeys. As typical rates per photo-multiplier are 100 kHz (from bioluminescence activity of sea fauna and  $^{40}\text{K}$  decays in the sea water [71]) and a typical event rate from atmospheric muons<sup>3</sup> is in the range of 10 Hz, a data-reduction factor exceeding  $10^4$  has to be achieved in on-line filtering.

The DAQ system is implemented as a finite state machine, in which every processing unit is running independently in a predefined state. The state itself and transitions between states – e.g. at the start of data-taking – are controlled by the ANTARES *RunControl* software. The software sends commands to the units and waits until they have reached the required state before proceeding. With this system it is guaranteed that each active unit is at the same state at all times. Data transmission between the parts of the system is implemented by the usage of optical or electrical Ethernet connections using the TCP/IP protocol.

The essential part of the off-shore DAQ system is the LCM with its electronics; a schematic and a photograph of an LCM is shown in Fig. 5.3. It is implemented by custom-built *boards* with dedicated tasks which are mounted on a common *backplane*. A power supply (*local power box*,

---

<sup>3</sup>Those events surpass the neutrino rate by  $\approx 6$  orders of magnitude and are all stored to be analysed off-line for detector calibration and reconstruction tests.

*LPB*) is deriving the required DC voltages for the boards from the high voltage provided through the EMC. The main DAQ component is the *DAQ board*, on which the Ethernet communication is established and the main processing unit (a Motorola powerPC chip, dubbed processor in Fig. 5.3(a)) running a VxWorks operating system is housed.

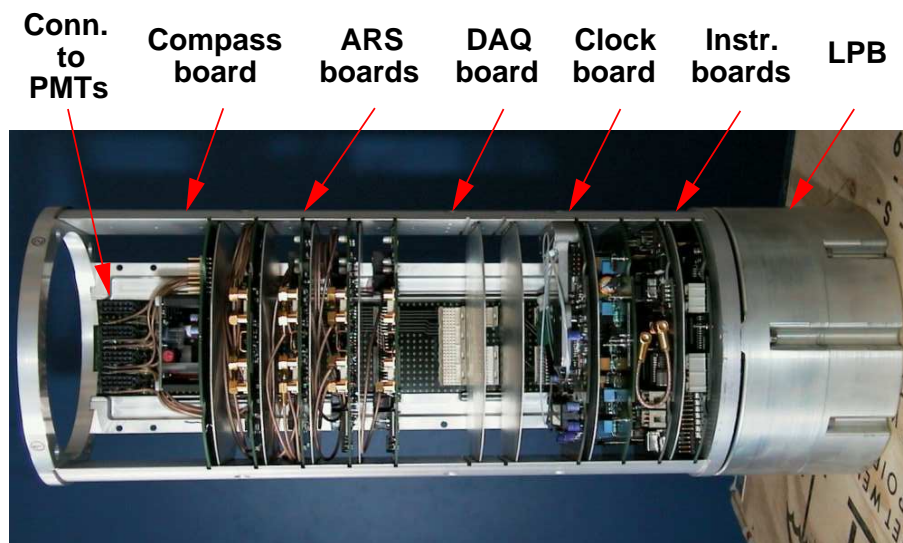
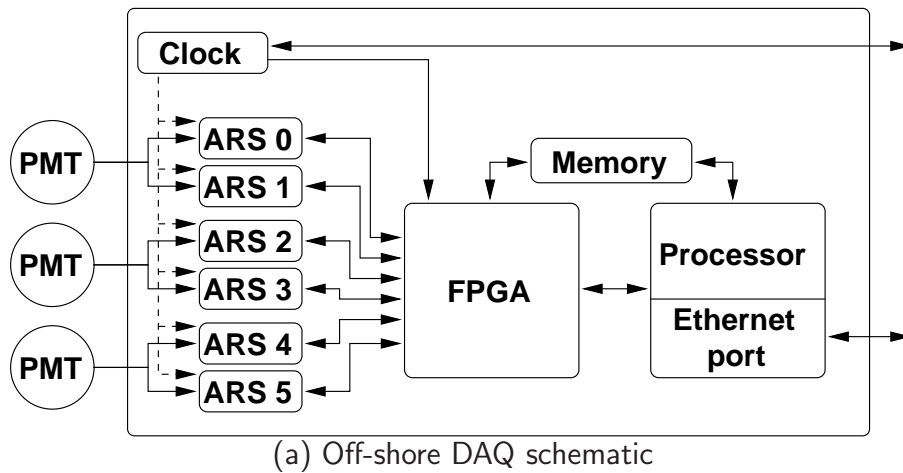


**Figure 5.3:** Schematic of the off-shore DAQ hardware (a) and photograph of the interior of the LCM (b). In the shown configuration, four ARS boards, as well as instrumentation boards for the acoustic positioning, are integrated, whereas no DAQ board is present. In the rear of the boards, the backplane with connectors for the boards and PMTs is visible.

The signals of the PMTs are read out and digitised in custom-designed *Analogue Ring Sampler (ARS)* chips [72]. The ARS digitises the signal in either of two modes: In the standard or *single photo-electron (SPE)* mode the signal charge is integrated within an adjustable time window (typically 35 ns) and sent to the DAQ board if a predefined threshold (typically the equivalent



of 0.3 photo-electrons to suppress electronics noise) is reached. In the second or *analogue waveform (WFA)* mode, the shape of selected PMT pulses can be digitised with adjustable sampling frequencies of up to 1 GHz. Each PMT signal is time-stamped by an internal clock with an  $\approx 0.5$  ns accuracy. As the amount of data for an event recorded in the WFA mode is a factor of 45 times bigger than for one event in SPE mode without much gain in information, the ANTARES detector usually takes data only in SPE mode. For optical neutrino telescopes such a simple threshold trigger in the SPE hits in each sensor together with coincidence filters on-shore are sufficient to efficiently identify physically interesting events in the data. For certain calibration runs the surplus on information in the WFA mode is used and thus WFA events recorded. To overcome the ARS dead-time of 200 ns after the sampling, a second ARS chip takes over if the first one is blocked. The two ARS chips for one PMT, together with peripheral electronics, are integrated on one ARS board, of which there are up to four in an LCM - three for the PMTs and one for a light calibration source at roughly every fifth storey (cf. previous section). Via the backplane the ARS chips communicate with the *Field Programmable Gate Array*<sup>4</sup> (FPGA) of the DAQ board (a Xilinx Virtex-E) in a dedicated data format. The FPGA buffers and converts the data into an ANTARES specific format which is then sent to shore by the processor. The data are combined on-shore to *time slices*, where each time slice holds the events from all sensors which occurred within a predefined time interval. The length of a time slice is adjustable, at the time of writing a value of 0.1049 s was used.

All LCMs are synchronised via a distributed clock system with a main GPS controlled clock at the shore station, which distributes a 20 MHz clock signal with an absolute accuracy of 100 ns. This signal is received at a *clock board* in every LCM and used to start, stop and synchronise data-taking and the ARS internal clocks. Delays due to the different path-length of the optical clock signal can be determined via a return pulse sent by the local clocks.

Additionally, some boards for additional devices at the storey and for system monitoring are included in the LCM. The *compass board* houses a tiltmeter and a compass and is a vital part of the positioning of the sensors (cf. previous paragraph). It also measures environment parameters inside the LCM, like temperature and humidity. Additional boards are used for instruments like the acoustic positioning sensors.

## 5.2 Acoustic Particle Detection in ANTARES

The ANTARES detector not only serves its main goal to detect cosmic neutrinos, but is also installed to act as a research infrastructure for the investigation of the deep sea environment. Among others, the activities in that area include a seismometer to record earthquake waves at the sea floor and the usage of the ANTARES detector to correlate the sea current with the bioluminescence activity of bacteria or crustaceans.

However, the largest addition to the ANTARES detector is physically motivated: The AMADEUS<sup>5</sup> project [73] which is the subject of this work. It incorporates the installation of acoustic sensors

---

<sup>4</sup>A chip with hardware programmable logic components.

<sup>5</sup>Abbr. for *ANTARES Modules for Acoustic DEtection Under the Sea*.

to study the detection of neutrinos using the method introduced in Sec. 2.3. As has been already pointed out, this system acts as a precursor experiment to evaluate the feasibility of building a future acoustic neutrino detector. For this study, the ANTARES detector with its deep-sea infrastructure provides an unmatched opportunity. Several studies of acoustic particle detection were and are conducted all over the world in sea and lake water, ice and salt [16,17,74], however, so far only the AMADEUS project incorporates all inter-sensor distances adapted for a future detector: local sensor clusters consisting of more than three sensors with a 1 m-spacing to suppress random noise correlations and to apply local data processing algorithms, and in the same setup cluster spacings of several hundred meters needed to efficiently instrument a large volume. The actual length scales between sensors in this setup range from 1 m to 340 m. Within the framework of the ANTARES detector all data-taking can be performed without interruption and continuously for several years and thus long-term studies can be performed. Therefore, all the questions which are connected to the feasibility and performance of an acoustic detector can be pursued with AMADEUS in a setup close to that of an actual acoustic detector for UHE neutrinos, if of course much smaller. Additionally, a search for hybrid events in the optical detector and the acoustical setup is possible.

In agreement with the ANTARES collaboration, a total of six storeys of the ANTARES detector will be equipped with acoustical, instead of optical, sensors. The total of 36 acoustic sensors are read out continuously by a modified ANTARES data-acquisition at a sampling rate of more than 100 kSamples/s. The exact setup of the AMADEUS extension to ANTARES is described in Chapter 6. Three storeys are attached to the IL07 and operated since December 2007, three additional ones are integrated into L12 and are installed in 2008.

### 5.2.1 The AMADEUS-0 Project

In order to gain experience in designing, constructing and operating a sensor system for acoustic measurements in the deep-sea, as well as acquiring and analysing data from the ANTARES site, the AMADEUS-0<sup>6</sup> project was initiated in 2004. The main contribution to that project discussed in this work was in the DAQ software and hardware – the gain in experience was used later for the design and calibration of the AMADEUS DAQ system.

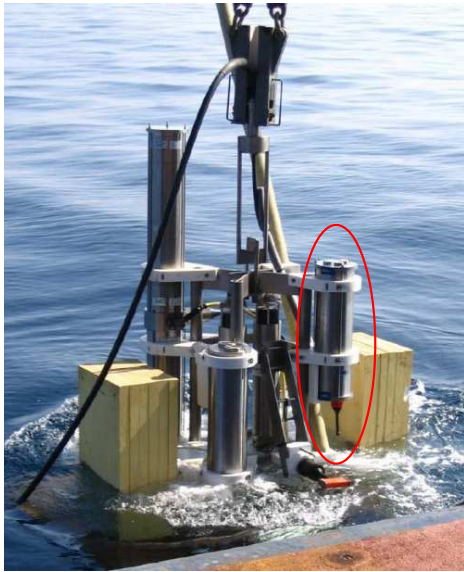
For the setup, a Titanium electronics container – usually housing the LCM – was used, equipped with five custom-designed piezo-ceramic sensors (cf. the acoustic modules in Sec. 6.1.1) and commercial hardware for the DAQ. Batteries ensured autonomous operation of the module for several hours. Due to the given geometry of the container the sensor spacing is in the order of 10 cm, which is not sufficient for the reconstruction of the direction of point sources in the data. Additionally, the housing of all sensors and the electronics in the same container leads to significant crosstalk between the individual components, degrading the data quality.

AMADEUS-0 (cf. Fig. 5.4) was operated autonomously at the BSS of a mechanical test string (*Line 0* [75]) during two data-taking periods. The first phase took place during the sea operation for the installation of the line at the ANTARES site on the 15<sup>th</sup> of March, 2005, lasting for almost 5 hours. The second set of data, 3.5 hours on the 15<sup>th</sup> of April (until the depletion of

---

<sup>6</sup>Abbr. for *Autonomous Module for Acoustic DEtection Under the Sea at Line 0*.

the batteries), was taken while the line was in continuous operation on the sea floor.



(a) AMADEUS-0 at the BSS of Line 0



(b) DAQ part of AMADEUS-0

**Figure 5.4:** Photographs of the AMADEUS-0 system attached to the BSS of Line 0 (a) at the installation and the DAQ system (b) without the surrounding Titanium cylinder that holds the sensors. The lower part of the DAQ system (red) contains the batteries, the middle part holds the DAQ hardware for read-out, digitisation and storage of the sensor data. When the system is closed the sensors are positioned between the red rings in the upper part.

The system characteristics were comparable to the ones used in the AMADEUS project, which are described in the next chapter. The data were sampled at 500 kSamples/s, i.e. one data point with 16-bit accuracy every 2  $\mu$ s. The sampling rate was divided evenly over the sensors read-out, e.g. it was possible to record the data of one sensor at the full rate or all five sensors at 100 kSamples/s. The piezo-electric sensors had a two-stage amplifier with a built-in bandpass filter from 1 to 100 kHz and an overall sensitivity of  $-120$  dB re 1V/ $\mu$ Pa (equivalent to 1V/Pa). The system operated within its expected potential. A huge variety of transient signals, e.g. from the pingers of the ANTARES acoustical positioning system, and background noise were recorded. Exemplary results are shown in Fig. 5.5.

The recorded amplitudes (cf. Fig. 5.5(a)) represent a gaussian white noise ( $\sigma \approx 54$  mV) with extensions to higher voltage amplitudes due to transients of higher amplitude. The recorded noise spectra vary with time and exhibit a steeper roll-off towards higher frequencies than expected from the ambient noise parametrisation in the frequency range between 10 and 20 kHz (cf. Fig. 5.5(b)) – a point to be studied with the AMADEUS setup. However, due to the complicated sound path within the module a complete calibration – especially directional sensitivity – was not feasible and thus it could not be determined whether the source of the deviation was of electrical origin or actual sea noise. The system is not sensitive to the ambient noise above frequencies of  $\approx 25$  kHz mainly due to the inherent noise of the electronics.

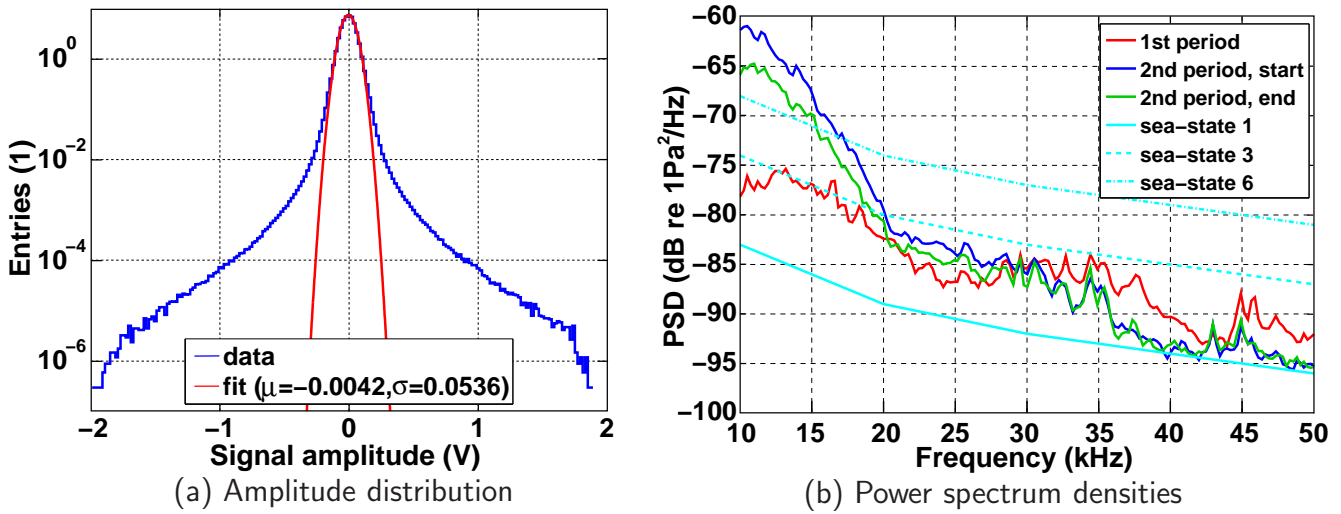


**Figure 5.5:** Selected analysis results for AMADEUS-0 data: normalised histogram of amplitudes for all recorded data (a) (quality cut applied) and noise spectra for different periods of data-taking with different weather conditions (b). For comparison the predictions for different sea conditions from [42] are given. The actual sea-state during the first period was SS1, for the second period the sea-state varied between SS3 and SS5. Both figures were adapted from [55].

A systematic analysis of the data recorded by AMADEUS-0 can be found in [55], where studies of the variation of the background noise were conducted and data filtering techniques were developed and tested on the data. The description of the sensors and figures of exemplary transients can be found in [48].

The operation of the system revealed several possibilities for improvement which were considered in the AMADEUS system, even though the new system has a completely different setup and hardware. For example the crosstalk between channels – both acoustically through the coupling to the same container and electronically between the sensors and the DAQ hardware – posed an obstacle for the reconstruction of directions in AMADEUS-0. In AMADEUS the channels are separated physically at the sensor level and electronically at the data-acquisition level. The electronics noise at high frequencies proved to be a bigger problem than expected and is suppressed in the later design by a low pass filter of high order. The system stability was not satisfactory as well, which is an important issue as the AMADEUS system is operated inaccessibly in the sea. The most important lesson learned from AMADEUS-0 is that the ambient noise level of the deep-sea is as expected, which gave the basis for the dimensioning of the sensor sensitivity and post-amplification gain in AMADEUS (cf. Secs. 6.1.1 and 6.2).

# Chapter 6

## The AMADEUS Project

The aim of the AMADEUS project<sup>1</sup> is to integrate acoustic sensors into the ANTARES framework in order to study acoustic particle detection in the deep sea with a dedicated setup. A total of six storeys on two lines of the ANTARES detector are equipped with six acoustic sensors each. The 36 acoustic sensors are continuously read out at more than 100 kSamples/s by a modified ANTARES data-acquisition system. The distances between sensors in that setup range from 1 m to 340 m, which is comparable to a potential future neutrino detector employing the acoustic detection method.

In this chapter the AMADEUS setup will be described in detail with special attention to the off-shore DAQ hardware, the main contribution of this work to the AMADEUS project.

### 6.1 The AMADEUS Setup

To use the full potential of the framework provided by the ANTARES detector it was decided, in an early stage of the development of the AMADEUS project, to use as much standard hardware and mechanical structures of the detector as possible. The DAQ infrastructure provides the requirements needed for the continuous transmission of data from the sensors to the shore, and the mechanical structure of a storey only needs minor modifications to house acoustic sensors. The major modification lies in the off-shore DAQ hardware, where the ARS boards have to be substituted by the so called *AcouADC boards* to digitise the sensor signals. The design, development and characterisation of the AcouADC board was the main aspect of this work and will be in focus for the rest of this document.

A schematic of the AMADEUS setup and photographs of *acoustic storeys* are shown in Fig. 6.1. Three of the acoustic storeys are additions to the instrumentation line IL07, which holds a total of 6 storeys (acoustic storeys at positions 2, 3 and 6 counted from the bottom storey). Here it was possible to deviate from the standard storey spacing of 14.5 m to have different length scales in vertical direction. The topmost storey 6 is installed at the maximum feasible distance of 110 m above the middle one (storey 3). The bottom storey 2 is located 14.5 m beneath storey

---

<sup>1</sup>Overviews on the project are also given in [63,73,76,77]; studies towards the realisation and individual parts of the projects are described in [15,48,54,55,78,79].

3 and 180 m above the sea bed, suppressing and delaying reflections of transients and surface generated noise from the ground. The other group of three storeys completing AMADEUS substitute optical ones on positions 21 to 23 at the detection line L12. The lowest acoustic storey on that line is positioned at a height of 390 m above ground, the others following at the nominal spacing of 14.5 m. L12 was chosen for its horizontal distance of 240 m from the IL07 – the maximum possible within the ANTARES detector – and because of the project schedule. As a consequence the maximum horizontal and the maximum vertical sensor spacings in the setup are each 240 m. The range of distances for studies of background behaviour, and as lever arms for a source reconstruction is therefore from below 1 m inside the storey up to 340 m from the bottom of IL07 to the top of L12. In this setup the sensors are operated at depths from 2050 to 2300 m below the sea surface.

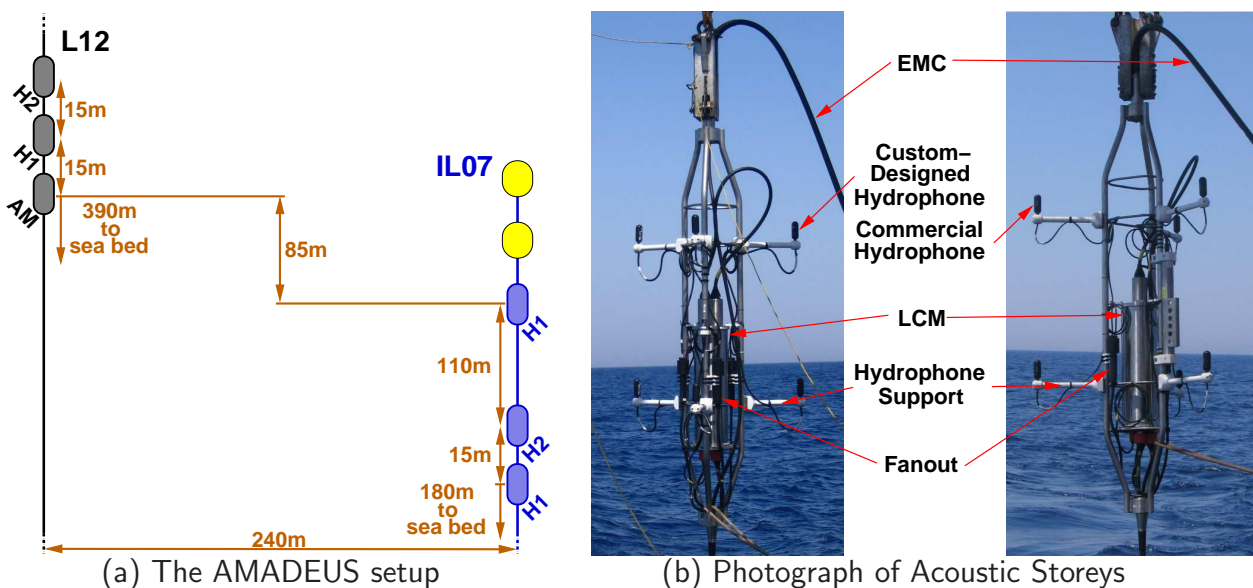


**Figure 6.1:** Schematic of the AMADEUS setup (not to scale, (a)) and photographs of two acoustic storeys on the instrumentation line IL07 (b). Only acoustic storeys are shown in (a), optical ones have been left out. The storeys labelled *H1* are equipped with commercial hydrophones (as shown in the right photograph in (b)), the ones labelled *H2* with custom-designed sensors (left photograph in (b)). The storey labelled *AM* holds acoustic modules.

### 6.1.1 Acoustic Sensors

For the AMADEUS project acoustic sensors are used on the storeys replacing the ANTARES PMTs. The sensors used in the AMADEUS setup are piezo-ceramic based, utilising the piezo-electric effect of certain ceramics with asymmetric lattices. Those materials develop a difference in the electric potential between faces if subjected to pressure variations. Over wide ranges of pressures, there is a linear correlation between the force applied and the electric potential difference between two opposing sides, with coefficients typically in the order of  $\mu\text{V}/\text{Pa}$ .

The characteristics of those ceramics with respect to the application in AMADEUS were simulated in a study with a finite element approach with the aim of finding the best suited material and geometry of the sensor [78]. For the development of the sensors actually used, an extensive design study was conducted [48,80,81]. The sensors chosen for the integration into ANTARES were calibrated and the sensitivity was fitted following an equivalent circuit diagram model, which can also be applied to predict the acoustic properties of piezo-ceramics. In this model the dynamical properties of a piezo-element are described by its electrical ones (like resistivity, capacitance and inductance).

Two types of sensors were built and thoroughly tested and calibrated: *hydrophones* and *Acoustic Modules (AM)*, cf. photographs in Fig. 6.2.



**Figure 6.2:** Photographs of the sensors used in AMADEUS. From left to right: Custom-designed hydrophone, commercial hydrophone and Acoustic Module (AM). The AM is a prototype with three active elements mounted in a mechanical structure for calibration measurements.

Both types employ a piezo-ceramic with an attached two-stage amplifier (gain  $\approx 50$  dB). In the case of the hydrophone, this active element is coated with plastics - a standard procedure for deep-sea acoustic sensors. For the AMs two sensors are glued to the inside of the glass sphere usually housing the PMT. This alternative sensor design is driven by the idea of shielding the sensor from the constant high pressure of the deep sea while sound waves are still able to couple through the glass into the sensor. It presents the promising future option to combine optical and acoustic sensors in one vessel, especially with regard to the hybrid optical/acoustic detection mentioned before. This method was already applied and successfully tested in AMADEUS-0. The sensitive frequency range is matched to the one of acoustic particle detection from 1 to 50 kHz (up to 100 kHz for the AM-sensors) with an average sensitivity of  $-140$  to  $-145$  dB re  $1\text{V}/\mu\text{Pa}$  ( $0.05$  to  $0.1$  V/Pa) at an inherent noise level of  $-105$  to  $-120$  dB re  $1\text{V}/\sqrt{\text{Hz}}$  ( $1$  to  $5$   $\mu\text{V}^2/\text{Hz}$ ). The pressure tightness of the sensors was evaluated in pressure tests and the hydrophones found to be fully functional after an exposure of up to 310 bar. Nonetheless, the pressurisation up to 250 bars at the sea is considered the main single

point of failure for the sensors, as the electronics in the sensors is highly reliable. Since one aim of the AMADEUS project is to test different sensor designs, adapted commercial deep-sea hydrophones (High Tech, Inc., 90 series [82]) were selected, tested and integrated. These hydrophones were also calibrated and were found to have a slightly smoother directional sensitivity and less inherent noise (by 10 dB) at an  $\approx 5$  dB lower overall sensitivity. A comparison of the overall sensitivities (direction averaged) for one custom-designed and one commercial hydrophone is shown in Fig. 6.3.

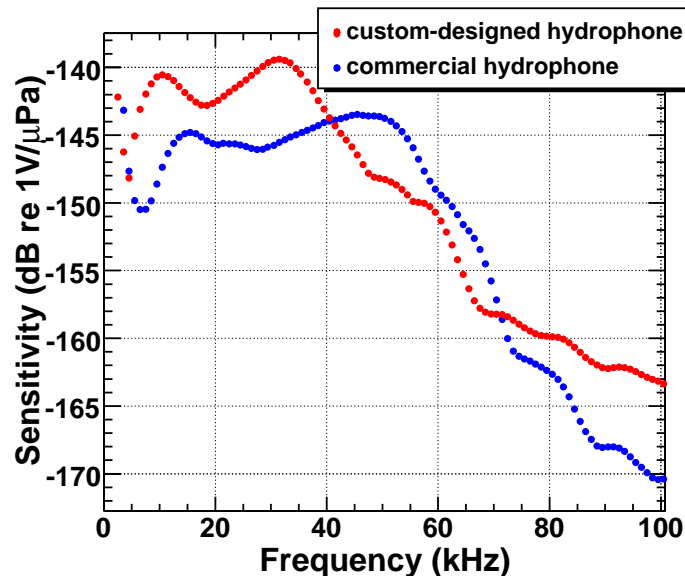


**Figure 6.3:** Overall sensitivity of one custom-designed hydrophone (red) and one commercial hydrophone (blue). The data are results of a calibration measurement from [48], which is not valid below 10 kHz.

The sensitivity of the custom-designed hydrophone shows in general more pronounced features than the one of the commercial hydrophone. The resonance structure of the piezo-element is clearly visible with a global maximum (main resonance) at 31 kHz and 45 kHz for the custom-designed and commercial sensor, respectively. Below that frequency the sensitivity is basically flat within 3 dB. The features below 10 kHz are caused by the calibration procedure. Above the main resonance the sensitivity drops by  $\approx 3$  to 6 dB per 10 kHz.

The directional sensitivity of a commercial hydrophone is shown in Fig. 6.4.

The sensitivity differences in the horizontal plane, displayed in the left plot, are low. Even when considering the frequency at the main resonance of the piezo-ceramic at 45 kHz, where the sensitivity is highest, the differences in sensitivity between all azimuthal angles are below 2 dB. Thus the hydrophone can be considered to have uniform sensitivity in the horizontal plane. In the vertical plane, displayed in the right plot of Fig. 6.4, the variation is higher, but mainly at frequencies above 60 kHz, where the overall sensitivity drops. For these frequencies the sensor is sensitive primarily in the upward direction. At polar angles exceeding  $165^\circ$  signals are shielded by the sensor cable and electronics.



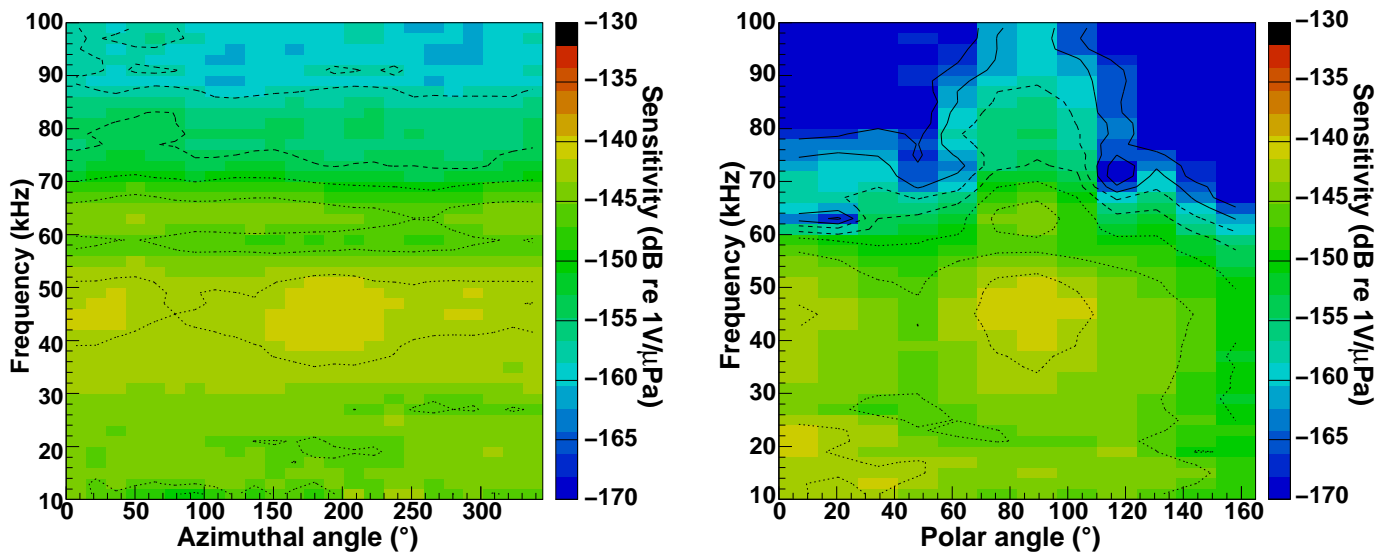


**Figure 6.4:** Directional sensitivity of a commercial hydrophone used in AMADEUS: the sensitivity for rotation in a horizontal plane (at  $90^\circ$  polar) (left) and a vertical plane (at  $0^\circ$  azimuth) (right). The z-axis of the hydrophones is defined as vertical upwards as pictured in Figs. 6.1(b) and 6.2, i.e. an polar angle of  $90^\circ$  defines the horizontal plane. Adapted from [48].

The directional sensitivity behaviour reflects the complicated signal generation in acoustic sensors, which has to be taken into account when analysing acoustic signals. The shape such a signal is distorted by the sensors, which is demonstrated for a bipolar signal in Fig. 6.5. The performance of the sensors within the AMADEUS system is described in the last part of this work.

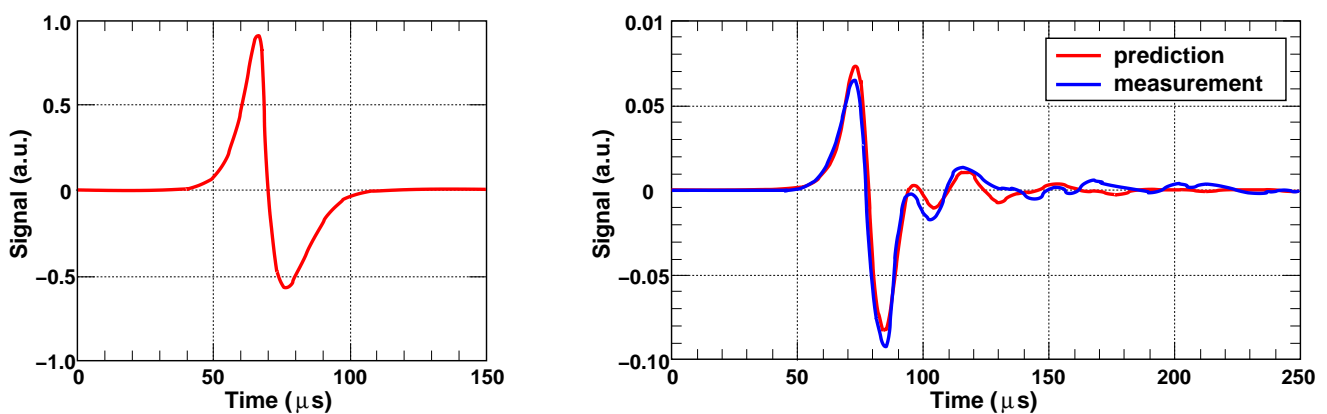


**Figure 6.5:** Response of a hydrophone to a bipolar signal. A pulse that produces the bipolar signal (shown left) in water is sent via a transducer. The recorded signal is compared to a prediction (shown right) taking into account the hydrophone sensitivity and the sender characteristics. Adapted from [48].

For the attachment of the sensors to the storey plastics hydrophone supports were constructed and, as one PMT was substituted by two sensors, a deep-sea cable fanout was devised. In that connector the cables of two hydrophones are merged into one cable fitting to the plug in the LCM container.

The hydrophones on IL07 are all aligned pointing upwards, as the most interesting source of background noise – the sea surface – is in that direction. Additionally the distance to the surface is by far bigger than to the ground, such that a bigger volume can be monitored. All signals originating at distances beyond  $\approx 10$  m are recorded at the same polar angle and thus at similar sensor sensitivities. This results in similar shapes of the uncalibrated signals, which can be used in on-line filtering. The commercial hydrophones on one storey of L12 will be aligned pointing downwards to study a possible shielding of the surface generated noise (cf. Sec. 12.2). Within the storey the six sensors are aligned in two horizontal, isosceles triangles, one atop the other. The two layers are separated vertically by 0.85 m and the distances between two sensors within one layer are around 0.90 m, giving a maximum distance within the storey of 1.2 m [83]. The two sensors atop each other are read out by the same AcouADC board. In the AMs, the sensors inside the spheres are attached in the horizontal plane, at the maximum circumference of the three spheres. The sensors inside one sphere are separated by  $45^\circ$  and read out by the same AcouADC board.

From considerations of the power consumption within the storey and the available voltages provided by the LPB, the hydrophones are powered by a DC voltage of 6.0 V. Their unclipped differential output signals range up to 2.5 V above or below the reference voltage of 3.0 V; the loss in range from 6.0 V to 5.0 V is due to the operational amplifiers used in the two-stage amplifiers. The unclipped dynamic range of the sensors for transients is from their equivalent inherent pressure noise in the order of mPa (cf. Sec. 10.2) up to  $\approx 100$  Pa.

## 6.2 The AcouADC Board

As the time scales in acoustic particle detection are three orders of magnitude larger than the ones in optical neutrino detection, and due to the completely different signal generation in the sensors, the digitisation of the acoustic sensors could not be done by the ARS boards used in ANTARES. Especially the low resolution of the ARS chip (8-bit) is not sufficient for the digitisation of acoustic signals and the design of the ARS chip does not allow for continuous untriggered data-taking. Thus the AcouADC board [84] was constructed to substitute the ARS board and read out the signals of two sensors, i.e. one AcouADC board incorporates two sensor *channels* (abbr. *ch0* and *ch1*). As the purpose of AMADEUS is to comprehensively evaluate the acoustic properties of the deep sea, the board was designed to be as flexible as possible, but at the same time to match the general conditions set by the acoustic particle detection method. The board has to fulfil at the same time the requirements for the data transmission and for the power consumption, set by the LCM environment. The main requirement for the board is the stable operation with low external interference over several years, as it is not accessible once installed in the storeys.

An LCM equipped with AcouADC boards is shown in Fig. 6.6.

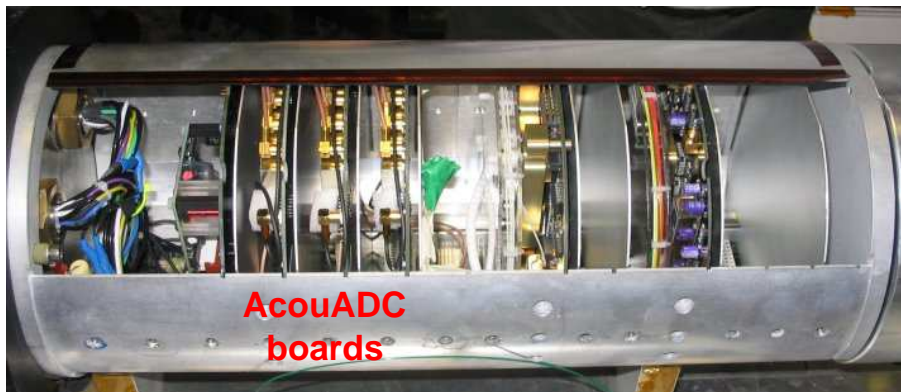
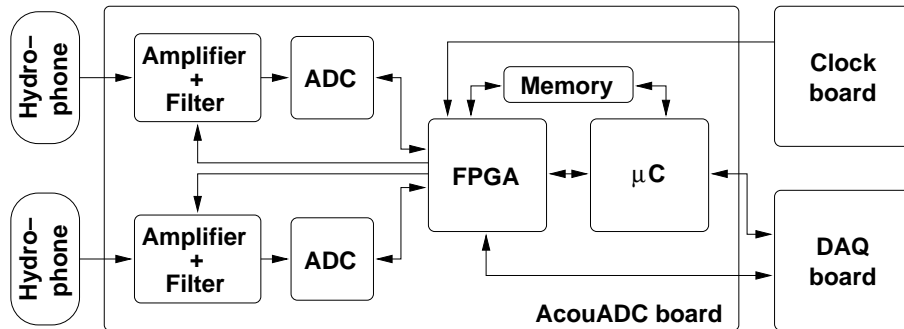


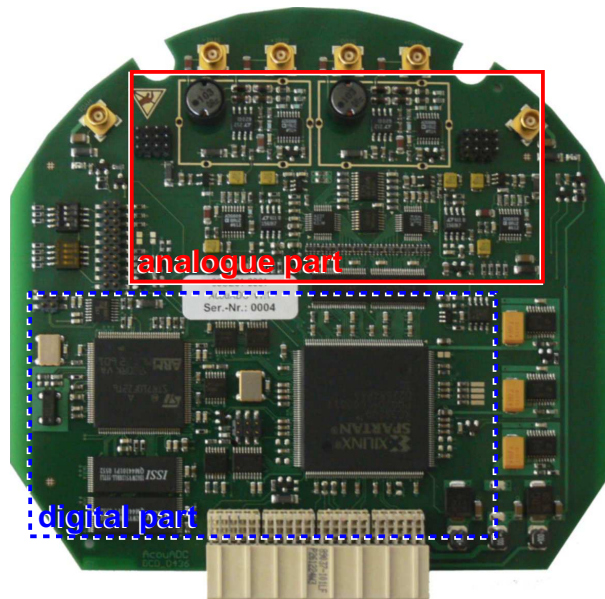
**Figure 6.6:** Fully integrated LCM for an acoustic storey of IL07. The ARS boards have been substituted by three AcouADC boards. The mechanical support structure is half closed and the outer Titanium cylinder has not yet been mounted.

The board design started early in 2006 and a first version was produced in the same year by a contractor [85]. This prototype version was extensively tested in the lab and minor changes had to be included in the final design of the board. This second version was produced early in 2007 and thereafter tested and found to match all requirements. The 18 boards needed for AMADEUS – including spares in case of a defect – were calibrated and the integration of the boards for the IL07 finished by mid 2007. The integration of L12 is scheduled early in 2008.

As there were a lot of requirements to be complied with, the composition of the board is rather complex – see Fig. 6.7. It comprises of two parts: an analogue one and a digital part. The analogue part amplifies and filters the sensor signal with adjustable settings. The resulting signal is digitised in an *analogue-to-digital converter* (ADC) and read out by the digital part. This part converts the digitised signal into the ANTARES data format and transmits it to the ANTARES DAQ board from where the data are sent to shore. The AcouADC board not only had to emulate the ARS board in the DAQ scheme, it also had to stay within the specifications for the power consumption of that board. Therefore the voltages used in the board and the single components had to be carefully chosen from the maximum allowed current drawings from the LPB. This goal was reached with a low power consumption of typically 1.8W [86].



(a) Off-shore DAQ schematic



(b) Photograph of an AcouADC board

**Figure 6.7:** AMADEUS off-shore DAQ hardware. Schematic of the off-shore DAQ hardware (a) and photograph of a first version of the AcouADC board (b). The shown AcouADC board does not vary much from the final design board used in the experiment but has no shielding cage above the first stage amplification (at the two rectangular areas surrounded by metal strips at the top of the board) and was chosen for better visibility.

### 6.2.1 Analogue part

In the analogue part of the AcouADC board, the differential signals coming from the sensors are filtered and amplified. The bandpass filter used is matched to the frequency range of interest ranging from about 1 kHz to about 100 kHz. The frequencies below 1 kHz, where the background noise of the deep sea rises due to the wave interactions and noise from human sources, are cut by a third order high-pass filter with a cut-off frequency of  $\approx 2$  kHz. High frequency components are suppressed by a steep 10<sup>th</sup> order root-raised cosine filter to eliminate aliasing effects of the digitisation, while keeping the passband as wide as possible. This filter suppresses

especially the high-frequency electronics noise, which provided a problem in AMADEUS-0. The selected active frequency range meets the one of acoustic neutrino detection, as well as the sensitive region of the hydrophones, which of course have also been designed and chosen for this application. The signal of the acoustic sensors can be amplified by 12 adjustable gain settings. The amplification is done in a two step procedure, using two separate amplifier stages utilising switched resistor chains. The first stage was designed with as low inherent noise as possible. A value below  $-120 \text{ dB re } 1 \mu\text{V}^2/\text{Hz}$  ( $1 \mu\text{V}/\sqrt{\text{Hz}}$ ) was reached, well below the inherent noise of the sensors. In the first stage coarse amplification factors of 1.00, 10.0 or 100 can be set. In the second stage, the gain factor can be chosen between 1.00, 1.78, 3.16 and 5.62, spanning a total amplification range from 1.00 to 562 (dubbed *G1* to *G562*) or 0 to 55 dB. Thus acoustic signals and noise in a wide amplitude range can be studied undistorted and without clipping. The high gains above a factor of 100 were integrated to be able to compensate for an unexpected loss of sensitivity of the sensors in the sea.

The filtered and amplified analogue signals are digitised by the ADC with a sampling rate of 500 kSamples/s (resolvable frequency components of up to 250 kHz) or one sample every  $2 \mu\text{s}$  with 16-bit accuracy. The digital output code levels (binary two's complement) start at  $-32768$  *least significant bits* (LSB) and end at 32767 LSB with a total of 65536 steps, which are mapped to the input range of the ADC from  $-2$  to  $+2$  V. This results in voltage steps of  $0.061 \text{ mV/LSB}$  width. The reference level of the signal can be chosen between  $+0$  V (*full range*, labelled R0) and  $-1$  V (*half range*, labelled R1). The first setting uses the full range accessible from the analogue part symmetrically, the second was introduced after an examination of prototype boards and finding of discontinuity of the ADC sampling around 0 V. This discontinuity can be deconvoluted from the signal by the performed system calibration. However, this is a time consuming process and can thus only be done off-line. Therefore, if an exact signal shape is necessary on-line, e.g. to test special data filtering algorithms, the second setting can be chosen.

In the analogue part, the  $6.0$  V power supply to the hydrophones is filtered, which is necessary as these devices are sensitive even to low noise on the supply voltage. Also the power can be switched on and off and a resettable fuse triggers, if the hydrophone draws too much current, to protect the LCM electronics – e.g. in case of a water penetration into the sensor. All the settings of the analogue part can be set at the beginning of a data-taking run from the shore via the digital part of the AcouADC board.

Acoustic signals that lie fully in the frequency range of the passband can thus be recorded undistorted and unclipped by the electronics up to a peak-to-peak amplitude of  $40 \text{ Pa}$  (gain 1) or  $70 \text{ mPa}$  (gain 562)<sup>2</sup>. This value is highly dependent on the frequency components of the signal and is only presented as a benchmark.

A detailed description of the analogue part and its characterisation and calibration is given in Chap. 8.

---

<sup>2</sup>These values have been calculated for the typical sensitivity of the sensors of  $-140 \text{ dB re } 1 \text{ V}/\mu\text{Pa}$  ( $0.1 \text{ V/Pa}$ ).

### 6.2.2 Digital part

The digital part mainly consists of an FPGA (Xilinx Spartan-3 series), a microcontroller ( $\mu\text{C}$ , STMicroelectronics STR71xF series) and several volatile and non-volatile memory components. The FPGA handles the data from the sensors and all the DAQ communication. It transforms the data into the ANTARES data format, starts and stops transmission triggered by the clock board and adjusts the settings of the analogue part. As it was chosen to fully integrate the AMADEUS data-taking in the ANTARES DAQ scheme, the AcouADC board emulates an ARS board with respect to the DAQ board. In the present phase the sensor signals are sampled continuously and transmitted using the waveform (WFA) data format, which is different to the ARS boards where waveforms are only sent when a predefined condition is fulfilled. However, with a better understanding of the acoustic signals in the deep-sea, it will also be possible to use the variability of the FPGA and to preselect interesting signals, or even to send only some of their characteristics, in analogy to the SPE events of the PMTs. The FPGA also processes the data further, with currently four different settings for downsampling of the data being integrated: the first – dubbed downsampling 1 (*DS1*) – transmits the data in the ANTARES data format without downsampling. The second (*DS2*) resamples the data by a factor of two by the usage of a *finite impulse response filter (FIR)*, i.e. to at a rate of 250 kSamples/s or 125 kHz. Thirdly, there is the possibility to downsample the data by a factor of 4 – to 125 kSamples/s or 62.5 kHz, again implemented by a FIR filter. One last setting, dubbed *DS0*, disables the data transmission from the FPGA to the DAQ board. The data-taking and start/stop of the data transmission by the FPGA is synchronised by the 20 MHz ANTARES clock signal, its 50 ns relative and 100 ns absolute accuracy being more than sufficient for the minimum sampling interval of 2  $\mu\text{s}$ .

The code of the FPGA is freely programmable from the shore, which is done via the  $\mu\text{C}$ , which also receives the settings for the FPGA and analogue part from the on-shore detector control. While the later procedure is done at every start of a run and only takes a few seconds time, the transmission of programming code is time consuming - up to several minutes per board and will only be done if necessary. The  $\mu\text{C}$  is therefore the instance responsible for the slow control communication. Once installed its programming and settings are not changeable.

## 6.3 Data-taking Scheme and Standard Settings

The data-taking scheme for AMADEUS was designed to be fully integrable in the ANTARES scheme, using the same hard- and software. For the commissioning phase of the project it was opted to clone the ANTARES DAQ hardware and use a separate scheme for AMADEUS. This was done to gain experience with system behaviour and also with the data to expect. With this separation no part of the ANTARES experiment is impeded or interfered by the acoustic setup. The connection to the AMADEUS storeys is established by a separate server in the shore station, where a separate RunControl programme to control the DAQ is running. The data are filtered by a second server and stored first to disk and later to a high performance storage system at a computing centre [87]. For more details on the data-taking scheme, especially the software and filter algorithms installed, cf. [54].

For tests of the system and the first phase of data-taking a collection of standard settings based on the experience gained in the laboratory and with the AMADEUS-0 system was defined. A sensitivity of  $-120$  dB re  $1\text{V}/\mu\text{Pa}$  has proven to match the ambient noise and digitisation range settings. To reach this, a gain factor of 10 (G10, 20 dB) was defined as standard since the average sensors sensitivity is around  $-140$  dB re  $1\text{V}/\mu\text{Pa}$ . This leaves still a wide range for examining both high energetic signals, e.g. the acoustic pingers, and low power signals, e.g. the low background noise at low wind speeds. For a first glance at the data without much need for calibration the half range setting (R1) is chosen.

A downsampling factor of 2 (DS2) is sufficient to study the background noise up to 100 kHz, where the sensors have already lost most of their sensitivity. At this downsampling factor the data rate of each storey is  $\approx 20$  MBit/s, approaching the maximum transfer rate set by the Ethernet port of the DAQ board. For the IL07 the total data rate amounts to 10 MByte/s, which has to be filtered on-line; for the whole AMADEUS setup the data volume doubles.





## **Part III**

# **Characterisation of the AcouADC Board**



# Chapter 7

## Calibration Setup

The transients and background noise in the deep sea, which are of relevance for a study of acoustic particle detection, cover a broad frequency range and exhibit a huge variety of signal shapes. Therefore a precise understanding of the data-acquisition hardware, concerning the frequency behaviour and signal distortion in the signal path from the sensors to the digitisation, is essential. This is achieved by calibrating the hardware – and here especially the AcouADC board as its main part. The calibration is also a good means to find defects in the board.

The AcouADC card is a complex electronics system (cf. Sec. 6.2), consisting of several components in the signal path that affect the signal properties. The components are highly integrated and interdependent and thus not separable for the calibration. A set of calibration measurements was conceived to calibrate the boards for all possible settings. The goal of the calibrations was a better than 10% accuracy for all parameters (below 1% for most), such that the major uncertainty in the determination of the acoustic signal is governed by the complex response of the sensors and not by the DAQ hardware.

In this chapter the calibration setup and the measurements performed are described, whereas the algorithms for deducing the system transfer functions and the results are presented in the following chapter.

### 7.1 Calibration Setup

The calibration measurements were performed separately for each AcouADC board and each sensor channel in a reduced LCM electronics surrounding, where only the boards necessary for data-taking were integrated. Included was a DAQ board in a backplane powered over the LPB by an external power supply at 48.0V, instead of the high voltage (380V) used in ANTARES. Clock signals were provided by a *pseudo clock board*, which generates the necessary clock pulses using quarzes with sufficient relative precision, but without the GPS timing and absolute precision.

This reduced setting was chosen for simplicity and to minimise the interference of the DAQ hardware with the measurements which have to be valid down to the sub-mV range in form of induced noise. Intensive tests were performed after the calibration with AcouADC boards

in fully equipped LCMs and in the complete IL07 setup at ANTARES integration sites. Those tests showed only minor changes in the noise characteristics of the boards, but did not indicate the need for a new calibration in the full setup, showing the overall validity of the performed measurements (cf. Chap. 9 and 10).

For each board several DC characteristics – like supply and reference voltages – which were needed for the determination of the system functions were measured. Each characteristic deviated less than 5% from its nominal value with a negligible variation between the individual boards.

A schematic of the setup used for the AcouADC board calibration is shown in Fig. 7.1.

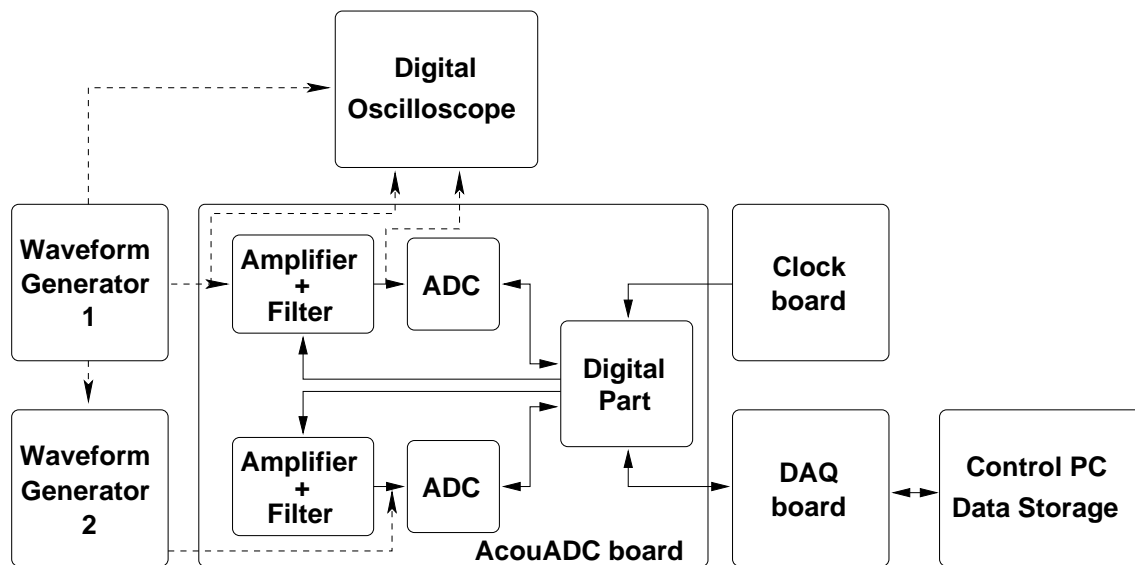


**Figure 7.1:** Schematic of the setup for the calibration of one channel of the AcouADC board, described further in the text. The DAQ schematic is simplified from Fig. 6.7(a). All measurements taken and signals sent for the board calibration are marked by dashed lines.

Two 20 MHz digital arbitrary waveform generators were used, one to produce the differential input signal for the channel of the AcouADC board under test and the other for a trigger signal for timed measurements. The trigger signal – a rectangular signal of 1  $\mu$ s width – was capacitatively coupled directly into the ADC of the channel which was not under test, avoiding the phase delay in the amplifier/filter part. Analogue measurements were performed with an 8-bit, 5 GSamples/s digital oscilloscope, digital ones with the DAQ hardware and a control PC which also acted as data storage.

Measurements with three different input stimuli – described in the next section – were performed with varying settings of the filter/amplifier part. The mean ( $\mu$ ), peak-to-peak (abbr. *pp*) amplitude and standard deviation ( $\sigma$ ) of the signals were measured at the input of the AcouADC board and directly at the input of the ADC with the oscilloscope for each measurement. The two channels on each board were stimulated consecutively and the resulting data were recorded with the DAQ for different settings of the downsampling and input range of the ADC. The setup

was designed such that there were no significant delays between the channels of the board and the oscilloscope ( $\ll 0.1 \mu\text{s}$ ). The absolute phase response can thus be deduced directly from the calibration.

The parameters measured with the oscilloscope were corrected for the noise of the instrument by fitting quadratically added noise contributions of the oscilloscope ADC (the volt equivalent of 1 bit) and a constant inherent noise of  $\approx 2 \text{ mV}_\sigma$ . This was necessary as the AcouADC board has substantial less inherent noise than an oscilloscope and for the calibration also signals of low amplitude had to be used.

Out of the total of 50 AcouADC boards produced, 30 were equipped with high-grade ADCs, with less inherent noise than the other 20 boards with normal grade ADCs<sup>1</sup>. Out of the first batch, 26 were calibrated for the usage in the AMADEUS stores. A selection of 18 boards was used to read out the signals of the 36 installed acoustic sensors. The rest of the boards showed defects, was reserved for spare usage, or was used for potentially destructive tests.

## 7.2 Input Stimuli

### 7.2.1 $\delta$ -Pulse

To calibrate the frequency response (in amplitude and phase) and the impulse response of the analogue part of the AcouADC boards, the approximation of a  $\delta$ -pulse by a waveform, gaussian in time was chosen. The input stimulus and the output signal of the amplifier/filter part measured by the oscilloscope are plotted in Fig. 7.2.

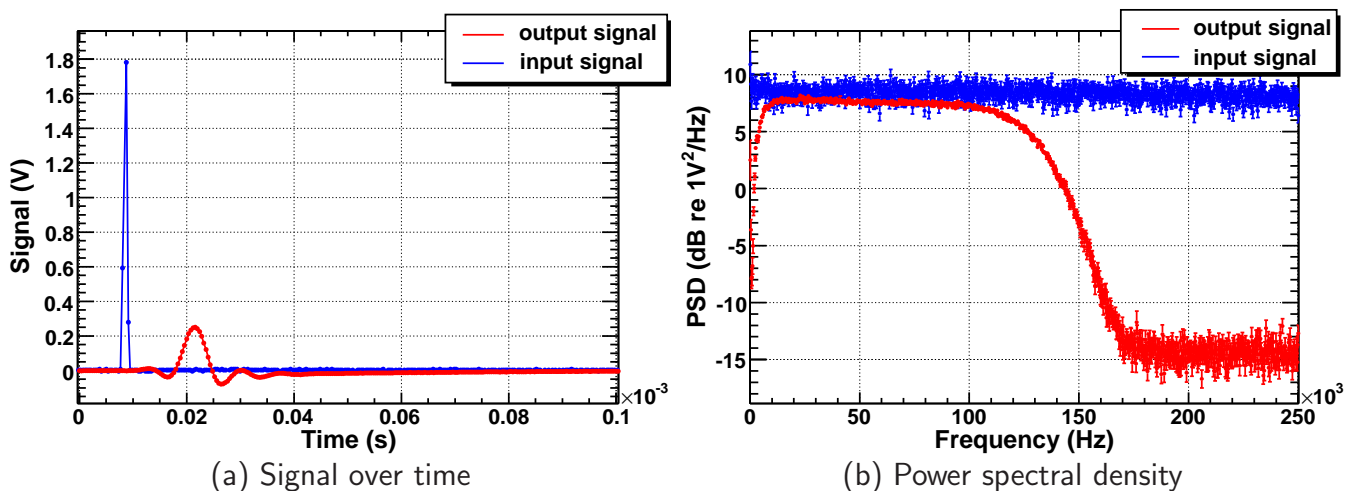


**Figure 7.2:** Exemplary input and output signal of the calibration with a  $\delta$ -pulse (a) and the spectral density of the signals (b). Shown are the oscilloscope measurements for board 0005, ch0 which were recorded and averaged over 100 pulses.

<sup>1</sup>The boards were numbered following the ANTARES scheme from 0001 to 0050.

The gaussian waveform had a  $\sigma$  in time of  $0.1 \mu\text{s}$ , the total signal was generated for  $20 \mu\text{s}$  or  $\pm 100\sigma$  and sent with a peak-to-peak amplitude of  $\approx 2V_{\text{pp}}$ . For the calibration of the boards down to  $10 \text{ Hz}$ , the signal was zero-padded (filled with zeros) up to a length of  $150 \text{ ms}$  and repeatedly sent to reduce statistical uncertainties. As the maximum sampling frequency is  $500 \text{ kSamples/s}$  or one sample every  $2 \mu\text{s}$ , this waveform is a good approximation of the delta-pulse with frequency components flat up to  $1 \text{ MHz}$ , i.e. beyond the range of the low-pass filter, as clearly visible in the shown spectrum. On the other hand, with the chosen parameters enough signal power was remaining in the frequency range of interest ( $\approx 1 - 250 \text{ kHz}$ ). From the analogue measurement of the signal at the input of the board and at the input of the ADC at the end of the analogue signal path, the impulse response of the filter/amplifier part can be estimated. The same can be done for the signal recorded by the DAQ by comparing the input stimulus with the triggered recorded waveform.

## 7.2.2 Gaussian White Noise

To calibrate the modulus of the frequency response, the actual gain of the different gain settings and the ADC transfer curve, gaussian distributed white noise, i.e. noise with a flat power spectrum and an amplitude histogram of gaussian form (cf. Fig. 7.3), was applied with different amplitudes.

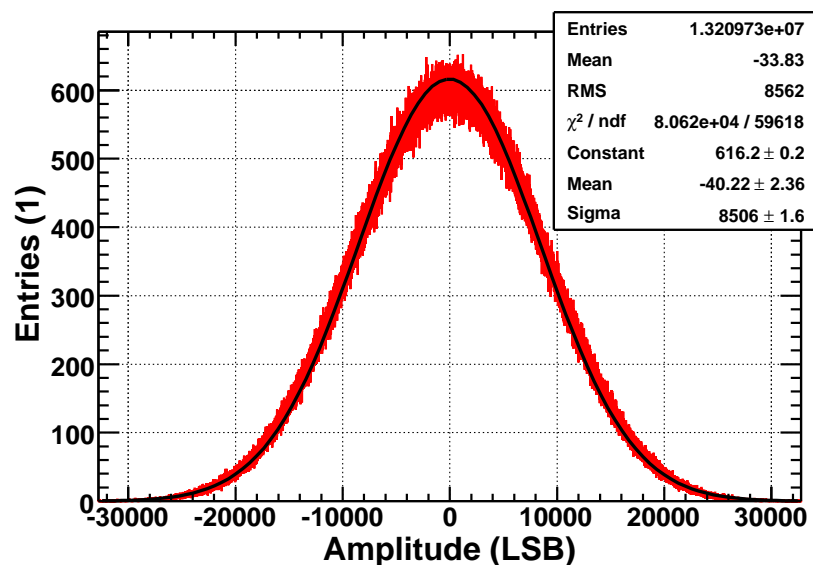


**Figure 7.3:** Amplitude histogram of a gaussian white noise as recorded with the AcouADC board 0005, ch0. The analogue measured standard deviation for this stimulus is  $(0.649 \pm 0.007) V_\sigma$  (input),  $(0.606 \pm 0.003) V_\sigma$  (output), the peak-to-peak amplitude is  $(5.1 \pm 0.1) V_{\text{pp}}$  (input) and  $(4.18 \pm 0.05) V_{\text{pp}}$  (output). The differences for mean and RMS/ $\sigma$  between the calculation for the histogram and the applied gaussian fit (solid black line) is effected by the non-linearities in the ADC which can be deconvoluted after the calibration.

One set of measurements was taken with over-modulated noise, i.e. with input amplitudes of  $\approx 5 V_{pp}$  including components which over-steer the filter/amplitude components and the ADC, especially when a gain setting of 100 was used. With this stimulus also the robustness of the system to high input signals was tested and no defects were found. The next set was taken with a noise of  $\approx 75 mV_{pp}$ , which almost saturates the ADC input range at the maximum gain of 562. With this set the system response can be tested for all gain settings with one input stimulus. The last set was an adapted noise setting with signal amplitudes of  $\approx 2.5 V_{pp}$  for gains 1.00 – 5.62,  $\approx 250 mV_{pp}$  for gains 10.00 – 56.2 and  $\approx 25 mV_{pp}$  for gains 100 – 562<sup>2</sup>. That setting was chosen to get a comparable ADC input level for each coarse gain step of 1.00, 10.0 and 100.

### 7.2.3 Sine Waveform

For the calibration of the ADC characteristics, especially to evaluate the non-linearities, a sine waveform was applied to the input of the board. The used waveform had a frequency of 26.87 kHz, which is incommensurable to the sampling frequency of 500 kSamples/s to avoid sampling effects and is within the passband of the analogue filter of the board. For the performed measurements with an ADC range R0 a peak-to-peak amplitude of  $\approx 4 V_{pp}$  was used, for range setting R1 (ADC range from  $-1$  to  $3 V$ ) the amplitudes were  $\approx 2 V_{pp}$ .

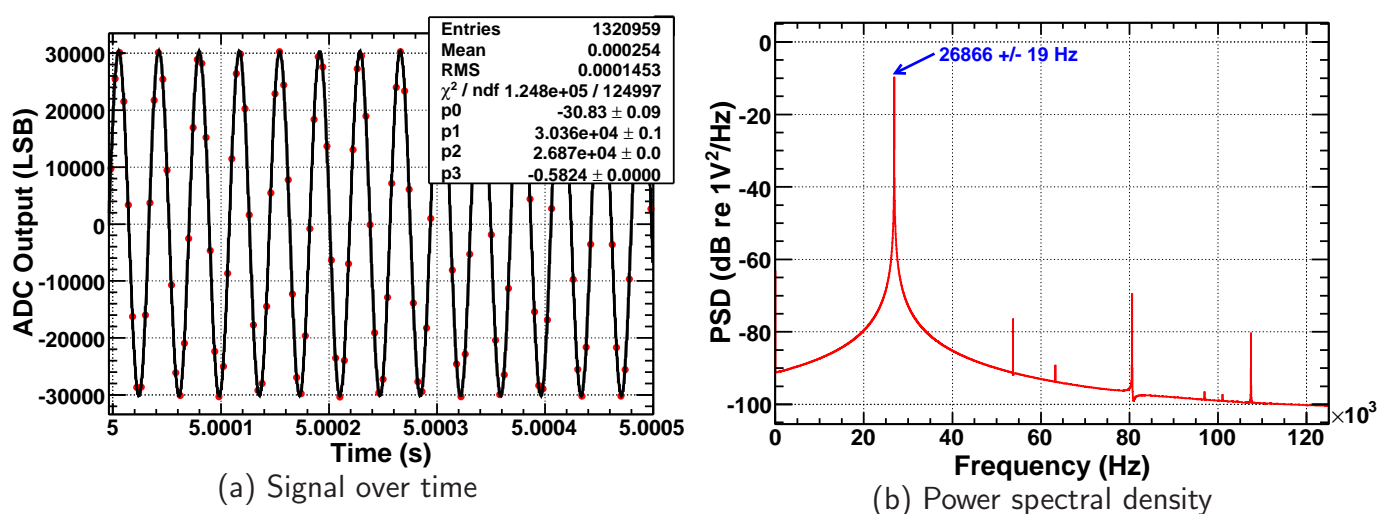


**Figure 7.4:** Signal of a sine waveform (a) recorded with board 0005, ch0. A function of the form  $s(t) = p_0 + p_1 \cdot \sin(p_2 \cdot t + p_3)$  fits the data (black solid line). The spectrum (b) of the same signal shows the prominent peak at the input frequency with highly suppressed noise peaks and harmonics.

<sup>2</sup>The peak-to-peak values given are the ones set in the waveform generator or calculated by the oscilloscope, respectively. For the analogue sampling used, the peak-to-peak value and the  $\sigma$  value are separated by a factor of 8.4.





# Chapter 8

## System Transfer Functions

In this chapter, the algorithms to deduce the system transfer functions from the calibration measurements are introduced and the results of the calculations are presented. The ADC transfer curve, the frequency response of the filters and the gain factors are derived based on the input stimuli and measurements described in the previous chapter.

The aim of the calibration was to get an accuracy in describing the AcouADC board characteristics at a level of  $< 10\%$  with a set of parametrised functions as simple as possible. This aim was reached with typical uncertainties being on a level of 1 to 2%. However, due to the complexity of the board and the variety of possible settings, this set is still extensive. The transfer functions describing the system are calculated for the whole signal path in the board instead of using separate ones for the analogue and digital part, as those parts affect each other and will always be operated together.

Since it is needed for the further calibration function, the ADC transfer curve is described first, followed by the frequency response of the system and the gain.

### 8.1 ADC Transfer Curve

The ADC transfer curve describes the conversion between the ADC output codes (in LSB) to the actual input voltage of the ADC (in V). This translation is represented by the derivation of the transition voltage levels for each output code. For an ideal ADC the curve is described by a linear function; for real ADCs non-linearities and electronics noise deform the curve. The algorithms used here to derive the curve assume that the ADC is non-invertingly monotonic, i.e. output codes are increasing with increasing input stimulus, and has no hysteresis, i.e. the transfer curve is not dependent on whether the input stimulus is raising or falling. It was confirmed that these conditions are met by the AcouADC board and its ADC.

For the calculation of the transfer curve the sinusoidal waveform was chosen as input signal to the channel of the AcouADC board under calibration. As a consistency check the same calculations were performed with the gaussian white noise stimulus. However, due to the bandpass in the system which suppresses the high and low frequency components of the noise, this signal does not stimulate the full input range of the ADC without over-steering the filters

and amplifiers and thus generating non-linear effects outside the ADC.

The algorithms used for the calculation follow the procedures described in [88–90] based on the international standard for the calibration of ADCs [91]. The disadvantage of using a sine as stimulus is that ADCs typically have frequency dependent transfer curves. However the signal amplitude distribution is favourable for a sine waveform as compared to gaussian noise, i.e. a smaller amount of recorded data is needed to calculate the ADC characteristics to the desired accuracy.

The ADC characteristics are calculated using a histogram method, in which a recorded histogram of signal amplitude is compared to the probability density of the input signal. The advantage of this method over directly fitting the signal is that it is also applicable to statistically distributed signals and faster to calculate for the required amount of data points ( $\approx 10^7$  samples per channel and setting). The probability density function  $p_d(V_s)$  of the stimulus signal  $V_s(t)$  with mean  $\mu$ , standard deviation  $\sigma$  and amplitude  $A^1$  is, respectively for the sine waveform (*sw*) and for the gaussian white noise (*gn*):

$$p_{d,sw}(V_s) = \frac{1}{\pi \sqrt{A_{sw}^2 - (V_s - \mu_{sw})^2}} \quad \text{and} \quad p_{d,gn}(V_s) = \frac{1}{\sqrt{2\pi} \sigma_{gn}} \exp\left(-\frac{(V_s - \mu_{gn})^2}{2\sigma_{gn}^2}\right). \quad (8.1)$$

The probability  $P_i$  for the input stimulus to lie between the transition voltage level  $T[i]$  of ADC output code  $i$  and  $T[i + 1]$  for output code  $(i + 1)$  is given by

$$P_i = \int_{T[i]}^{T[i+1]} p_d(V_s) dV_s. \quad (8.2)$$

Equation 8.2 can be solved for the transition levels using the probability densities of the applied signals from Eq. 8.1. The desired transition voltages  $T[i]$  can thus be calculated using the measured cumulative amplitude histogram  $H_c[i]$  of the recorded data, leading to

$$T_{sw}[i] = \mu_{sw} - A_{sw} \cos\left(\frac{\pi H_{c,sw}[i-1]}{S}\right) \quad (8.3)$$

and

$$T_{gn}[i] = \mu_{gn} \sqrt{2} \sigma_{gn} \operatorname{erf}^{-1}\left(2 \frac{H_{c,gn}[i-1]}{S} - 1\right), \quad (8.4)$$

where  $S$  is the total amount of samples taken.

The histograms of one measurement with sine waveform input are shown in Fig. 8.1. The probability density function, which is fitted to the amplitude histogram, describes the data well except for non-linearities in small separated code regions e.g. around 0,  $\pm 10\,000$  and  $\pm 19\,500$  LSB.

---

<sup>1</sup>These three parameters are measured at the calibration (cf. Sec. 7.1).

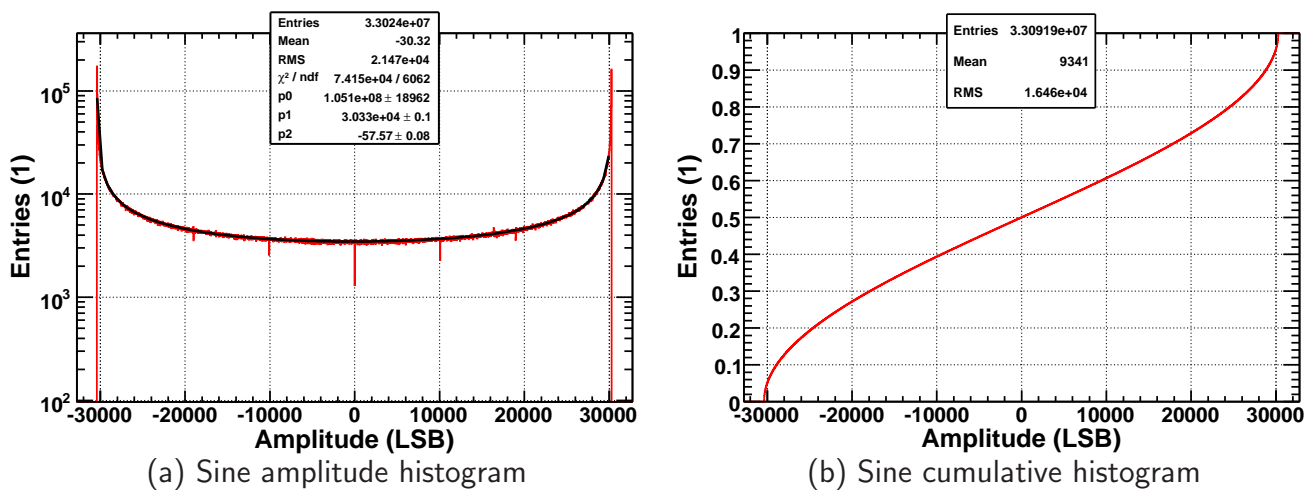


**Figure 8.1:** Histograms of a calibration measurement with sine waveform input: amplitude histogram (a) and cumulative histogram with maximum normalised to 1 (b). Measurements were taken with AcouADC board 0005, ch0. A fit is applied to the amplitude histogram (a) according to Eq. 8.1 ( $f(c) = p0/(\pi\sqrt{p1^2 - (c + p2)^2})$ , black line).

Figure 8.2 shows the average ADC transfer curve calculated from the transition voltage levels for each calibrated sensor channel.

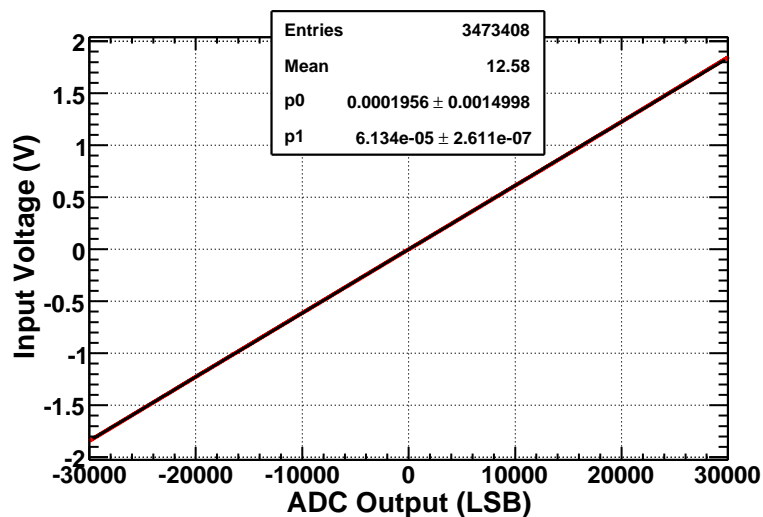


**Figure 8.2:** Total ADC transfer curve, averaged over all calibrated sensor channels. This curve displays the conversion from the ADC output code in LSB to the input voltage in Volts. A linear fit is applied to the curve, describing an ideal system response.

The applied linear fit shows the idealisation of a transfer curve with offset ( $p0$ ) and gain ( $p1$ ) correction only,  $V_{in} = p0 + p1 \cdot N_{LSB}$ . The values for an ideal ADC would be  $p0 = 0.000\text{ V}$  (no offset) and  $p1 = 4.000\text{ V}/2^{16} = 6.104 \cdot 10^{-5}\text{ V/LSB}$  (full-scale range (FSR) divided by the

number of output codes). As expected, those values do not deviate from the values found in the fit. As observable by the  $\chi^2/\text{ndf}$  of  $408 \cdot 10^6$ , the transfer curve is described well by a linear fit only globally, but not locally.

For quantification of the non-linearities which are responsible for those local deviations, the differential nonlinearity (*DNL*) and integral nonlinearity (*INL*) were calculated. The former represents the deviation of the actual code bin width ( $T[i+1] - T[i]$ ) from the ideal one ( $Q$ ), the later the cumulative deviation of the actual transfer curve from the ideal one:

$$\text{DNL}[i] = \frac{T[i+1] - T[i] - Q}{Q} \quad \text{and} \quad \text{INL}[i] = \sum_{k=0}^i \text{DNL}[k], \quad (8.5)$$

where  $Q = \text{FSR}/2^{16}$  is the full-scale range divided by the total number of codes. Histograms representing the INL and DNL averaged over all calibrated sensor channels are shown in Fig. 8.3.

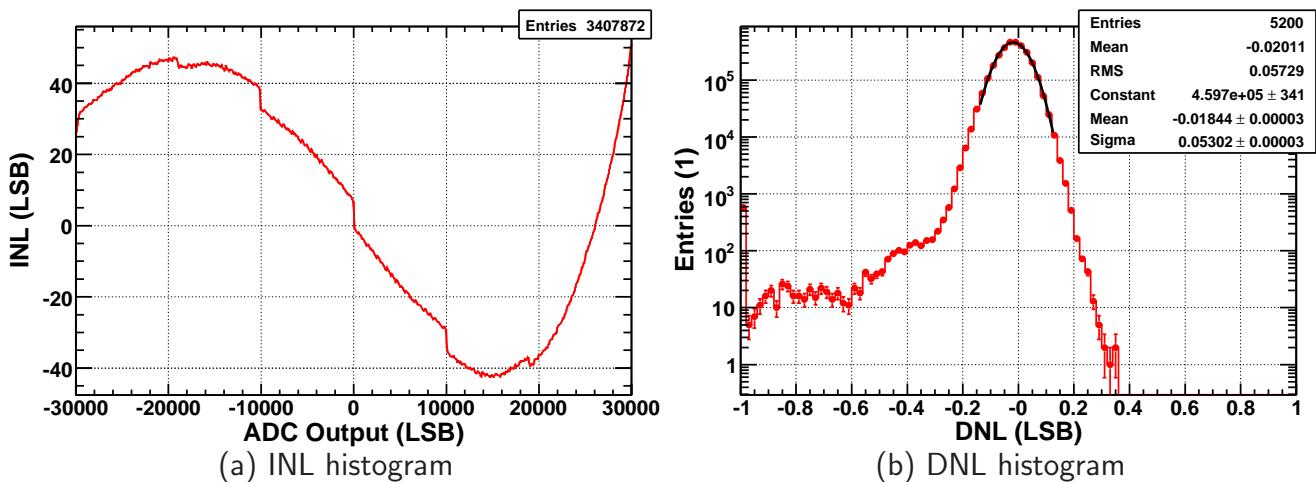


**Figure 8.3:** Average INL (a) and DNL histograms (b) for all calibrated sensor channels. The INL is shown as a function of the ADC output code, the DNL in form of a distribution histogram. A gaussian fit is applied to the central peak of the DNL distribution (black line), demonstrating the adequacy of the statistical uncertainty of the analysis as described in the text.

In the INL plot a deviation from the ideal curve is observable with a maximum INL below  $\pm 50$  LSB or  $\pm 3.1$  mV. Steeper drops around 0,  $\pm 10000$  and also, though less prominent, around  $\pm 19500$  LSB, show the regions of greater deviation visible in the amplitude histogram of the recorded data (cf. Fig. 8.1(a)). This feature was studied intensely and found to be originating from irreducible noise induced on the ground potential by the LCM surrounding.

On the whole, the deviation from the ideal code bin width is small. The standard deviation of the DNL distribution is 0.056 LSB or  $3.4 \mu\text{V}$  and the distribution exhibits a mostly gaussian form. For each calibrated sensor channel  $3.3 \cdot 10^7$  samples were analysed, sufficient for a tolerance of

0.053 LSB at a  $1\sigma$  confidence level according to the estimation in [88]<sup>2</sup>. This statistical error in the determination of the DNL is visualised by the gaussian fit in Fig. 8.3(b) with  $\sigma \approx 0.053$  LSB. The variation of the slope and the steep declines in the INL are represented by deviations from the gaussian form primarily at DNL values below  $-0.2$  LSB. Missing codes – i.e. ADC output codes which represent transition voltage intervals of zero width – were not observed in the calibration. The histogram entries in Fig. 8.3(b) below  $-0.9$  LSB, which would usually hint at missing codes, are from the empty bins or those only filled with noise due to the not fully saturated sine waveform.

As shown, the analysis of the ADC transfer curve of the system exhibits minor deviations from an ideal one. When the ideal transfer curve is applied to calibrate the data, the maximum systematic uncertainty induced by the non-linearities is below 0.1%. Also the differences between the ADC transfer curves of the individual channels are small: the standard deviation of the curves is  $1.6\mu\text{V}$  at output code 0 LSB and  $3.0\text{mV}$  at output codes  $-30000$  and  $30000$  LSB. Thus the average transfer curve shown in Fig. 8.2 can be applied for all channels or – for simplicity and processing time conservation – the ideal transfer curve can be used to determine the input voltages of the ADC. However, the shape of the amplitude histogram of the deep-sea ambient noise is systematically deformed by the non-linearities, which can only be deconvoluted by applying the full ADC transfer curve.

## 8.2 Frequency Response of the Filter

The transfer function of the analogue part describes the answer  $g(t)$  of the system to the input signal  $f(t)$ . For its determination it is assumed that the AcouADC is a linear time-invariant system. Those systems can be described by linear differential equations with constant coefficients [92]:

$$\left( \sum_{k=0}^n A_k \frac{d^k}{dt^k} \right) g(t) = \left( \sum_{l=0}^m B_l \frac{d^l}{dt^l} \right) f(t). \quad (8.6)$$

The Fourier transformation to the frequency domain, utilising  $df(t)/dt \rightarrow i\omega F(i\omega)$ , yields

$$\left( \sum_{k=0}^n A'_k (i\omega)^k \right) G(i\omega) = \left( \sum_{l=0}^m B'_l (i\omega)^l \right) F(i\omega). \quad (8.7)$$

Note that for the time-limited signals recorded with the ANTARES DAQ software in form of events, the existence of the Fourier integral  $F(i\omega) = \int_{-\infty}^{+\infty} f(t) \exp(-i\omega t) dt$  can be guaranteed by the usage of an appropriate window function.

The resulting rational complex valued transfer function  $H(i\omega)$  is given by

$$H(i\omega) = \frac{G(i\omega)}{F(i\omega)} = \frac{\sum_{l=0}^m B'_l (i\omega)^l}{\sum_{k=0}^n A'_k (i\omega)^k}. \quad (8.8)$$

<sup>2</sup>Equation A15 in this reference has to be modified for the used non-saturating sine waveform by a factor of  $2A/FSR = 0.91$ .

The transfer function of the filter part of the AcouADC board was evaluated by analysing the analogue and digital measurements performed during the calibration of the boards. A physical model of rational functions was fitted to the frequency response. Due to the small deviations between the characteristics of the individual boards, the same parameters were chosen for all the boards, only allowing for individual gain and noise characteristics. The latter vary for the different channels mainly due to the environmental noise in the laboratory that changed during the calibration.

The aim of the parametrisation was an accurate description with physical motivation when possible. For some of the filters a physical model would be complicated to implement in the calibration of the data and too time consuming during the conversion of the raw data. For those filters, simplified functions were found which fit the frequency response well.

A modulus-phase representation for the complex-valued filter transfer function  $H(f)$ , with  $f = \omega/2\pi$ , was chosen in the form

$$H(f) = A(f) \cdot \exp(i\Phi(f)), \quad (8.9)$$

with the real-valued functions for amplitude-frequency characteristic  $A(f)$  and phase-frequency characteristics  $\Phi(f)$ .

The characteristics are composed out of simple models for filters [93] and labelled by  $i$ ,  $j$  and  $k$ . For  $A(f)$  are used:

$$A(f) = G_{tot} \cdot \prod_i A_{h,i}(f) \cdot \prod_j A_{l1,j}(f) \cdot \prod_k A_{l2,k}(f) \quad (8.10)$$

with

$$A_{h,i}(f) = \left( \frac{f/f_{h,i}^0}{\sqrt{1 + (f/f_{h,i}^0)^2}} \right)^{n_{h,i}}, \quad (8.11)$$

$$A_{l1,j}(f) = \left( \frac{1}{\sqrt{1 + (f/f_{l1,j}^0)^2}} \right)^{n_{l1,j}}, \text{ and} \quad (8.12)$$

$$A_{l2,k}(f) = \frac{1}{\sqrt{1 + (f/f_{l2,k}^0)^{2n_{l2,k}}}}. \quad (8.13)$$

For  $\Phi(f)$  :

$$\Phi(f) = \phi_{tot} + \sum_i \Phi_{h,i}(f) + \sum_j \Phi_{l1,j}(f) + \sum_k \Phi_{l2,k}(f) \quad (8.14)$$

with

$$\Phi_{h,i}(f) = n_{h,i} \cdot \left( \frac{\pi}{2} - \arctan(f/f_{h,i}^0) \right), \quad (8.15)$$

$$\Phi_{l1,j}(f) = -n_{l1,j} \cdot \arctan(f/f_{l1,j}^0), \text{ and} \quad (8.16)$$

$$\Phi_{l2,k}(f) = d_{l2}^G \cdot 2\pi f. \quad (8.17)$$

The functions subscripted with  $h$  and  $l1$  model the LRC high- and low-passes<sup>3</sup> integrated on the AcouADC card, respectively. For those filters the corner frequencies  $f^0$  and the order  $n$  were calculated from the values of the actual composition of the filter elements. The functions subscripted with  $l2$  describe generalised low-pass filter and are used to model the root-raised cosine (RRC) low-pass filter. This filter exhibits an almost linear phase which was approximated by the group delay ( $d_{l2}^g$ ) given in [94] to be around  $12\ \mu\text{s}$  with small deviations at frequencies above  $100\ \text{kHz}$ . A best fit to the data yielded a delay of  $(12.39 \pm 0.28)\ \mu\text{s}$  and the deviations were fitted by a gaussian function. The total phase offset  $\phi_{tot}$  was found to be  $(-0.02 \pm 0.15)\ \text{rad}$ , compatible with no additional total phase delay.

Additional low-passes, also with the generalised form  $A_{l2}$ , were used to model the FIR filters realized in the FPGA [95] which are responsible for the downsampling of the digitised data. Those digital FIR filters use the same filter core for all boards and have a frequency-independent group delay, i.e. no additional relative phase between the data from different sensors is introduced and the phase of those filters have not to be corrected. The total delay of the FIR filters is dependent on the downsampling setting: for DS1 no delay is induced, for DS2 and DS4 the delay corresponds to 64 samples of the raw data, i.e.  $128\ \mu\text{s}$ . All parameters of the functions subscripted  $l2$  for RRC and FIR filters were adjusted for best fit to the data.

The results for all determined parameters are presented in Tab. 8.1. The calculation of the total gain  $G_{tot}$  will be described in Sec. 8.3.

Subscript	Pass Type	Corner Frequency $f^0$ (kHz)	Order $n$
h,1	RC, high	1.129	1
h,2	RC, high	1.881	2
h,3	RC, high	0.03183	1
l1,1	LRC, low	1022	3
l2,1	RRC, low	128.0	5.000
l2,2	RRC, low	150.0	10.00
l2,3	RRC, low	178.1	18.45
l2,4	FIR, DS2	109.1	22.00
l2,5	FIR, DS2	112.8	38.44
l2,4	FIR, DS4	47.96	13.76
l2,5	FIR, DS4	54.03	24.38

$$\phi_{tot} = (-0.02 \pm 0.15)\ \text{rad} \quad d_{l2}^g = (12.39 \pm 0.28)\ \mu\text{s}$$

**Table 8.1:** Parameters of the filter transfer-function described in Eq. 8.9 and the text.

Figure 8.4 visualises the frequency response of the system with a frequency binning of  $100\ \text{Hz}/\text{bin}$ .

<sup>3</sup>Passive or active filters with resistors, inductors and capacitors.

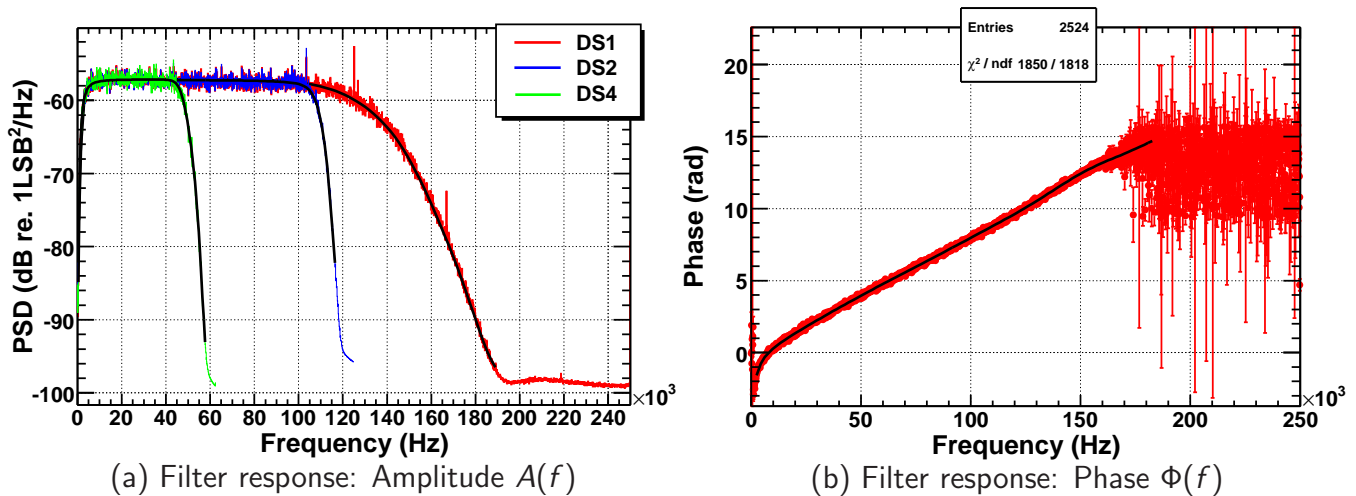


**Figure 8.4:** Filter response with transfer-function described in Eq. 8.9 with parameters from Tab. 8.1. The amplitude (a) is shown for DS1, DS2 and DS4 from a digital recording, the phase (b) from an oscilloscope measurement of the calibration of board 0005, ch0.

Two calibration measurements were used to fit this and all other filter transfer functions: a digital ADC recording of gaussian noise for the amplitude response and an oscilloscope recording for the phase – due to the complicated determination of exact timing of the external trigger to the AcouADC board. The amplitude response for the three different downsampling settings are plotted in Fig. 8.4: DS1 with frequencies up to 250 kHz, corresponding to the ADC sampling frequency of 500 kSamples/s, DS2 up to 125 kHz and DS4 up to 62.5 kHz. All samplings share the same high-pass feature but low-passes with different corner frequencies – the analogue RRC filter dominating for DS1 and digital FIR filters for DS2 and DS4. In the passband the filter response is uniform. Inherent noise contributes to the measurements significantly only in the stop bands, visible as a turn to the horizontal at high frequencies. The phase response of the analogue part is identical for all sampling settings. It exhibits a steep slope at low frequencies due to the high-pass filter. At higher frequencies, i.e. in the passband, the phase rises linearly with frequency. The RRC filter causes a slight deviation to this behaviour above  $\approx 120$  kHz and above  $\approx 160$  kHz noise starts to dominate the measurements, which is also true for frequencies below  $\approx 500$  Hz.

To estimate the accuracy of the chosen parametrisation, residuals of the fit to the recorded data for all calibrated channels were calculated with the total gain  $G_{tot}$  and the total phase  $\phi_{tot}$  as free parameters. Additionally a simple model for the inherent noise was fitted (a smoothed step function in the frequency domain) to estimate the limits of the applicability of the parametrised frequency response. The result is, that the presented filter transfer function is valid for the wide frequency ranges of 0.500 to 190 kHz (DS1), to 117 kHz (DS2) and to 58.0 kHz (DS4), respectively. The phase response is applicable for frequencies between 0.500 and 175 kHz. Outside the given limits, where the input signal as well as the electronics noise is already suppressed by at least 25 dB (factor of 18), the afore mentioned noise model, or a similar one,



has to be applied before calibrating the data with the given frequency response.

The results of the residual calculations are summarised in overview histograms in Fig. 8.5.

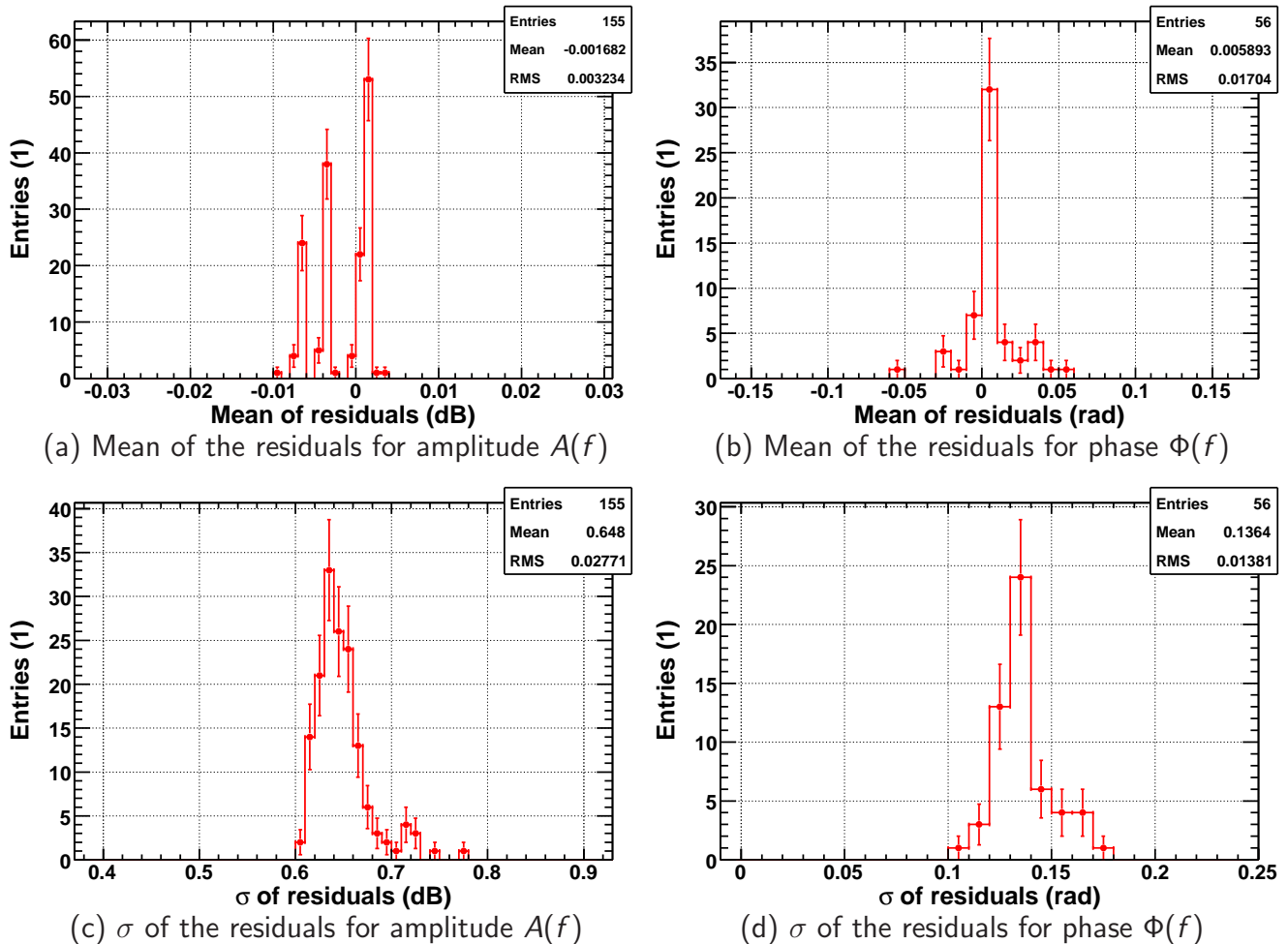


**Figure 8.5:** Residuals of the fit of the filter transfer function to the calibration data. For each channel and measurement a residual histogram was calculated and the mean (top row) and  $\sigma$  (bottom row) filled in the shown overview histograms. On the left hand side the parameters of residuals for the amplitude are shown, on the right hand side the results for the phase.

The amplitude and phase responses both have a mean residual compatible with 0, showing the adequacy of the filter model. The standard deviation of the residual for the amplitude is  $(0.648 \pm 0.028)$  dB which corresponds to an overall deviation of  $(7.7 \pm 0.3)\%$  and thus well within the target value. The phase response exhibits a  $\sigma$  of  $(0.136 \pm 0.014)$  rad.

### 8.3 Gain Settings

As the ADC transfer curve was calculated using the sine waveform as input stimulus, the gain calculation ( $G_{tot}$  in Eq. 8.10), presented here, is based on this measurement as well. The sine waveform calibration measurement was conducted at a gain setting of 1.00 (G1), so the gain for this setting was calculated absolutely for each board and channel - via the amplitude ( $A_{sw}$ ) and standard deviation ( $\sigma_{sw}$ ) of the waveform at the board input ( $in$ ) and directly at the ADC input ( $ADC$ ) following

$$G_{tot,1.00} = A_{sw,ADC} / A_{sw,in} \text{ and } G_{tot,1.00} = \sigma_{sw,ADC} / \sigma_{sw,in} , \quad (8.18)$$

respectively. The resulting gains for all channels are presented in Fig. 8.6, yielding a mean value of  $\overline{G_{tot,1.00}} = 0.951 \pm 0.011$  with maximum deviations below 2%.

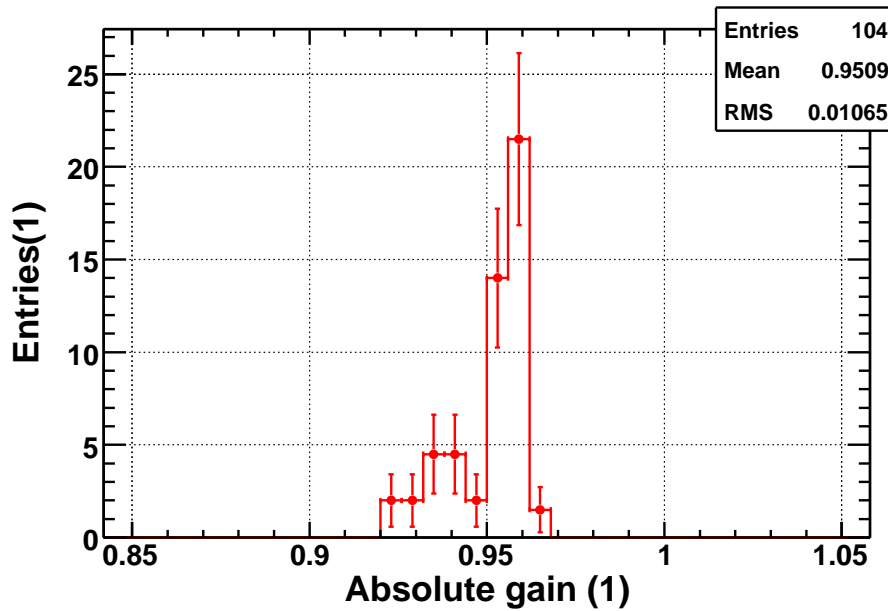


**Figure 8.6:** Distribution of the absolute gain at a nominal gain of 1.00 for all calibrated sensor channels, calculated from oscilloscope measurements of the sine waveform signal.

The values for the other eleven gain settings for each channel were calculated relative to the gain setting 1.00. For the relative gain calculation the recorded ADC data (digital recording,  $dig$ ) of the low noise and adapted noise input stimuli were considered. The relative gain is calculated following the equation

$$G_{rel,i}^{dig} = \sigma_{gn,i}^{dig} / \left( \sigma_{gn,1.00}^{dig} \cdot C_{corr} \right) , \quad (8.19)$$

where  $\sigma_{gn,i}^{dig}$  is the standard deviation of the gaussian white noise from the recording of setting  $i$ ,  $\sigma_{gn,1.00}^{dig}$  is the corresponding recording with gain 1.00 and  $C_{corr} = \sigma_{gn,in,i}^{ana} / \sigma_{gn,in,1.00}^{ana}$  is a correction

factor for variations in the input waveform determined from analogue (*ana*) measurements. To get the absolute gain for each setting the result of Eq. 8.19 has to be multiplied by  $\overline{G_{tot,1.00}}$ . As a cross-check, the gain was calculated absolutely according to Eq. 8.18, but from analogue measurements of gaussian noise, following

$$G_{tot,i}^{ana} = \sigma_{ADC,i}^{ana} \cdot C_{sup} / \sigma_{in,i}^{ana}. \quad (8.20)$$

Here, the frequency response of the system has to be taken into account, when comparing the signal standard deviation of gaussian white noise at the input of the board to the one at the input of the ADC. A suppression factor for the standard deviation of  $C_{sup} = 9.33 \pm 0.10$  was calculated from integrating the amplitude frequency response up to the sampling frequency of the oscilloscope of 1.25 MSamples/s at a nominal gain of 1 and comparing it to the integrated signal power spectrum.

The results averaged over all channels for each setting separately for both the digital and analogue measurements are plotted in Fig. 8.7. The distributions of the measured gains, separately plotted for each gain setting, can be found in the Appendix A.

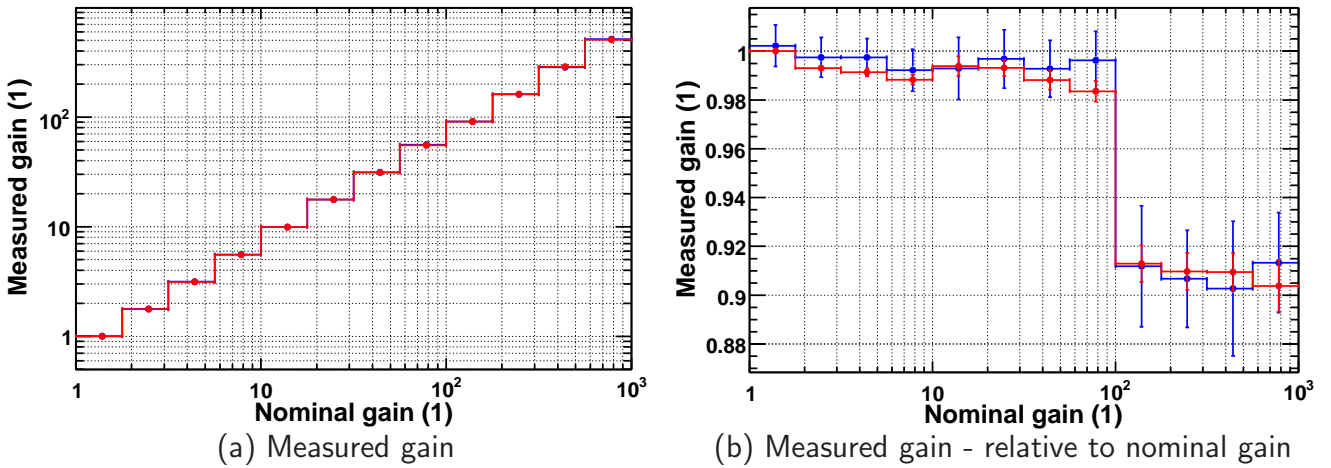


**Figure 8.7:** Gains averaged over all calibrated channels calculated according to Eq. 8.19 and Eq. 8.20. In (a) the measured gain is plotted over the nominal gain, in (b) the measured gain relative to the nominal gain is plotted over the nominal gain. Calculations using the recorded ADC data (digital) are shown in red and the ones using the analogue oscilloscope measurements are shown in blue.

The gains calculated from the recorded data and the oscilloscope data match well and show the same characteristic deviation from the nominal gain above a setting of 100, where the ratio drops by  $\approx 7\%$ . This behaviour can be explained by the implementation of the coarse gain settings 1.00, 10.0 and 100 in first amplifier stage of the AcouADC board, which depends on a switchable chain of resistors. The ratio of the resistor values defines the gain, i.e. a small systematic deviation of one of the resistors in the chain from its nominal value could describe the drop. A similar, but less prominent, step is expected at setting 10.0, but the uncertainties are too big to unambiguously identify it.

Again all channels on all boards can be described by one single gain value for each setting, the uncertainty being below 2%.

# Chapter 9

## System Characteristics

In this chapter the characteristics of the AcouADC board will be described with respect to its function to take data of acoustic sensors within the ANTARES detector. As the complex board is operated unaccessible in an even more complex system, internal and external influences on the data quality are evaluated.

An analysis of the dynamic range and frequency distortion of the board is presented first, followed by the inherent noise of the system and the crosstalk between channels. To test potential effects of the ANTARES data-acquisition hardware embedding the board on the data quality, the electromagnetic compatibility of the board has been evaluated.

The influence of all these effects on the data quality was found to be insignificant. Therefore the response of the AcouADC board to acoustic signals are evaluated is the end of this chapter, based on the system transfer functions derived in the previous chapter. The characteristics of the complete AMADEUS system, including the sensors, is presented in the following chapter (Chap. 10).

### 9.1 Dynamic Range and Frequency Distortion

At first the dynamic range and frequency distortion of the AcouADC boards was evaluated. One parameter used to study this characteristics is the *spurious free dynamic range* (SFDR) [96]. The SFDR is the ratio of the spectral amplitudes of the fundamental frequency of an input stimulus, typically a sinusoidal waveform, to the largest harmonic or spurious signal component and is usually expressed in dB. This quantity indicates the dynamic range of the ADC; any component in a spectral analysis which deviates more than the SFDR from the maximum component has to be treated carefully as it may be of inherent noise origin. The SFDR of an ADC is a function of the input signal amplitude and frequency, for the specific device used here [97] the optimal SFDR is  $\approx 96$  dB up to a frequency of 30 kHz. It degrades down to  $\approx 80$  dB up to the maximum Nyquist frequency of 250 kHz (manufacturer's data).

The SFDR for the AcouADC board was calculated from the recordings of the sine waveform calibration signal. A power spectrum of one of these measurements and an exemplary determination of the SFDR is shown in Fig. 9.1. The distributions of the calculated SFDR for all

channels is plotted in Fig. 9.2(a).

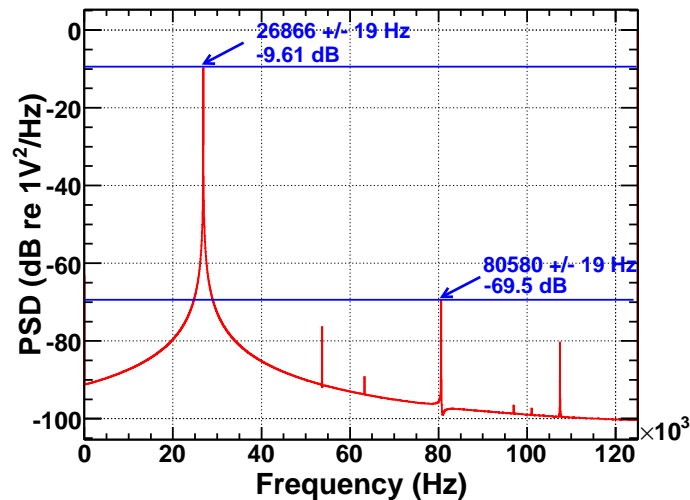


**Figure 9.1:** Power spectral density of the sine waveform used for the calibration of board 0005, ch0, averaged over 2500 time slices of 52,4 ms length. The fundamental frequency and the highest harmonic distortion is shown, giving a SFDR of  $\approx 60$  dB.

The measured average value of  $(59.9 \pm 1.1)$  dB is lower than the optimal one, due to the influence of the electric environment on the AcouADC board. However, spectral parts distorting the signal are still suppressed by a factor of  $\approx 1000$ . It was found that, as in the example shown, the highest non-fundamental peak in the spectrum is always the second harmonic of the input signal and not a noise peak. Thus it is safe to neglect distortions of the frequency spectrum of an input signal for both narrow-band and wide-band acoustic signals.

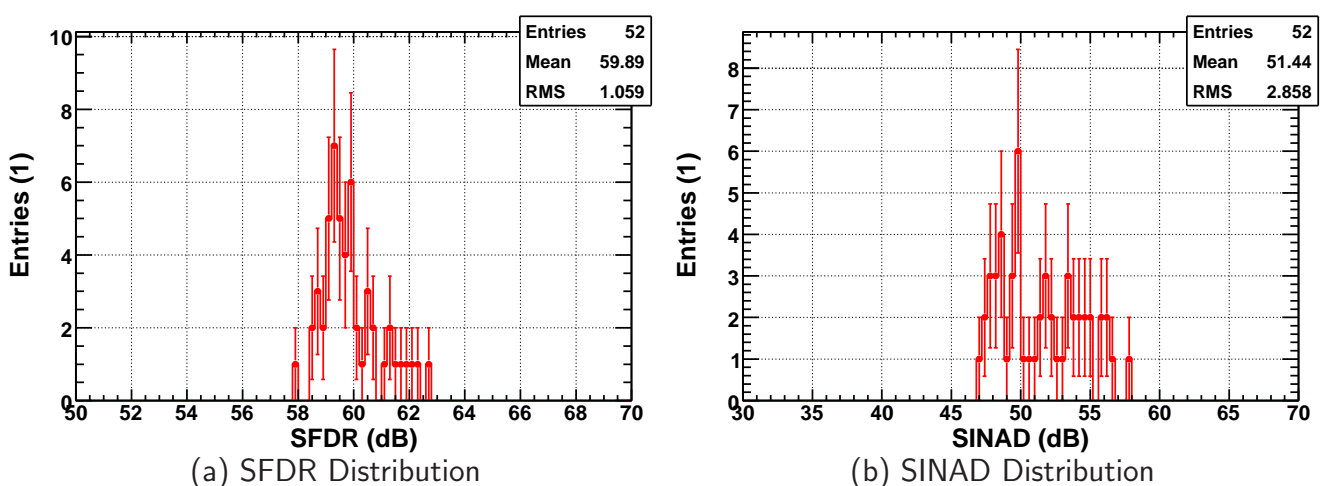


**Figure 9.2:** Distributions of SFDR (a) and SINAD (b) calculated as described in the text for all calibrated sensor channels.

The *signal-to-noise and distortion ratio* (*SINAD*) [96] is the ratio of the RMS of a signal to the one of the underlying total noise. The SINAD for the AcouADC board was evaluated using the same sinusoidal waveform as for the SFDR calculus above. The RMS of the signal was calculated directly from the recording. The RMS of the underlying noise was extracted from the residuals of a fit of a sine function to the recorded waveform (as performed in Sec. 9.4). Because of RMS calculus the SINAD value depends on the frequency of the applied waveform and its amplitude. As the amplitude of the sine waveform stimulus is almost full-range, the SINAD calculated here states an optimum for the devices under test. The optimum SINAD for the used ADC (manufacturer's data [97]) is 83 dB up to 30 kHz and degrading to 75 dB at 250 kHz. The mean measured SINAD (cf. Fig. 9.2(b)) of  $(51.4 \pm 2.9)$  dB is again below the optimum but still shows the high dynamic range of the system.

## 9.2 Inherent Noise and Channel Crosstalk

The inherent noise and crosstalk between sensor channels reduced the data quality in the AMADEUS-0 system. For this reason these characteristics were evaluated in detail for the AcouADC board (and for the whole AMADEUS system in Chap. 10). The analysis of the noise characteristics showed a highly improved behaviour as compared to the AMADEUS-0 DAQ system, so that those features are of low consequence to the data quality in AMADEUS.

Figure 9.3 shows an analysis of the noise levels for the calibration measurements with gaussian noise of low amplitudes and for comparison the inherent noise of a board without input signal. Always both channels of the board under calibration were analysed: the one where the signal was applied to (shown in red), and the one without external signal (shown in blue). The input stimulus is the same for each measurement and is comparable to the inherent noise of the hydrophones used in AMADEUS: the gaussian noise had a standard deviation of  $(1.020 \pm 0.025)$  mV<sub>σ</sub> as compared to  $(0.414 \pm 0.019)$  mV<sub>σ</sub> for the commercial hydrophones and  $(1.42 \pm 0.13)$  mV<sub>σ</sub> for the custom-designed ones (cf. Sec. 10.2). Therefore both the internal noise of a sensor channel and the crosstalk between channels can be evaluated from this measurement at conditions comparable to those in the operation of AMADEUS in the sea.

The observed values for the inherent noise are below the design goal of  $1 \mu\text{V}^2/\text{Hz}$  or  $\approx 0.5$  mV<sub>σ</sub> ( $\approx 8 \text{ LSB}_\sigma$ ) over the frequency range from 0 to 250 kHz and thus well below the intrinsic noise of the sensors (cf. Sec. 10.2). The inherent noise of the individual channels differs by up to  $3 \text{ LSB}_\sigma$ . The average value is below  $5 \text{ LSB}_\sigma$  for the coarse gain settings G1 (1.00), G10 (10.0) and G100 (100), which are implemented at the first amplifier stage. For the fine gain tuning in the second stage (factor 1.00, 1.78, 3.16 and 5.62), the inherent noise of the first amplifier stage is amplified, thus the noise reading at the ADC is expected to rise slightly more than linear with the fine gain setting (for a detailed analysis of the noise of operational amplifiers see e.g. [98]).

This behaviour is visible in the solid blue curve of Fig. 9.3(a) up to a nominal gain of 56.2. From G100 upwards the noise in the open channels increase compared to the same fine gain setting at lower coarse settings (1.00 and 10.0). This shows the crosstalk of the gaussian white noise from one channel of the board to the other, as compared to the stable behaviour of the

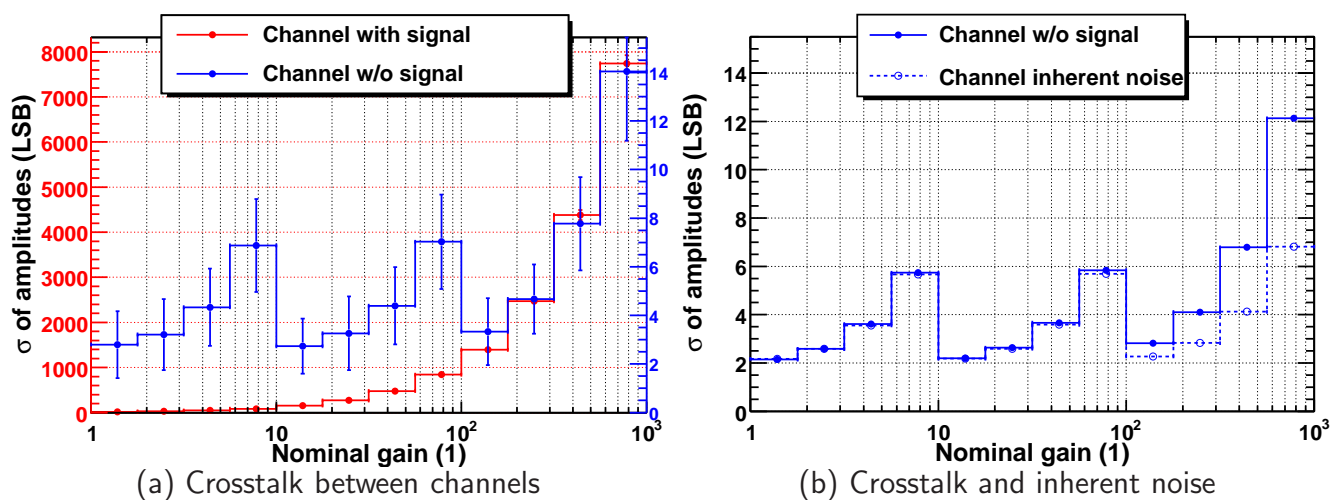


**Figure 9.3:** Standard deviation of the calibration recordings with Gaussian noise at different gain settings, averaged over all calibrated channels (a). In red the average standard deviation for the applied signal is shown, in blue the noise of the corresponding channel on the same board without signal is shown with a different scaling. The error bars indicate the deviations between the different channels. As an example the crosstalk to the channel without signal is shown in (b) for board 0005, ch0 as solid line and circles and for comparison the inherent noise of the same channel as dashed line and open circles.

exemplary shown inherent noise of board 0005, ch0 in Fig. 9.3(b). However, since this crosstalk is small, the inherent noise rises only roughly by a factor of two when comparing the same fine gain settings – at the same time the input signal rises by a factor of 10 or even 100. Note that even at a gain setting of 1.00 the input signal has already a standard deviation of  $\approx 15 \text{ LSB}_\sigma$ , higher than the inherent noise level even at G562, where the input signal has  $\approx 7800 \text{ LSB}_\sigma$ . As all sensors will be read out with the same settings at the same time and the input stimulus will be comparable, the crosstalk for Gaussian white noise between channels is negligible, as is the inherent noise.

The noise characteristics in the frequency domain are shown in Fig. 9.4 for the same measurements as above. For comparison the power spectra of a channel with low noise applied are shown for the standard gain of 10.0, and the spectra for the channel without signal for the exemplary gains G1, G100 and G562. The peak in the low frequency range at 3.5 kHz is assumed to originate in the non-standard power supply system used in the test. The curves for G1 and G100 show a comparable noise level – the curve of G10 not shown here as well –, G562 deviates, with an increasing component towards low frequencies originating in the crosstalk. The inherent noise for a gain of 100 is well below the recorded signal at the factor of 10 lower gain in the whole frequency range with the smallest distance of 10 dB for the highest and lowest frequency ranges in the stop band of the filter. Therefore the inherent noise of the system is at no spectral range higher or even in the same region as the input signal expected from the hydrophones.



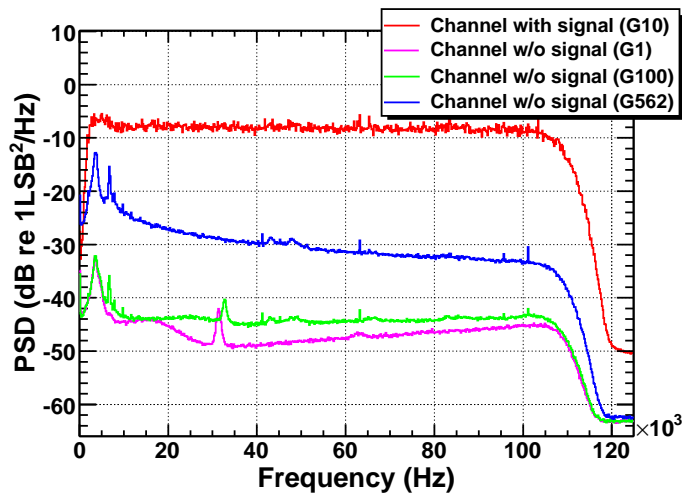


**Figure 9.4:** Spectrum of measurements for inherent noise and channel crosstalk for measurements on board 0005. The signal (red) was applied to ch0 and is shown for a gain setting of 10.0 (G10). The inherent noise and cross talk is demonstrated by spectra of the open channel without signal at gain settings 1.00 (G1, magenta), 100 (G100, green) and 562 (G562, blue).

The channel crosstalk for small-band input was checked with the sinusoidal input stimulus, which almost saturates the full-scale range of the ADC. As shown in the spectra in Fig. 9.5, crosstalk constitutes no problem here either, as only the fundamental frequency and first harmonic is observable in the channel without signal, but with a suppression of  $\approx 100$  and  $\approx 50$  dB, respectively.

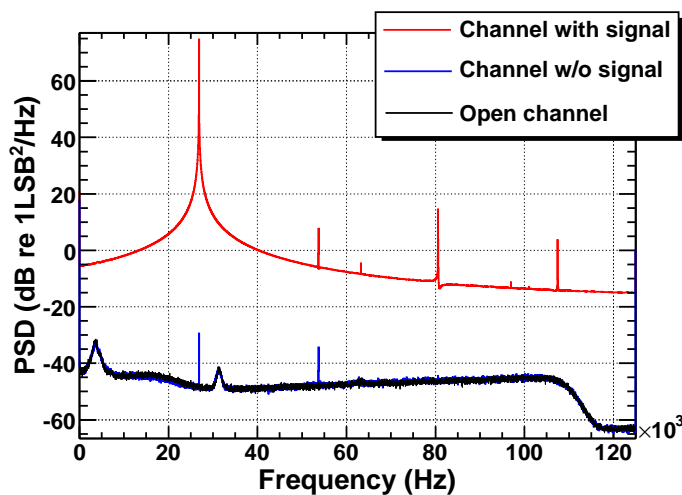


**Figure 9.5:** Power spectrum density for a recorded sine waveform with board 0005, the channel with the signal applied is shown in red, the one without signal in blue and overlaid in green an open channel without any input stimulus to the board.

### 9.3 Electromagnetic Compatibility

At different ANTARES integration sites, the system was tested extensively for its capability to operate in the electromagnetic environment of the ANTARES DAQ hardware without degradation of the data quality, i.e. its *electromagnetic compatibility* (EMC). However, as the ANTARES DAQ hardware characteristics cannot be fully emulated in the laboratory – even at those sites –, also the *electromagnetic vulnerability* (EMV) of the system was tested in a controlled environment<sup>1</sup>. The EMV is defined as “the characteristics of a system that cause it to suffer degradation in performance of, or inability to perform, its specified task as a result of electromagnetic interference” [100].

The system was tested for cable-propagated interference, induced by high-frequent (*HF*) fields of 40 kHz to 250 MHz (sine waves with a peak-to-peak amplitude of 10 V). As carrier wave a 1 kHz sine wave with an 80 % amplitude modulation was superimposed on the HF. The HF-current induced into the system has peak values up to 350 mA, almost reaching the power consumption of an AcouADC board and orders of magnitudes higher than any noise from the ANTARES DAQ hardware (typically in the mA range). The HF was induced to all DC power wires going from the LPB to the backplane, thus the disturbance was superposed to all supply voltages.

The test system, shown in Fig. 9.6, consisted of a fully equipped LCM with a simplified clock board, was powered over the LPB by 48.0 V and contained three prototype AcouADC boards. At one board (the first one visible in the photograph) the optional metal screen covering the first amplification stage (cf. Sec. 6.2) was present at one sensor channel and absent on the other, as on the channels of the other two boards. No failure in the data-taking was observed and no extreme events occurred under these extreme conditions. Nonetheless some improvements in the grounding scheme of the boards were triggered by the tests, e.g. the metal screen reduced the noise substantially and was thus part of the final design.

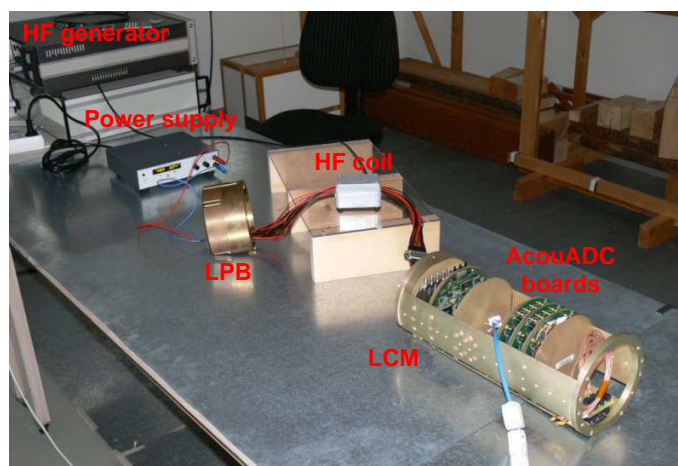


**Figure 9.6:** Photograph of the setup for the EMV tests described in the text.

<sup>1</sup>Following the DIN EN 61000-4-6 [99] norm at a certified EMV laboratory.

The standard deviations of signal amplitudes for a setting of gain 10 (G10), sampling at 250 kSamples/s (DS2) and full ADC input range (R0) – calculated in subsequent half-second intervals – are shown for a full sweep from 40 kHz to 250 MHz in Fig. 9.7. Note that the given frequencies may differ from the actual ones up to 10 %, as the data were recorded continuously during the whole sweep (which was done step-wise) and the assignment of the frequencies could only be done off-line. Deviations from the typical inherent noise of  $\approx 2 \text{ LSB}_\sigma$  are observable primarily in two frequency ranges: below 150 kHz and above 70 MHz. The first range marks the active region of the AcouADC board, the pass-band of the filters. HF induced noise in this range is found in the data unshifted in frequency and also unbroadened, i.e. as sharp spikes which can be easily eliminated in an analysis (cf. Fig. 9.8). The second range is situated, where the wavelength of the interferences matches the physical dimensions of the test system ( $\lambda = c/(\sqrt{\epsilon_r} \cdot f)$ , e.g.  $\lambda \approx 0.75 \text{ m}$  for  $f = 200 \text{ MHz}$  and a typical relative permittivity  $\epsilon_r \approx 4$  for printed circuit boards as the backplane of the LCM). Visible is the improvement by the shielding, especially in the active region below 150 kHz.

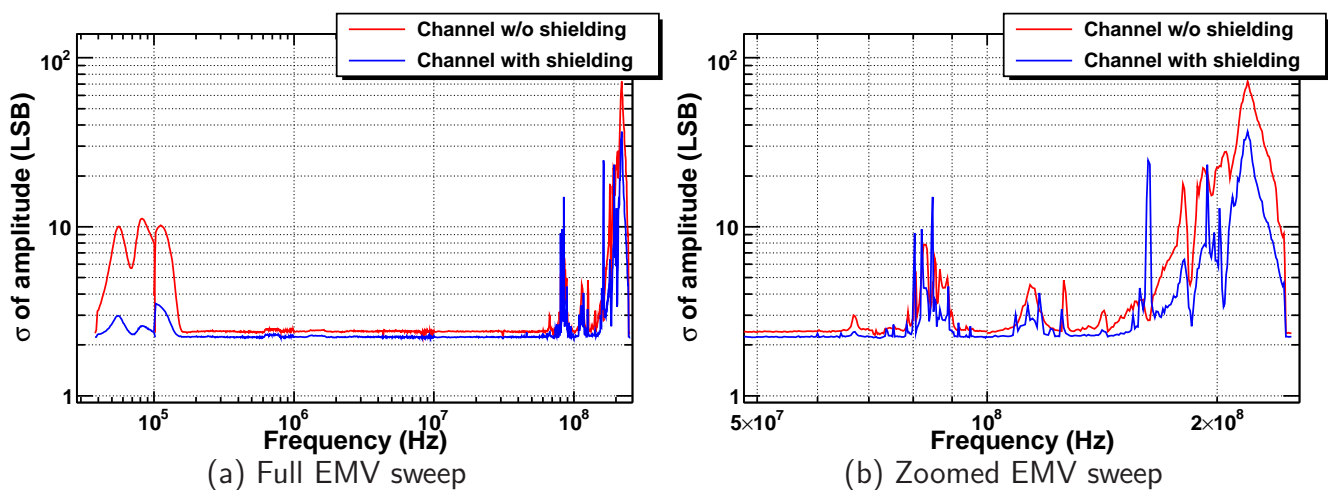


**Figure 9.7:** Induced noise by a HF field with frequencies ranging from 40 kHz to 250 MHz (a) and a zoom to frequencies exceeding 50 MHz (b).

During the tests a complex response of the noise levels recorded by the boards were found, e.g. a by the shielding of the board in the middle of the setup. However, the induced noise even for the extreme input interference ( $10 \text{ V}_{pp}$  interference voltage and  $350 \text{ mA}_{pp}$  parasitic current) used in the tests never exceeds  $40 \text{ LSB}_\sigma$  for the shielded channel. The system can thus be considered nearly undisturbed by noise induced by external electronics.

Figure 9.8 shows the spectra for interference around 56 kHz and 220 MHz, i.e. where the induced noise in the AcouADC board shows peaks. For the interference in the pass-band the frequency is reproduced in the recording, whereas at higher input frequencies the noise is distributed over the full frequency range of interest, with rising contributions toward lower frequencies.

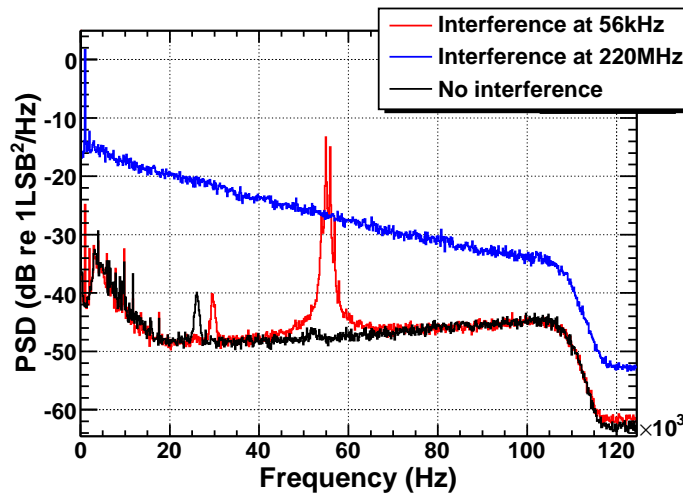


**Figure 9.8:** Recorded power spectra for regions with high induced noise calculated over 6 steps in interference frequency. For high frequency interference ( $\approx 220$  MHz) a broadband noise is induced, for low frequencies ( $\approx 56$  kHz) sharp spikes at the input frequencies of 55, 56, 57 and 58 kHz are observable. The carrier frequency is observable at 1 kHz.

## 9.4 System Stability

The long-term stability of the system was also analysed, as the system is designed to work continuously aside from short power cycles of the detector.

The tests were performed with the calibration setup (cf. Sec. 7.1), thus a synchronisation by the GPS clock was not available. However, even with the pseudo clock board used, the fit of a sine waveform generated by an arbitrary waveform generator shows the temporal coherent operation over a short period of 5.2s (cf. Fig. 9.9) with high precision, a prerequisite for the linearity and noise analysis. The fit reproduced the input frequency of 26.867153 kHz to a relative precision of  $3.2 \cdot 10^{-6}$  and no phase delay was observed for over 130 000 sine periods.

To evaluate the long-term stability, the setup was equipped with three AcouADC boards. The inherent noise of that setup was analysed over a period of  $6 \cdot 10^5$  s or 7 days at a setup of gain 100, downsampling 2 and full ADC range. The mean and standard deviation of the noise were calculated for subsequent 5.2s long time slices, the distribution of these parameters is shown in Fig. 9.10.

The distribution of the mean values (Fig. 9.10(a)) shows a slight evolution with time for the first channels on each board (ch0, ch2 and ch4 in the figure). The variance of those values range from 0.8 to 1.0 LSB whereas that of the other channels varies only from 0.2 to 0.3 LSB. As the mean of the distribution is caused by the difference between two reference voltages on the board, it can only be deduced that one of those exhibits a small temporal variation ( $1 \text{ LSB} \hat{=} 6 \cdot 10^{-5} \text{ V}$ ). This behaviour could be caused by a temperature gradient between the left and right side of the board, due to the cooling of the LCM by a fan from the side, where the second channel is located and is of no direct consequence to data-taking with AMADEUS. The

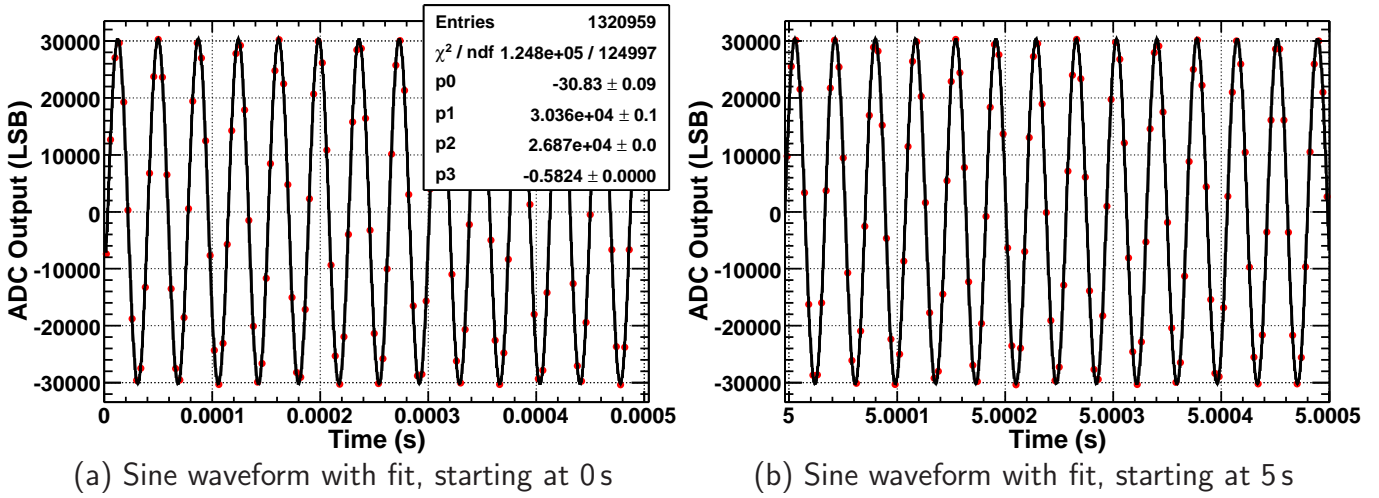


**Figure 9.9:** Typical recorded sine waveform (red points) with board 0005, ch0, with sine fit applied ( $f(t) = p_0 + p_1 \cdot \sin(p_2/2\pi \cdot t + p_3)$ , black solid line). The total length of the waveform is 5.2 s, the fit was made for the first 0.50 s. The waveform and fit are shown for two 0.50 ms time intervals starting at 0.0 s (a) and 5.0 s (b).

distribution of the standard deviation (Fig. 9.10(b)) is of more relevance to the measurement of ambient noise in the sea. It exhibits a strictly statistical fluctuation with low variances of 0.2 LSB and slightly different inherent noise of the individual channels between 2.2 to 2.7 LSB, demonstrating again the low inherent noise of the AcouADC board. With deviations at such a small level, the system can be operated stably with high precision over long periods.

## 9.5 System Response to Acoustic Signals

As has been shown, neither internal nor external sources create a significant deviation of the signal quality and system performance. Therefore the response of the AcouADC board to signals can be described with the system transfer functions derived in the previous chapter. The calculation results can be compared to recorded signals; an agreement between both shows the validity of the calibration of the boards. In the following this test of the board calibration is presented. As input signals, signatures interesting with respect to acoustic detection of neutrinos were chosen: bipolar signals and gaussian white noise.

### 9.5.1 Bipolar Pulse Input

A form suggested in [34] was chosen to represent a bipolar pulse:

$$S(t) = -A \cdot \frac{t - t_0}{\tau} \cdot \exp\left(-\frac{(t - t_0)^2}{2\tau^2}\right). \quad (9.1)$$

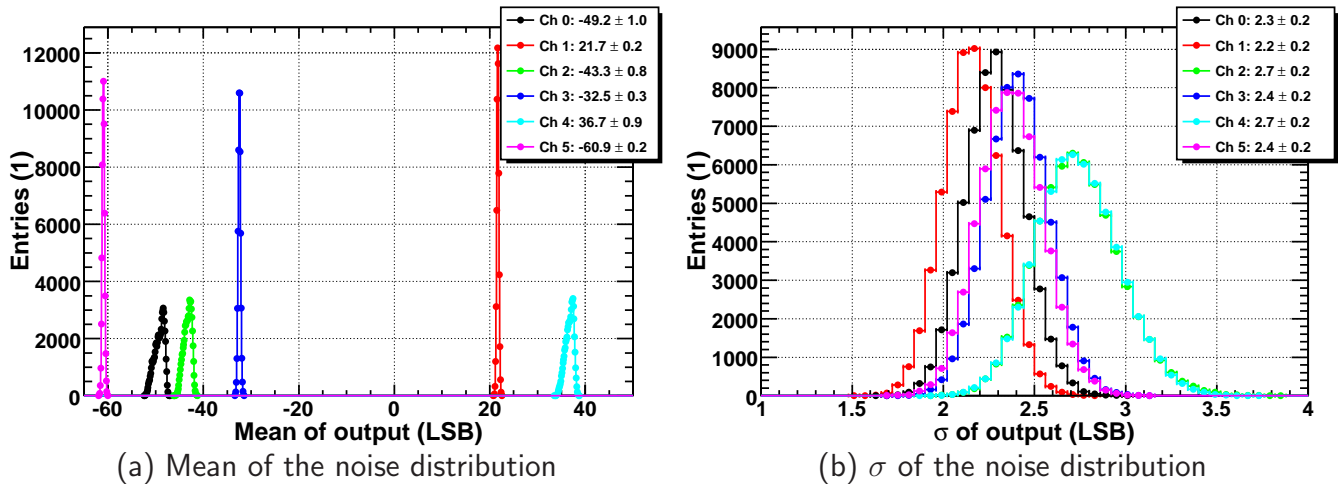


**Figure 9.10:** Distributions of the mean (a) and  $\sigma$  (b) for a recording of the inherent noise amplitudes over 7 days as described in the text. Ch0 to ch5 denote the six channels of three AcouADC boards in one LCM used in the measurement.

The amplitude  $A$  was chosen such that the signal applied to the board input had a peak-to-peak value of 100 mV,  $t_0$  was set to 0.5 ms and  $\tau$  to 7  $\mu$ s, corresponding to a peak-to-peak distance of 14  $\mu$ s. This parametrises the acoustic signal of a UHE cascade as shown in Fig. 4.1 in Sec. 4.1 to a good degree.

The recorded signal in a time interval of 0.1s is in good agreement with the expected, when applying the filter transfer function to the input signal, as shown in Fig. 9.11.

The small discrepancies, especially at the induced second positive pulse, are exclusively in the low and high frequency ranges (below 3 kHz and above 80 kHz), where the spectral power of the pulse sent did not overcome the electronics noise of the surrounding. This is visible in the power spectrum plot as well as the phase plot, where the green measured curve deviates from the blue calculated one for those frequency ranges. However, not much of the total signal energy falls into that frequency ranges and thus only a small fraction of the signal information is lost. The signal to noise ratio in the frequency domain can be improved by choosing a shorter time interval for the calculation of the system response, the one chosen was used to match the length of a time slice in the ANTARES data format of 0.105s.

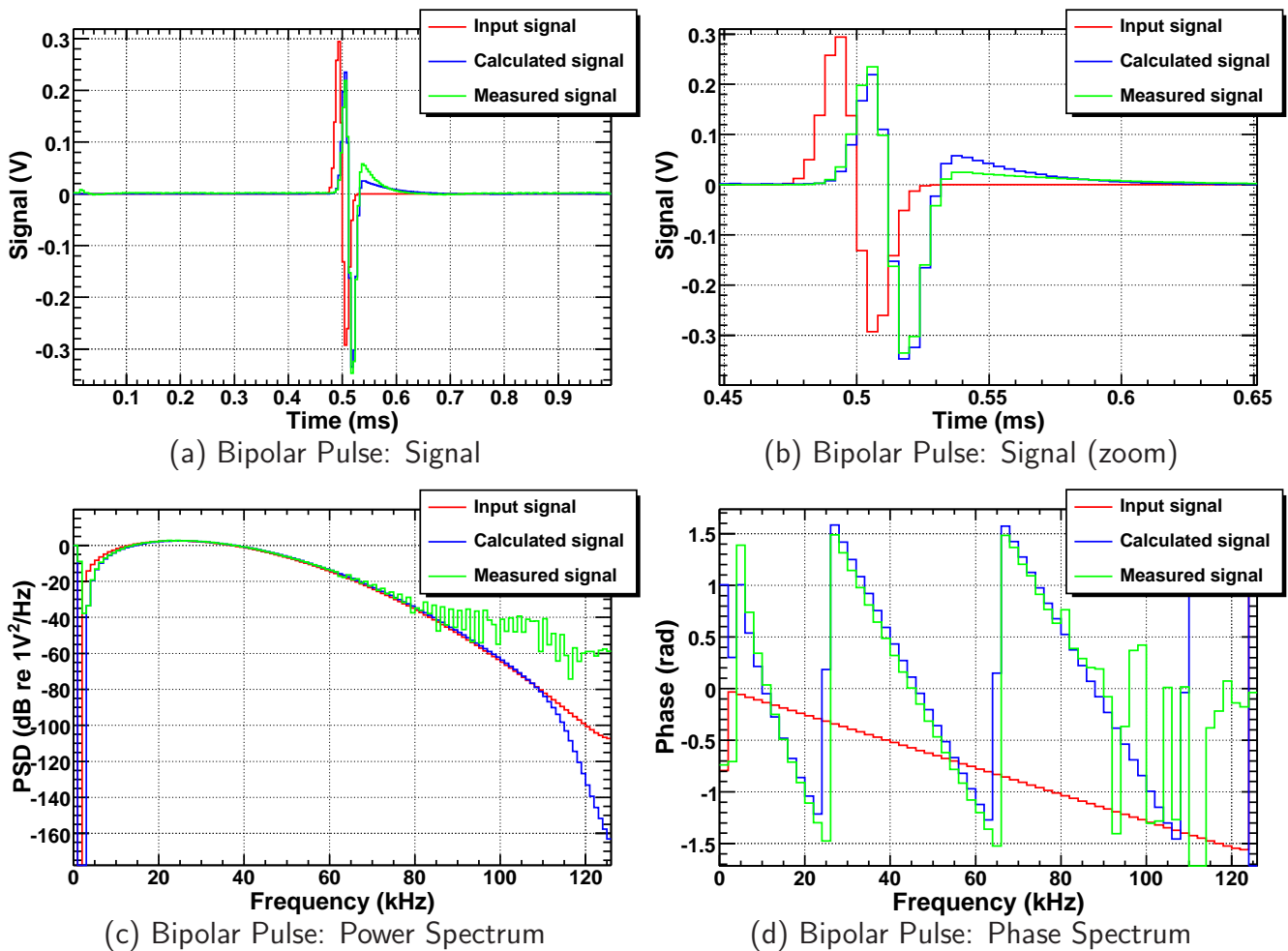


**Figure 9.11:** System response to a bipolar pulse as expected in a neutrino interaction recorded for 0.1s at 250 kSamples/s. The time domain response is shown for the whole period in (a) and a zoom in (b). The response in the frequency domain is represented by the power spectrum density in (c) and phase in (d). For better visibility the phase plots were smoothed, the one for the calculated signal was plotted modulo  $2\pi$ .

### 9.5.2 Gaussian Noise Input

For the representation of the analysis of the system response to gaussian white noise, amplitude histograms and the power spectra are used. Exemplary data of a 16.0s long time interval is presented in Fig. 9.12 for measurements of gaussian noise with low amplitude at a setup of gain 100, downsampling 2 and full ADC range. For comparability the ADC input values have been determined once with an ideal ADC curve of  $6.104 \cdot 10^{-5}$  V/LSB and no frequency response of the amplifier/filter part, and once with the full derived response of the board (cf. Sec. 8.1). The amplitude distributions (Fig. 9.12(a)) for those two forms of data representation do not differ much, as expected. However, the significance of the gaussian fit improves with the full calibration. The frequency response of the AcouADC board only effects regions of the spectrum

(Fig. 9.12(b)), where the high- and low-pass starts to suppress the input signal. Those regions are reproduced adequately after calibration of the data. In the stop-band, where the transfer function is not valid (for downsampling 2:  $< 500$  Hz and  $> 117$  kHz), the impact of the inherent noise is clearly identifiable by a rising of the spectral power for the calibrated data.

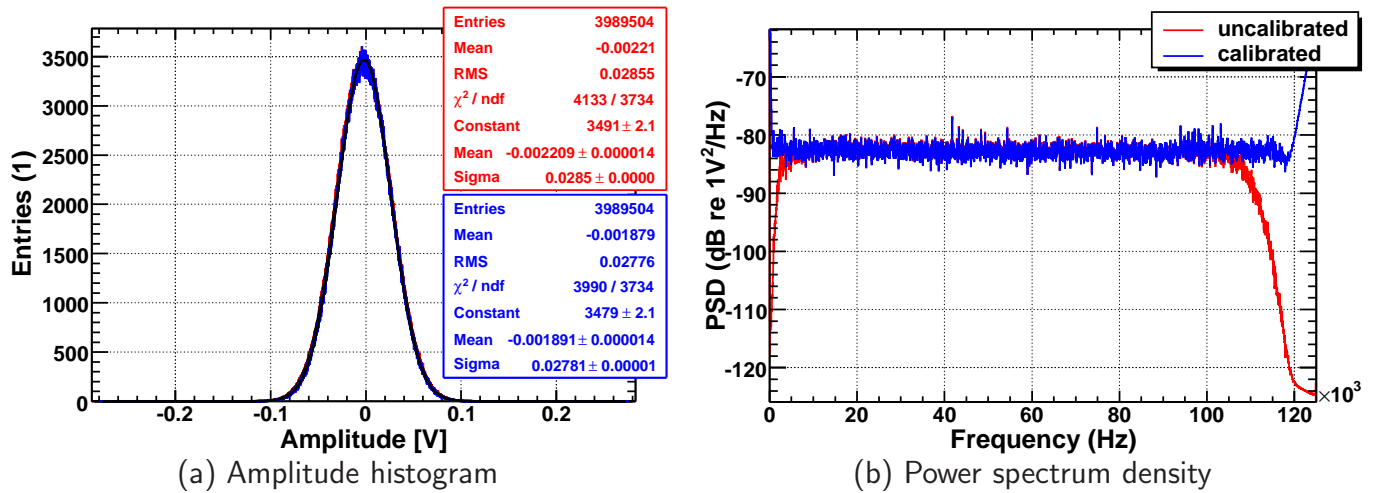


**Figure 9.12:** System response to gaussian white noise input. Amplitude histogram (a) and power spectral density (b) are shown using an ideal ADC response and no frequency response of the filter (red, uncalibrated), and using the full system calibration (blue, calibrated).



## **Part IV**

# **Data Taking with the AMADEUS System**



# Chapter 10

## System Characteristics and Performance in the Laboratory

In the previous chapters the AcouADC board as integral part of the off-shore DAQ system of AMADEUS was presented and its characteristics were illustrated. The board was found to be well describable by parametrised system transfer functions with no significant deviations in performance due to inherent noise, system instabilities, etc.

In the following chapter the performance and characteristics of the complete AMADEUS system, including the acoustic sensors, will be described. Most features will be illustrated using one commercial and one custom-designed hydrophone, whose overall sensitivity was shown in Fig. 6.3 (labelled LTI105 and HTI010, respective). Where not indicated differently, the voltages given in the rest of this work are the output voltages of the sensors, i.e. the reconstructed input voltages of the AcouADC board, calculated from the recordings using the ideal ADC transfer function, the full filter response and the average gain factors as presented in Chap. 8.

### 10.1 System Stability

In Sec. 9.4 the long-term stability of the AcouADC board was demonstrated, with variations of the noise data distributions  $\leq 1 \text{ LSB}_\sigma$  in the mean and  $\leq 0.2 \text{ LSB}_\sigma$  in the standard deviation. The long term stability of the AMADEUS system including sensors was tested in the same setup, using six commercial hydrophones selected for the equipment of one acoustic storey on detection line L12. Due to the size of the setup, which consisted of the hardware for one complete storey, it could not be completely shielded from outside influences, like HF-noise and ambient acoustic noise. The system noise was again analysed over a period of  $6 \cdot 10^5 \text{ s}$  (7 days) for a setting of gain 100, downsampling 2 and full ADC range. The mean and standard deviation of the noise were calculated every 10s with a time slice length of 5.2s. The distribution of these parameters is shown in Fig. 10.1.

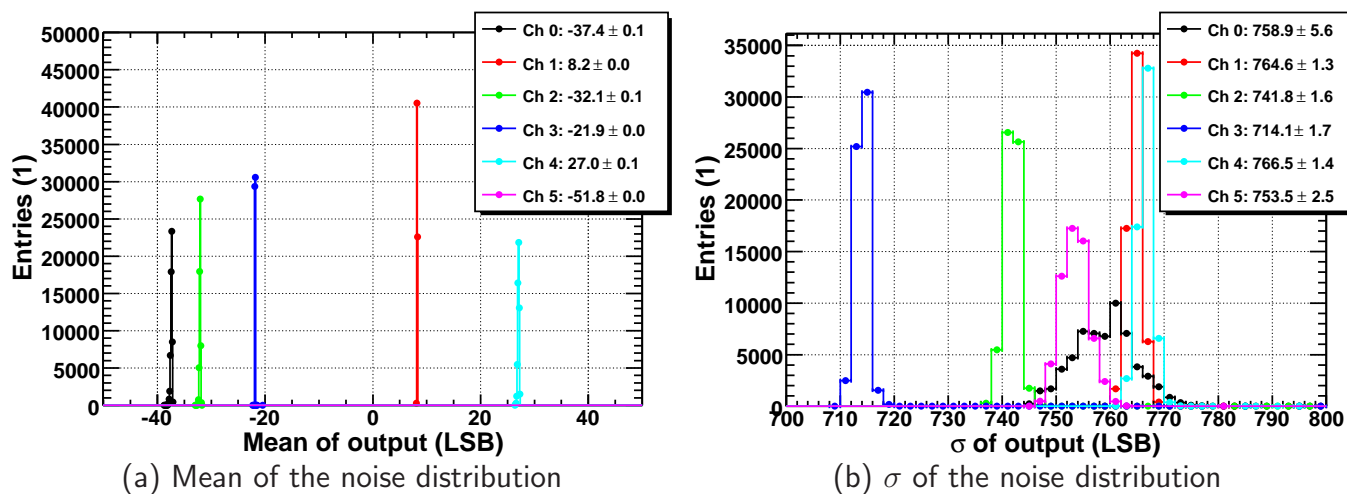


**Figure 10.1:** Distributions of the mean (a) and  $\sigma$  (b) for a recording of the inherent noise amplitudes of six commercial hydrophones over 7 days. Ch0 to ch5 denote the six channels of three AcouADC boards in one LCM used in the measurement. For each distribution, the mean and standard deviation is given in the legend.

For this measurement, the cooling of the electronics was changed with respect to setup described in Sec. 9.4, eliminating the slight systematic rise of the mean values with time observed in the previous measurement. The deviation of the distributions from the mean values is now  $\leq 0.1 \text{ LSB}_\sigma$ . The individual mean values of the distribution (Fig. 10.1(a)) changed by up to  $10 \text{ LSB}_\mu$  from the previous measurement, which is owed to the increased load created by the higher input noise levels and of no consequence to the measurements.

The mean standard deviation for the noise distributions (Fig. 10.1(b)) increased from below  $3 \text{ LSB}_\mu$  ( $\approx 2 \mu\text{V}$  at the AcouADC input) for the AcouADC board alone to  $700 - 800 \text{ LSB}_\mu$  ( $\approx 0.5 \text{ mV}$  at the AcouADC input) due to the inherent noise of the sensors (addressed further in the following section) and the ambient noise in the laboratory picked up by the sensors. The width of the histograms shown in Fig. 10.1(b) increased to  $1.3 - 5.6 \text{ LSB}_\sigma$ , the highest value being more than a factor of two higher than the next to highest level of  $2.5 \text{ LSB}_\sigma$  and probably caused by a less effective acoustic shielding for the affected sensor. Even so, the variation in the standard deviation of the recorded noise data is distributed normally, showing no systematic shift in time. The relative deviation is small:  $0.7\%$  for the highest and  $0.3\%$  for the next to highest value. Each histogram shows a long tail with few entries towards higher noise levels due to transient signals picked up by the sensors.

From these measurements it is deduced that on a level of better than one percent, the whole system can be considered stable in time; any bigger variations in the data characteristics measured in the deep-sea have to be of acoustic origin.

## 10.2 Inherent Noise

As the expected ambient noise level in the sea with values in the order of 1 to 100 mPa<sub>r</sub> (1 – 50 kHz) is small, the acoustic sensors used in AMADEUS must not only be very sensitive, but must also exhibit a low level of intrinsic noise. Furthermore, the sensors have to be insensitive to electronics noise coupling in through the power supply from the DAQ system. Measurements were conducted in two different laboratories to evaluate the inherent noise of the 18 sensors chosen to be integrated on IL07: in a laboratory at the ECAP and at the integration site for ANTARES lines at the CPPM<sup>1</sup>. At the former site measurements were carried out in an electrically and acoustically shielded surrounding using the reduced power supply chain of the calibration measurements. At the latter site, the measurements were conducted after the integration of the IL07 and the full string including the full power system were used. In that laboratory it was not possible to shield the sensors from ambient noise for this measurement.

### 10.2.1 Equivalent Noise Level

Exemplary amplitude distributions for recordings at the standard settings (G10, DS2 and R1) are shown in Fig. 10.2. The distributions are gaussian, shown by a fit to the histograms, with a broadening to higher amplitudes due to ambient transients, especially for the commercial hydrophone.

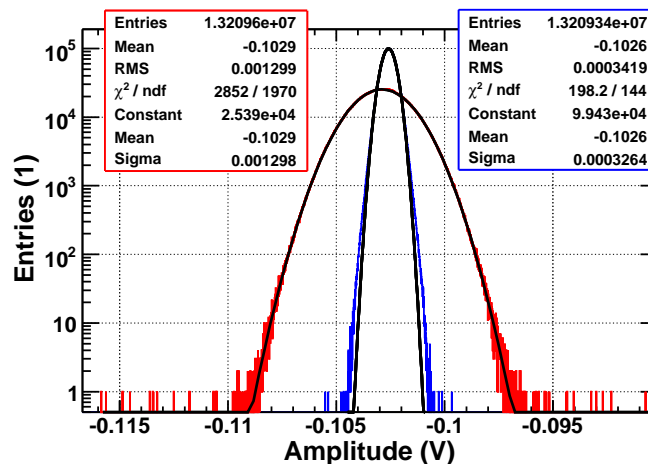


**Figure 10.2:** Amplitude distributions of noise measurements at the CPPM of a custom-designed hydrophone (red, LTI105) and a commercial hydrophone (blue, HTI010). The legends give the characteristics of the histogram, as well as those of a gaussian fit (black) for each of the two sensors.

The *equivalent noise level* of the sensors is defined here as the standard deviation of the recorded amplitudes in V (or Pa) at the AcouADC input, taking into account the board calibration (or board and sensor calibration). For measurements performed at the ECAP, this quantity

<sup>1</sup>Abbr. for *Centre de Physique des Particules de Marseille* [101].

was evaluated for different gain settings and averaged separately for the custom-designed and commercial hydrophones, respectively. The resulting levels are shown in Fig. 10.3.

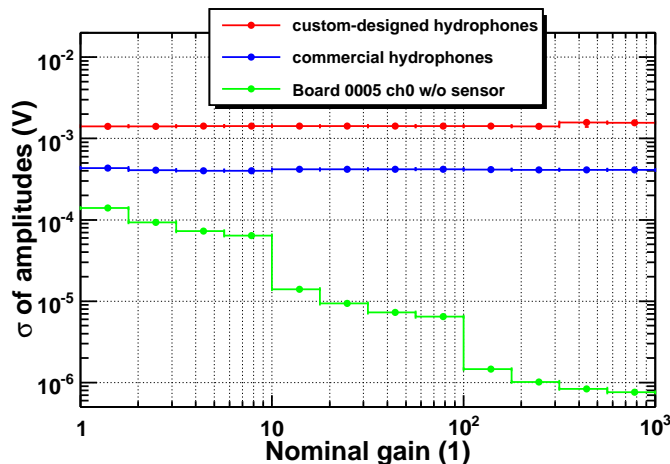


**Figure 10.3:** Equivalent noise levels defined as the standard deviation of the amplitude distribution at the AcouADC input. The level for each gain setting is shown averaged over the six custom-designed hydrophones (red) and over the 12 commercial hydrophones (blue) on IL07, respectively. The noise component generated by the DAQ hardware is shown in green. The individual measurements were taken at downsampling 2 (DS2) and half range (R1) with time slices of 26.2 s lengths.

As expected, the equivalent noise level of the sensors calculated at the input of the AcouADC boards does not change significantly with the gain setting. This confirms that the gain calibration was done accurately and that the intrinsic noise of the boards is negligible. The average noise level for the custom-designed hydrophones is  $(1.42 \pm 0.13) \text{ mV}_\sigma$ , a factor of  $3.43 \pm 0.45$  higher than the one of the commercial hydrophones, which was found to be  $(0.414 \pm 0.019) \text{ mV}_\sigma$ . The higher noise for the custom-designed hydrophones is, however, partly compensated by their higher sensitivity up to frequencies of  $\approx 40 \text{ kHz}$ .

The inherent noise component of an AcouADC board is shown also in the plot (in green). It falls off with rising gain due to the amplification implemented in two stages in the analogue part (cf. Sec. 9.2). At gain 1.00 the intrinsic noise of the board is a factor of  $3.0 \pm 0.1$  lower than the inherent noise of the commercial sensors. The factor rises with the nominal gain; at the standard setting of G10, the intrinsic noise of the board is already a factor of  $29 \pm 1$  lower than the sensor noise.

## 10.2.2 Noise Power Spectra

As the noise level is almost equal for all gains, the standard setting (G10) was used to evaluate the power spectrum density of the inherent sensor noise. The spectra of the recorded noise data in time slices of 26.2 s length are presented in Fig. 10.4(a) for custom-designed hydrophone LTI105 and commercial hydrophone HTI010.

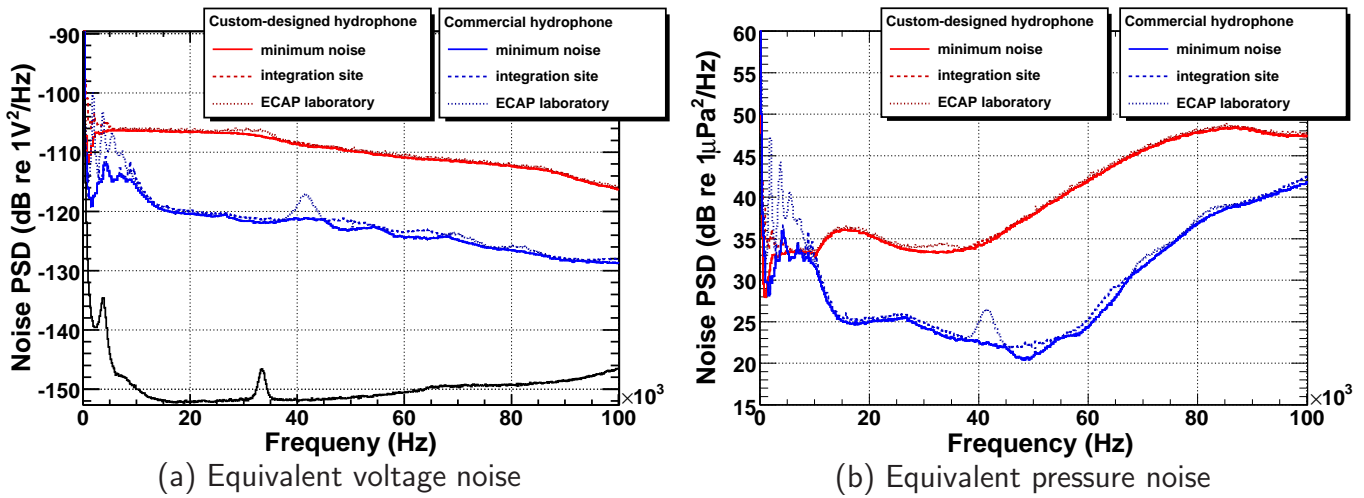


**Figure 10.4:** Power spectrum densities of the sensor intrinsic noise of a custom-designed hydrophone (red, LTI105) and a commercial hydrophone (blue, HTI010). The intrinsic noise as calculated at the AcouADC board input is shown on the left (a). For comparison the intrinsic noise of an AcouADC board (0005, ch0) is shown in black. The equivalent pressure noise, which is taking into account the overall sensor sensitivity is shown on the right (b). For each sensor a measurement at the integration site (dashed line) and the ECAP laboratory (dotted line) is shown and the minimum of the measurements (solid line). The curves for the noise measurements at different sites do not differ much and are thus hardly distinguishable.

The intrinsic noise level of an AcouADC board – shown in black – is only significant for frequencies below 500 Hz and above 120 kHz (not shown); thus, the recorded data represent the intrinsic noise of the sensors in the broad frequency range between 500 Hz and 120 kHz with potential components from induced electronics noise from the power supply, the laboratory and ambient noise leaking through the shielding.

The intrinsic noise of the sensors itself is composed of the noise of the piezo-ceramic and the sensor electronics (amplifier and filter). The first component is related to the resonance structure of the piezo element and thus to the sensitivity<sup>2</sup>. This explains the rounded steps observable in Fig. 10.4(a) for the custom-designed hydrophone at frequencies of  $\approx 2$ , 35 and 85 kHz. For the commercial hydrophone some external influences are superimposed. The peaks between  $\approx 2$  and 15 kHz and between  $\approx 38$  and 46 kHz are assumed to originate from electronics noise produced by interferences of the power supply, as they are more prominent in the ECAP measurement (where no full power supply chain was used) and not observable for the custom-designed hydrophone with its different electronics and higher overall noise level.

For the calculation of the equivalent pressure noise level, the overall sensitivities of the hydrophones are used (cf. Fig. 6.3), with a maximum sensitivity at 32 and 46 kHz for the custom-designed and commercial sensor, respectively. The structures in Fig. 10.4(b) below the maximum sensitivity of the individual sensors are governed by the resonance structure and the

<sup>2</sup>A detailed description of the noise behaviour of the acoustic sensors is given in [48,80].

external noise. Above those frequencies, the sensor becomes less and less sensitive, whereas the intrinsic noise of the piezo element and amplifier does not reduce by the same amount leading to a rising equivalent noise level. It should be noted that using the overall sensitivity of the sensors to deduce the equivalent noise level is only valid for isotropic external noise, especially for frequencies above the main resonance, where the directional sensitivity is not uniform. This fact will become important later on, when comparing the intrinsic noise to the measured noise in the deep-sea.

Table 10.1 summarises the equivalent inherent noise level of the hydrophones and presents for comparison the expected ambient noise in the sea at different sea-states from Sec. 4.3.1. The noise levels are given for two frequency ranges of interest with respect to acoustic particle detection (1 – 50 kHz and 1 – 100 kHz) and are deduced by integration over the corresponding noise power spectrum density.

Sensor	1 – 50 kHz		1 – 100 kHz	
	(mPa)	(mV)	(mPa)	(mV)
custom-designed	13	0.96	47	1.1
commercial	5.4	0.26	16	0.28

Sea-state	1 – 50 kHz (mPa)	1 – 100 kHz (mPa)
SS0	6.2	7.1
SS1	17	18
SS3	52	53
SS6	130	130

**Table 10.1:** Upper table: Equivalent inherent noise level in mV at the AcouADC input and in mPa using the sensor sensitivity for exemplary hydrophones (custom-designed: LTI105, commercial: HTI010). Lower table: Expected ambient noise level in the deep-sea for different sea-states for comparison. The noise levels were calculated by integrating the corresponding noise power spectrum densities from Fig. 10.4 and Fig. 4.3 within the given frequency ranges.

The intrinsic noise of the hydrophones is comparable to the ambient noise of the sea at a sea-state of SS0 – SS1 for 1 – 50 kHz. For most weather conditions the AMADEUS system is therefore sensitive to the ambient noise of the deep-sea. The rise of the hydrophone noise for higher frequencies degrades the performance in the wider frequency range of 1 – 100 kHz, where both noise levels are comparable with a sea-state of SS1 – SS3. In the smaller frequency band, the difference in the inherent sensor noise between the two types of sensors decreases to a factor of 2.4, whereas in the wider range they differ by a factor of 2.9. The latter value is comparable to the factor of  $3.4 \pm 0.5$  deduced in the previous section, where the full digitisation frequency range was considered.

A comparison of the inherent noise of the hydrophones to the actual recorded ambient noise and the Knudsen spectra will be given in a later section (cf. Sec. 12.2).



# Chapter 11

## Commissioning of AMADEUS on IL07

The installation of a line of the ANTARES detector requires two sea operations. In the first operation the line is lowered from a ship to its position on the sea bed. A precision of a few meters with respect to the nominal position is reached by the usage of a combined GPS and acoustic positioning system. In the second step, the line is connected to the JB (and thus to the shore) via an interlink cable for power supply and data transfer using a submersible *remotely operated vehicle (ROV)*<sup>1</sup>.

The IL07 was installed at its position on July 18th, 2007. Due to a temporary unavailability of the ROV it was connected to the JB almost five months later on 5th of December, 2007. Within the first hour after they had been powered up, the three acoustic storeys on the IL07 provided the first AMADEUS data from the deep-sea. All LCMs were found to be responding. The DAQ boards have been fully functional, the slow-control communication with the AcouADC boards has been established and all commands for the different settings in gain, downsampling and range are acknowledged and realised in the board. The acoustic data of all LCM can be transmitted at transfer rates of  $\approx 30$  Mbit/s, allowing for a continuous read-out of the sensors at 250 kSamples/s (downsampling 2) ( $\approx 26$  Mbit/s). This downsampling was chosen for data-taking during the commissioning phase of the project. Since their first initialisation, the acoustic storeys have continuously transmitted data to the shore, with the exception of some short time intervals, when errors in the connection to or errors at the ANTARES DAQ board arose and data-taking had to be resumed after a restart of the units.

At first, the full data were stored on disk with a rate of  $\approx 10$  MByte/s. To reduce the amount of unfiltered data, the recording was eventually reduced to 10s every hour on the 17th of December, giving a stored data rate of  $\approx 2$  GB/day. This raw data are used to monitor the behaviour of the system and to evaluate the efficiency of the filters. The analysis in the following chapter is based on the raw data taken in the first month of operation and will concentrate on the performance and the potential of the setup. It is foreseen that the full data stream will be filtered on-line and events of interest will be recorded, once the filter algorithms have been adapted to the ambient parameters deduced from the raw data.

---

<sup>1</sup>The required personnel and equipment for the ANTARES sea operations are provided by the sea research institute *IFREMER* [102], a member of the ANTARES collaboration.

## 11.1 Determination of Standard Settings

From laboratory measurements and the parametrisation of the ambient noise in the sea a standard setting of gain factor 10.0, downsampling 2 (250 kSamples/s) and range 1 (half range, 2V) was deduced and used for the first check of the system in the deep-sea. This set was compared with the actual conditions in the sea and found to be well adapted.

Figure 11.1 shows a comparison of the amplitude distributions of 10.4 s of data from the sensors LTI105 and HTI010 for the three coarse gain settings G1, G10 and G100 (at DS2, R1). The data was taken in consecutive runs for each setting at a sea-state SS3, which is the expected average condition and is determined by a wind measurement at the shore. For better comparability, the amplitudes are given as ADC output values in LSB. The distributions are gaussian, as expected for mainly white ambient noise. The width of the distributions for each sensor scales with the gain within an inaccuracy of 5% (75.9, 770 and 7930 LSB for LTI105 and 17.8, 187 and 1750 LSB for HTI010), where the error can be attributed to gain uncertainties as well as to slightly changing environmental conditions between the runs. Compared to the commercial sensor, the standard deviation for the custom-designed sensor is higher by a factor of 4.3.

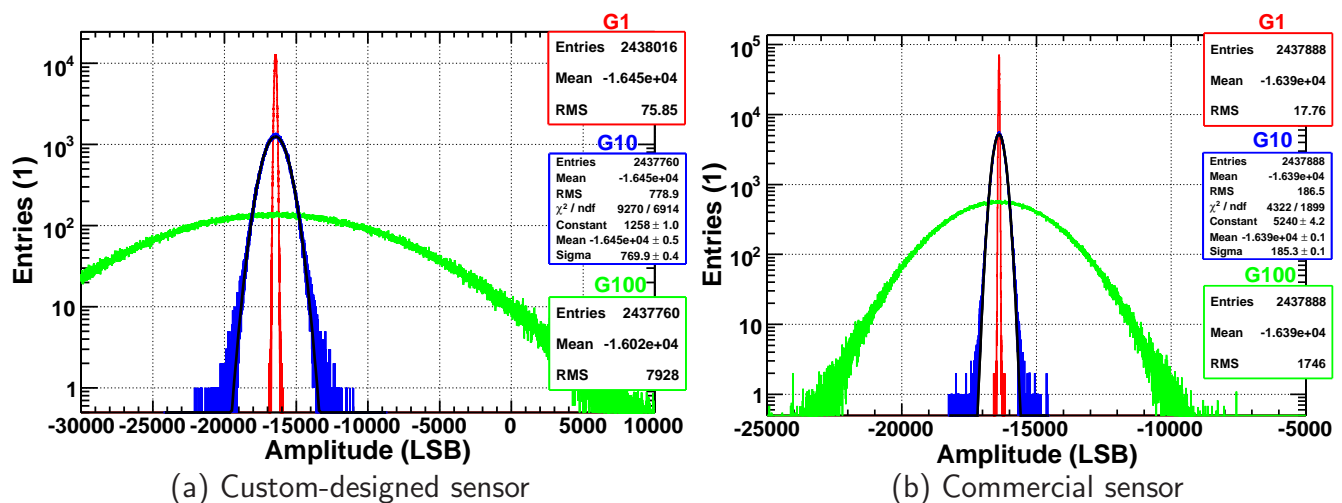


**Figure 11.1:** Amplitude distributions for gain settings of G1 (red), G10 (blue) and G100 (green) for a custom-designed sensor (a, LTI105) and a commercial sensor (b, HTI010). For G10 a gaussian fit (black solid line) was applied with parameters as shown in the legend.

The distributions at a gain factor of 10.0 leave for both sensor types (standard deviations of 779 and 187) the possibility to resolve the ambient noise at lower sea-states and the possibility to record the ambient noise at higher sea-states without saturation, leaving enough dynamic range for high amplitude transients, as well. For a gain factor of 1.00 the standard deviation of 17.8 for HTI010 would not allow for the first possibility and at a gain factor of 100 the noise measured with LTI105 saturates the ADC range for the given conditions. Even though the gain setting can be individually chosen for each sensor, the usage of an overall gain factor constitutes a facilitation for the data analysis.

Slight deviations from the gaussian shape at high amplitudes, visible in Fig. 11.1 for G10 as a deviation from the gaussian fit, hint at transient signals of acoustic origin. The  $\chi^2/\text{ndf}$  of the fits with values greater than 1 are artifacts of the ideal ADC transfer function used in the data calibration. To minimise these artifacts, the half range setting R1 was used as standard so far. Due to the width of the distribution at a gain factor of 10.0, the non-linearities of the ADC transfer-function are however insignificant for the determination of the standard deviation and spectra. To improve the dynamic range of the system it was therefore opted for using the full range setting R0 as standard, despite its higher non-linearity at the zero level input.

## 11.2 Comparison of Sensors

With the same sample of data as used in the previous section (G10, DS2, R1 for 10.4 s at SS3), the comparability between measurements with the same type of hydrophones was tested. Figure 11.2 shows the amplitude distributions separately for the custom-designed sensors and the commercial ones<sup>2</sup>; Fig. 11.3 shows the power spectrum density.

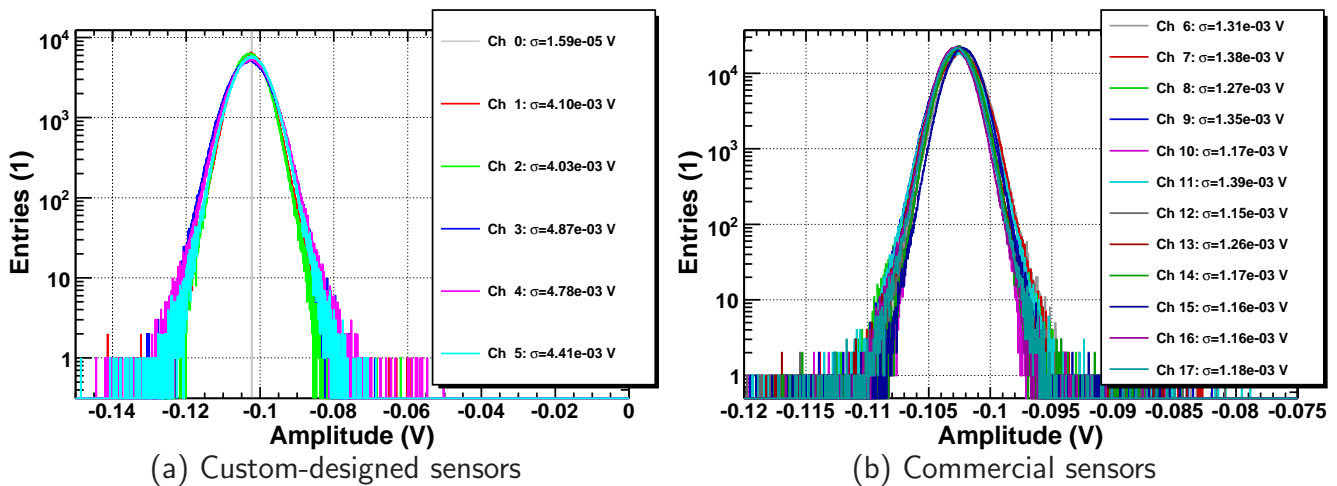


**Figure 11.2:** Amplitude distributions for 10.4 s of data from the six custom-designed hydrophones on IL07 storey 3 (a) and from the 12 commercial hydrophones on IL07 storeys 2 and 6 (b). The legend gives the colour coding for the AcouADC board channels and the standard deviation of the distributions.

It was found that the data of the custom-designed sensor at AcouADC board channel ch0 (storey3) exhibits a standard deviation more than two orders of magnitudes lower than that of the other sensors of that type, hinting at a defective sensor. The power spectrum density

<sup>2</sup>The sensors are labelled in the following with the AcouADC board channel they are attached to, arrayed by an LCM tag and not the storey number. The board channels are numbered from ch0 to ch5 for IL07 storey3, equipped with custom-designed hydrophones, ch6 to ch11 for IL07 storey 6 and ch12 to ch17 for IL07 storey 3 (both equipped with commercial hydrophones).

of the same sensor, shown in Fig. 11.3(a), exhibits a noise level comparable to the intrinsic noise of the AcouADC board without sensors. This behaviour has been found in every analysis conducted for more than one month of data-taking. Thus this sensor is considered defective, giving a total of 17 out of 18 sensors working. Taking into account that the pressurisation of up to the 240 bars at the ANTARES site is considered as the main point of failure for the sensors and that the line was installed at the sea-bed almost five months before the activation of the sensors, the 94% working sensors are a full success and exceed expectations.

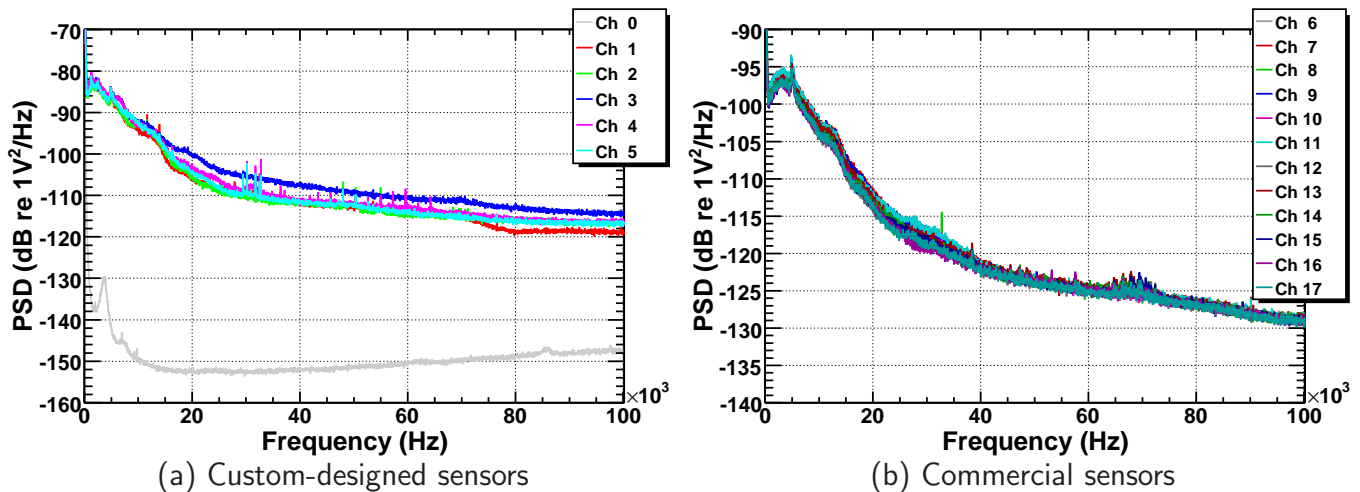


**Figure 11.3:** Power spectrum densities for 10.4 s of data from the six custom-designed hydrophones on IL07 storey 3 (a) and from the 12 commercial hydrophones on IL07 storeys 2 and 6 (b). The legend gives the colour coding for the AcouADC board channels. The sensor denoted by ch0 is considered defective.

The rest of the custom-designed hydrophones shows the same behaviour both in amplitude distribution and in the spectra, solely the sensor at ch3 deviates for frequencies above 15 kHz for more than 4 dB. The average recorded standard deviation for this data sample is  $(4.44 \pm 0.38)$  mV as compared to an intrinsic noise level of  $(1.42 \pm 0.13)$  mV measured in the laboratory. The twelve commercial sensors show an even better comparability, as it was also observed for the calibration of all sensors in the laboratory. For this type, the standard deviation lies at  $(1.245 \pm 0.091)$  mV and the intrinsic noise at  $(0.414 \pm 0.019)$  mV. The recorded noise in this data sample is more than a factor of 3 higher than the intrinsic noise of the system recorded in the laboratory, giving a first hint to the observation of ambient noise with the system.

This ambient noise in the deep-sea deforms the spectra as compared to the intrinsic noise spectra of the sensors recorded in the laboratory, where the noise level was essentially flat with deviations below 10 dB from 1 to 40 kHz. For the sea data, the acoustic noise level in the same frequency range falls by 30 dB with rising frequency. For a comparison of the noise levels of sea data with laboratory data in more detail cf. Sec. 12.2. For all sensors a broadening of the amplitude distribution at high amplitudes again hints to transient signals (cf. Fig. 11.1). The sharp spikes observable in the spectra are considered to be of electronic origin; however, their signal energy is small due to their small bandwidth.

The comparability of the sensor data for the same hydrophone type justifies the choice of one hydrophone of each type to show the overall features of the data. However, there is a huge potential to detect finer features in the noise data by comparing the data of different hydrophones. This task, as many more, will be covered in later studies.

## 11.3 System Stability

One of the first checks of the system performance in the sea was again the analysis of the stability of the system, in comparison to the values obtained in the laboratory. The distributions of the mean and standard deviation of data recorded over a period of 12 days are shown in Fig. 11.4 and Fig. 11.5, respectively for the two sensor types. Each of the 310 entries in the distributions is calculated once every hour for a period of 1.5 s.

The mean of the recorded data (cf. Fig. 11.4) exhibits no systematic evolution in time. All distributions are gaussian, but with different width ( $\lesssim 1.1 \cdot 10^{-5} \text{ V}$ ) and centre ( $|\lesssim 5 \cdot 10^{-4} \text{ V}|$ ). These observations are consistent with the ones observed in the laboratory and give a first clue that the ANTARES line electronics does not significantly influence the acoustic data quality.

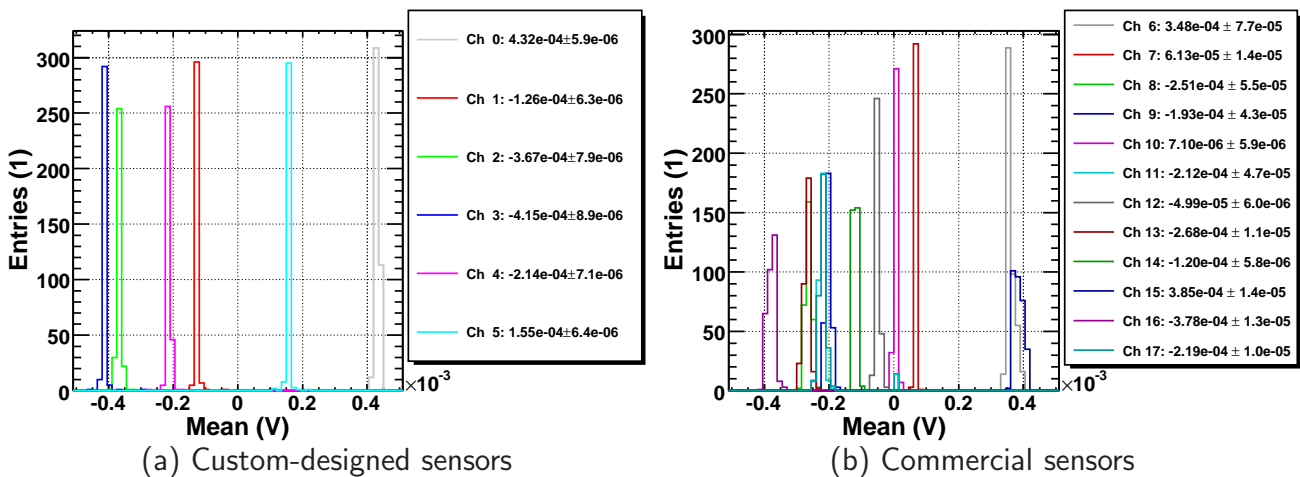


**Figure 11.4:** Distributions of the mean of data for a recording of all 18 sensors during 12 days from 1.5 s long time slices analysed once every hour. Ch0 to ch5 in (a) denote the custom-designed hydrophones. Ch6 to ch17 in (b) mark the commercial hydrophones. For each distribution, the mean and standard deviation is given in the legends in Volts.

The behaviour of the standard deviation (Fig. 11.5) is changed as compared to the laboratory, where the distributions of this parameter were gaussian with a relative width of well below 1%. The sea data exhibit distributions with tails towards higher standard deviations and a highly increased relative width. For the functional custom-designed sensors the average standard deviation of the data is  $(4.6 \pm 3.0) \text{ mV}_\sigma$  (laboratory:  $(1.42 \pm 0.13) \text{ mV}_\sigma$ ), for the commercial ones it is again lower at  $(1.4 \pm 1.0) \text{ mV}$  (laboratory:  $(0.414 \pm 0.019) \text{ mV}_\sigma$ ). The average values

are comparable with the ones found for the data sample recorded at SS3 in the previous section. The variability of the noise level is high with around 70% of the mean level. As the system was extensively tested in the lab, the assumption that this variation can be generated in the DAQ system can be ruled out; it has to be of acoustic origin.

The observation can be explained assuming the agitation of the sea surface, i.e. the sea-state, as the main contribution of the ambient noise in the deep-sea, which will be supported with more data in the following chapter.

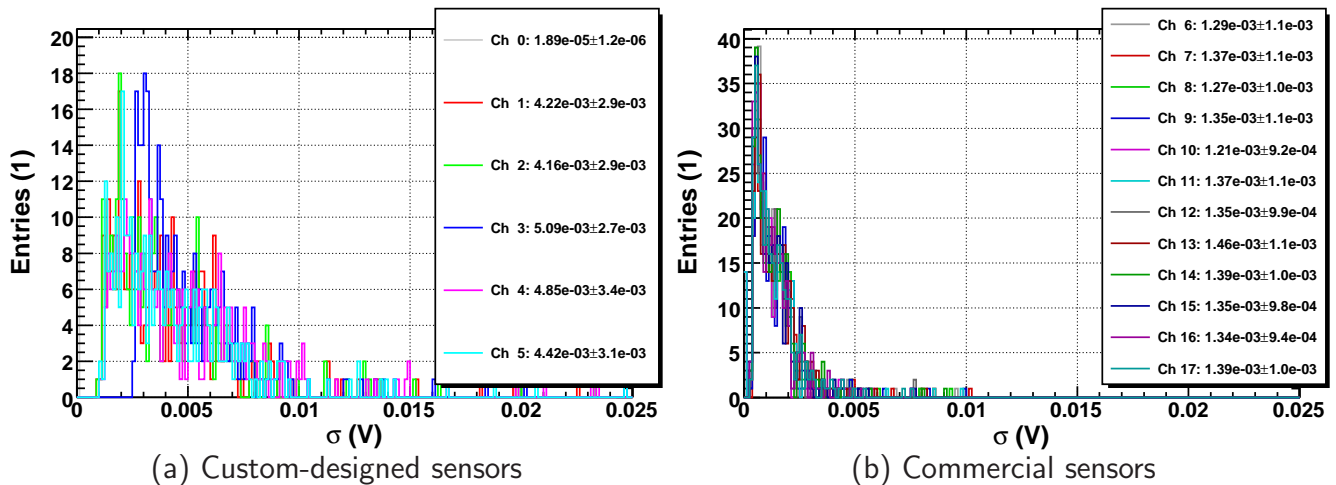


**Figure 11.5:** Distributions of the standard deviation of data for a recording of all 18 sensors during 12 days from 1.5 s long time slices analysed once every hour. Ch0 to ch5 in (a) denote the custom-designed hydrophones. Ch6 to ch17 in (b) mark the commercial hydrophones. For each distribution, the mean and standard deviation is given in the legends in Volts.

# Chapter 12

## Analysis of Sea Data

In this chapter a first look at the acoustic data acquired with AMADEUS on IL07 within the first month of its operation is presented and the potential of AMADEUS to investigate the acoustic environment of the deep-sea with the ultimate goal of detecting UHE cosmogenic neutrinos is highlighted. The analysis presented here is preliminary and addresses only basic properties of the data, but already gives a strong indication that the chosen setup of sensors provides a unique opportunity to investigate the full spectrum of the questions addressed in this work, which have to be solved towards acoustic neutrino detection.

The system response to exemplary transient signals will be shown, demonstrating the comparability of the sensor data, the directional sensitivity and reconstruction possibilities at the level of individual storeys. Additionally, an investigation of the ambient noise and its temporal correlation with weather data from a station near the ANTARES site is presented.

### 12.1 Transient Signals

#### 12.1.1 Acoustic Positioning Signals

The acoustic positioning system with its transponders (*pingers*) placed on the BSSes (cf. Fig. 5.2) of all ANTARES lines at a height of  $\approx 2$  m above the sea-bed and at autonomous *acoustic pyramids* surrounding the detector emits transient signals (*pings*) at predefined times – sinusoidal waveforms of 1 – 2 ms length, at specified frequencies in the range between 44.5 and 60.2 kHz and an emission strength in the order of 160 dB re 1  $\mu$ Pa (100 Pa) at 1 m distance. The acoustic positioning procedure is segmented into *cycles* with different transponders sending at different frequencies and with individual delays in each cycle to allow for a unique identification of the senders and to reconstruct the position of each receiving hydrophone of the system. The positioning hydrophones are placed at approximately every fifth storey of the detection lines and cannot be used for tests in acoustic particle detection due to their inapplicable sensitivity and read-out scheme.

The pings of the acoustic positioning signals are easily identifiable in the AMADEUS data, due to their signal strength and small band-width. They significantly change the time signal, the

amplitude histogram and the spectra of data samples. Recorded signals for a part of one cycle are shown in Fig. 12.1 for sensors on the lowest and on the highest acoustic storeys on IL07, storey 2 and 6, respectively. The recording was done at DS2, R1 and at a gain of 1.00, as for higher gains the pinger signals saturate the sensors at least on the lower storeys. Even at this lowest possible gain the pingers are easily observable at all sensors and storeys with the same temporal and amplitude structure (cf. Fig. 12.1(a)). The time intervals between the individual pings are slightly shorter in the time signal for storey 6 as compared to storey 2. This is expected, as storey 6 is located above storey 2 and the pingers are located directly below and diagonally below the acoustic setup on IL07. Within one storey (cf. Fig. 12.1(b)) the signals start at clearly distinguishable times, allowing for the reconstruction of the direction of the source. The evaluation of the arrival times of different pings combined with their known emission time and position allows for the determination of the position of each storey. This will be used, together with the data from compass and tiltmeter on each storey, to determine the position of each sensor to a centimetre precision as they float in the sea current.

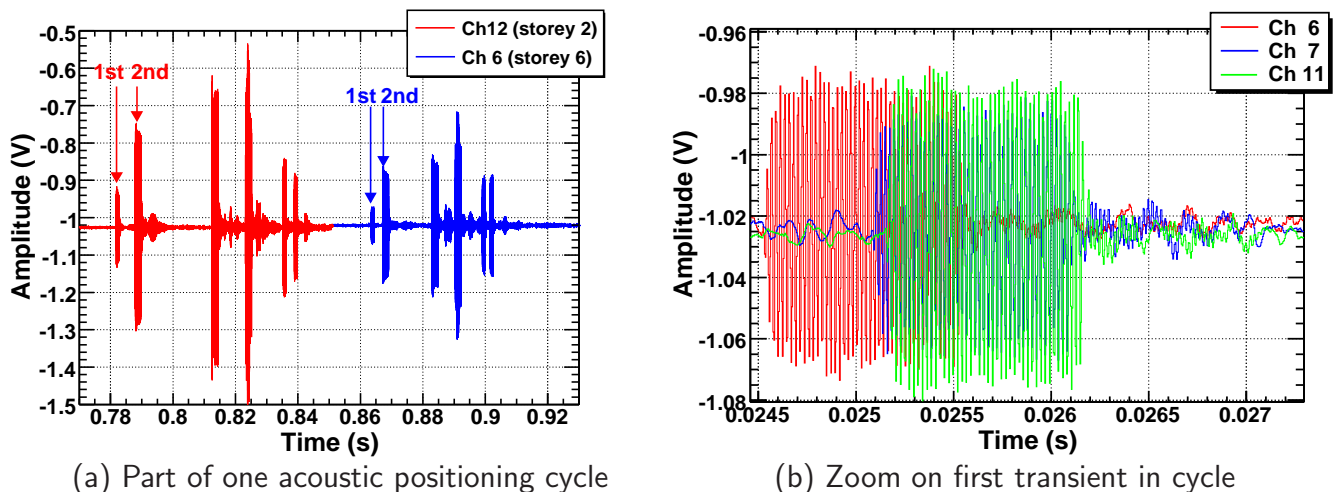


**Figure 12.1:** Recordings of acoustic positioning signals at G1, DS2 and R1. Part of an acoustic cycle recorded with one bottom sensor on storey 2 and one on storey 6, respectively is shown in (a). Marked are the first and second ping in the cycle; a zoom (with different time scale) of the first ping for three sensors on storey 6 is shown in (b) (ch6 being at the bottom, ch7 and ch11 at the top of the storey). For visibility the signals of the other three sensors are not shown.

Using the differences in the average arrival time in the three storeys and assuming the detector line to be exactly vertical, the horizontal distance of the pingers from the BSS of IL07 can be estimated. For the first signal of the pinger cycle in Fig. 12.1(a) it is consistent with 0 m, i.e. the transmitter is located at the BSS of IL07. This is already suggested by the arrival times of this signal shown in Fig. 12.1(b) with almost identical signal beginnings in the upper sensors (ch7 and ch11). For the second signal of the cycle a vertical distance of  $\approx 60$  m was deduced, consistent with an emission from the BSSes of the detection lines L1 or L2. Due to the, at the time of writing, missing positioning determination, the source direction could not



be reconstructed.

Amplitude distributions for a data sample recorded during two subsequent 6.3 s long measurements with the sensors LTI105 and HTI010 (ch3 and ch14, respectively) around the start of a pinger cycle are plotted in Fig. 12.2. Around their mean value, the gaussian distribution of the ambient and system inherent noise just before the cycle start (shown in red) is reproduced by the distribution of the data sample containing pings (shown in blue). However, a substantial part of the distribution is shifted to higher amplitudes, showing the transients by a broadening of the distribution. This can be used to distinguish ambient noise from transients and shows that the recording of transients does not influence the recording of noise, i.e. the linearity of the signal response of the sensors.

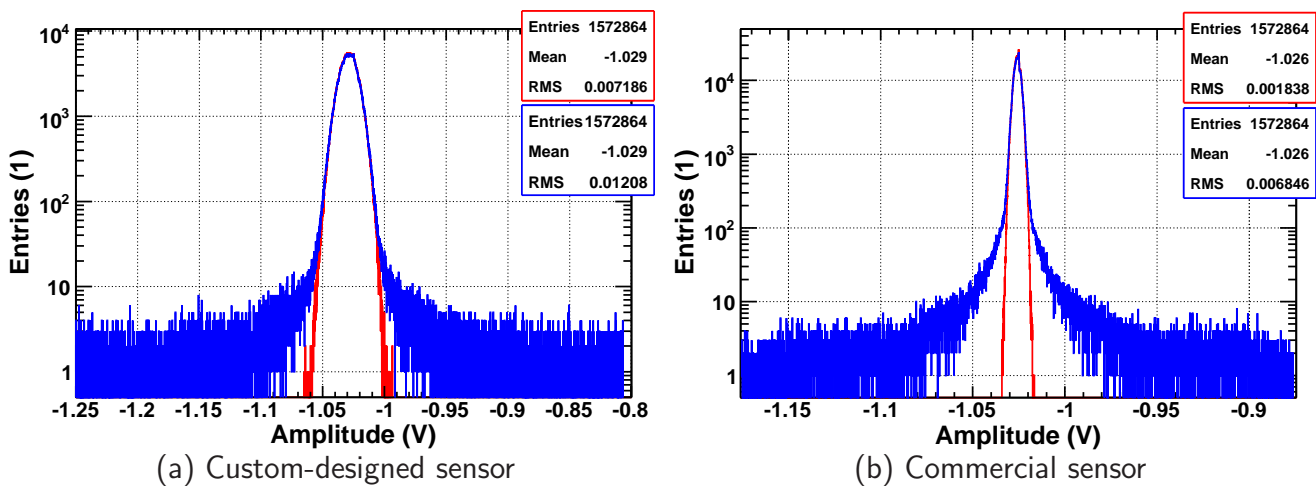


**Figure 12.2:** Amplitude distributions for signals recorded with a custom-designed sensor (a, LTI105) and a commercial sensor (b, HTI010). In each case two time intervals of 6.3 s length are represented, in red just before an acoustic positioning cycle and in blue containing a full cycle.

The acoustic signals of the ANTARES positioning system are also clearly distinguishable from the background in the third signal representation form used in this work: the frequency spectrum. Figure 12.3 shows spectra and a spectrograph of the same part of a positioning cycle as used for the amplitude representation in Fig. 12.2.

In the power spectrum densities (cf. Fig. 12.3(a)) the pinger frequencies are, due to the long time window chosen, observable as washed-out spikes. Due to the signal structure and the short pinger signal length compared to the sample time, the spectrum is enhanced as compared to the ambient noise data over a broad frequency range starting from  $\approx 25$  kHz. The sequence of the different signals and their frequencies is clearly observable in the spectrograph (cf. Fig. 12.3(b)), where all six frequencies of the cycle are distinguishable at 44.5, 46.5, 51.2, 53.9, 56.9 and 60.2 kHz. Their spectra are computed from 16.4 ms long data samples and thus the energy signals (pings) are better distinguishable from the power signal of the noise. Each ping is followed by a tail of up to 0.3 s at the same frequency, also observable in the time signal of Fig. 12.1. Comparable structures in the pings recorded with the AMADEUS-0 setup were

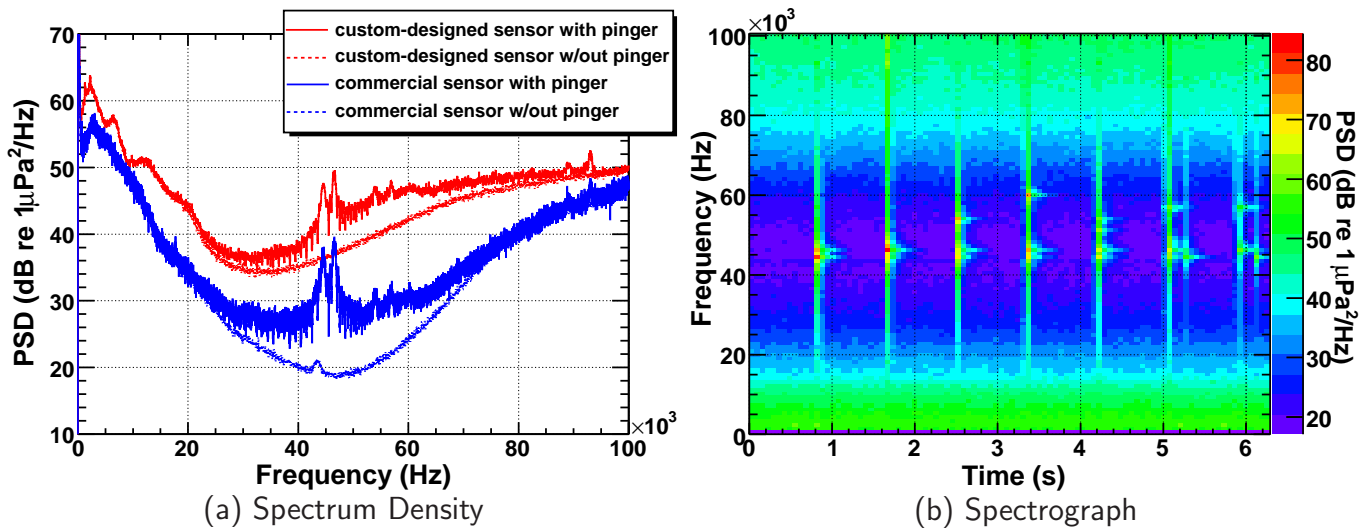


**Figure 12.3:** Spectra (a) and spectrograph (b) of 6.3 s of data containing signals of an acoustic positioning cycle. The spectra in (a) are given for sensors LTI105 in red and HTI010 in blue, both given with a noise spectrum of the same time interval of data just before the cycle for comparison. The spectrograph is given for the data of LTI105.

attributed to echos on the mechanical structures of the detector [55].

### 12.1.2 Exemplary Transient

As repeatedly mentioned, the main goal of the AMADEUS project is to evaluate the rate of background bipolar transients mimicking neutrino events. The event with the most neutrino-like signature found in this preliminary analysis – its source is probably a sea dweller – consists of a series of several signals of tri- to quadropolar form within a short time interval of 0.1 s. Two of those signals within a shorter time window of 4 ms length are shown in Fig. 12.4(a). The signal shape in each sensor is almost identical, showing again the good comparability between the sensors. Due to the repetition and the length from minimum to maximum of  $\approx 70 \mu\text{s}$  it is clearly not a sound generated in a particle cascade. The same type of signals from an unknown source was already observed in the AMADEUS-0 data [48,55].

Due to the signature of the signal it is possible to show the potential of a beam-forming algorithm developed for directional reconstruction of short transients in acoustic particle detection, especially with AMADEUS [79]. With this algorithm a scan for the source direction was made by superimposing the signals of all six sensors on storey 6 with time delays adjusted to an assumed direction of incidence. At the direction to the signal source all signals add constructively and a maximum peak arises; lower maxima are found, where combinations of less than six hydrophones add constructively. The resulting intensities of the scan over all directions in a  $1^\circ$  binning is shown in Fig. 12.4(b). The band-like shapes are the zones of constructive interference from two sensors, accumulating to the maximum at  $-48.5^\circ \pm 2.1^\circ$  in azimuthal

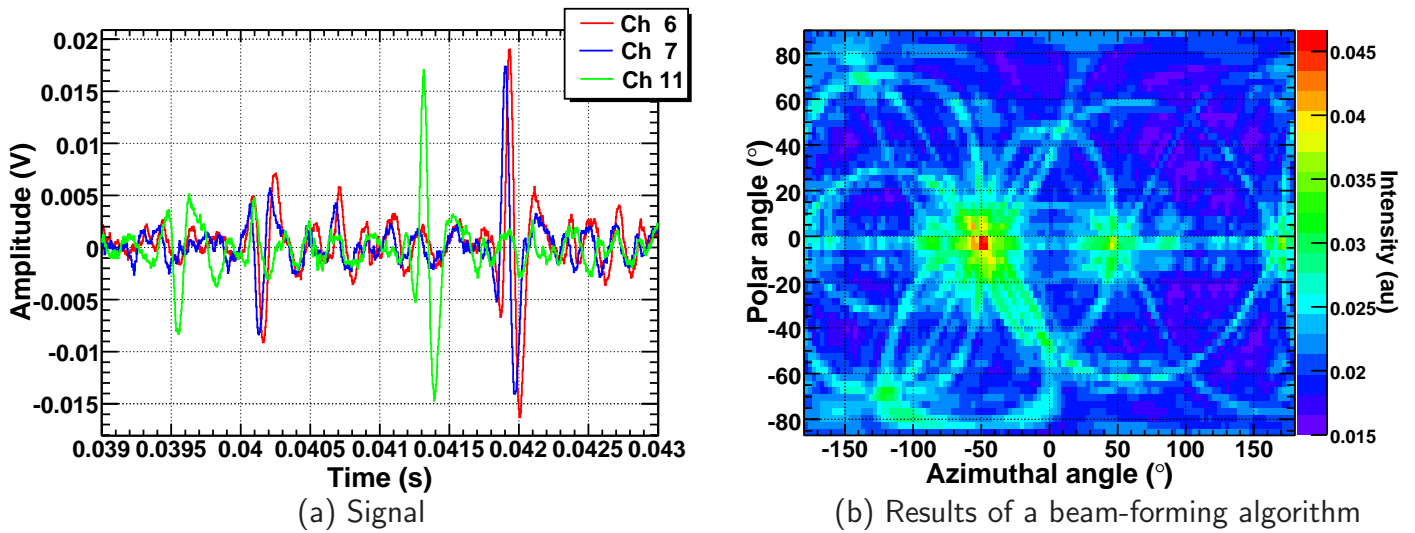


**Figure 12.4:** Signal of two short transients as recorded with three sensors (ch6, ch7 and ch11) on storey 6 (a) and scan for the direction of the signal source using a beam-forming algorithm from [79], described further in the text.

and  $-3.2^\circ \pm 2.1^\circ$  in polar angle, where the signal from all six sensors fit. The direction to the source and uncertainties ( $2.1^\circ$ ) in the determination of it were evaluated with mean and standard deviation from a gaussian fit to the two one-dimensional distributions, respectively fixing the polar and the azimuthal angle at the position of the highest intensity. To evaluate the true directional sensitivity, a more sophisticated parametrisation of the combinatorial background will have to be applied.

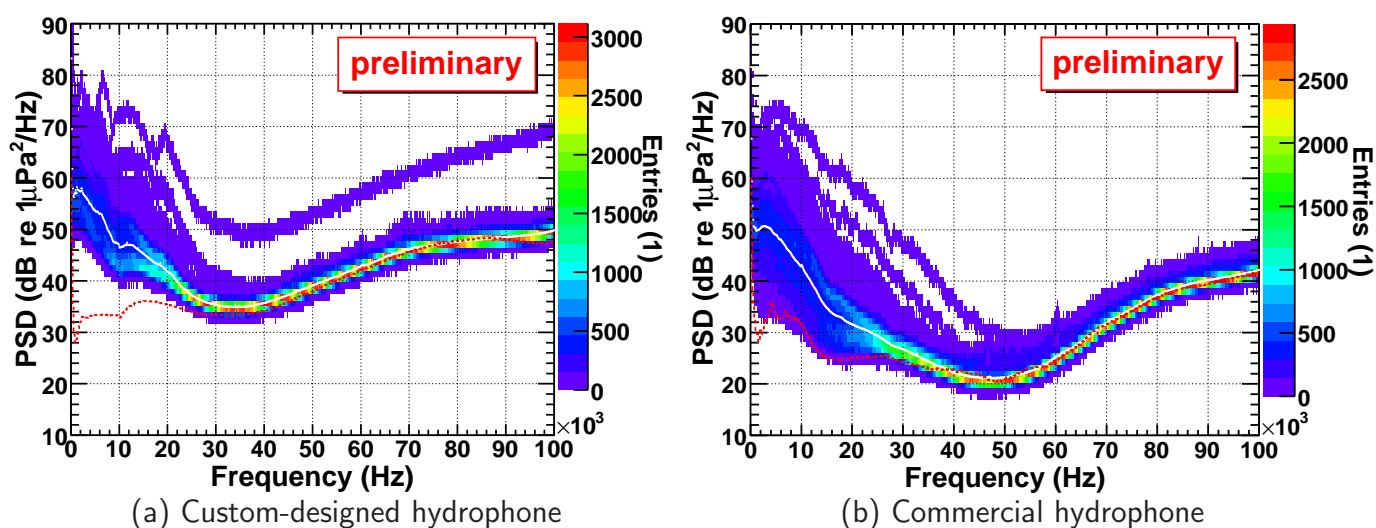
The algorithm shows the excellent directional sensitivity already at a sensor spacing of 1 m and the potential of the concept of acoustic clusters. For the determination of the source position, the algorithm can be applied individually for the three storeys of IL07 (and for the six storeys with L12) and the directions found can be matched. For this matching the position of all sensors at the time of measurement have to be determined first. Using this algorithm the signal to noise ratio for transients can be highly improved, as uncorrelated background noise is suppressed by a factor of  $\sqrt{N}$ , where  $N$  is the number of sensors analysed. Furthermore correlated noise, e.g. from the sea surface (see next section), can be separated from the uncorrelated noise.

## 12.2 Ambient Noise

In the following section, the ambient noise data recorded with AMADEUS on IL07 over 24 days are analysed, representatively using the custom-designed hydrophone LTI105 and the commercial hydrophone HTI010. The calibration of the recorded raw data was done applying the preliminary averaged hydrophone sensitivity. Therefore, especially at frequencies above the main sensitivity of the hydrophones, the presented power spectra can contain artifacts from the directional sensitivity of the hydrophones and calibration procedure, and have to be regarded as preliminary.

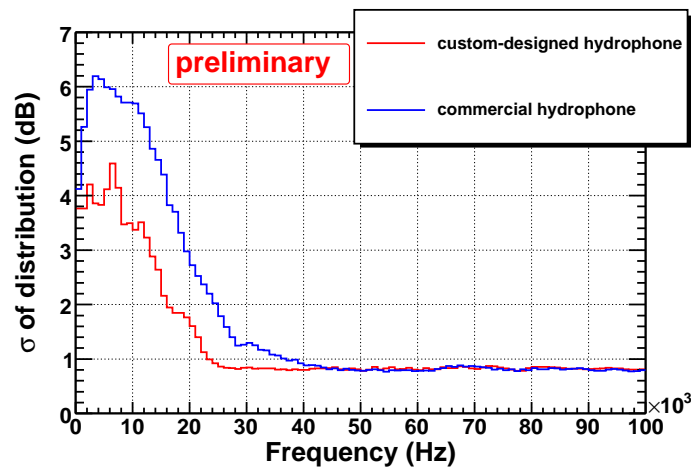
### 12.2.1 Noise Spectra

Figure 12.5 shows a scatter plot (representing the rate of occurrence by intensity) of 640 equivalent noise power spectra calculated from data samples of 8.4 s duration recorded approximately every hour during the 24 days. The mean spectra, represented by a white line in the plots, exhibit comparable behaviour: a roll-off from 0 to  $\approx 35$  and  $\approx 45$  kHz for the custom-designed and commercial sensor, respectively. The roll-off is followed by an increasing noise level up to the sampling frequency. The differences in the overall noise level and the features in the shape of the spectra (dips and discontinuities) can be partly attributed to the preliminary calibration and the different directional sensitivity of the hydrophones. The spread between individual spectra is significantly higher in the range from 1 to 25 or 35 kHz for LTI105 and HTI010, respectively, than above these frequencies. This is shown in Fig. 12.6 by the standard deviation of the distributions of 1 kHz wide profiles along the y-axis of the plots in Fig. 12.5 at a given frequency, determined using a gaussian fit. This frequency range is where the system is sensitive to the ambient noise in the deep-sea at the ANTARES site and its temporal variations, as the mean spectrum lies significantly above the inherent noise of the sensor (represented by the dashed red line in the plots) in this range. Thus, the falling part of the spectrum is generated by the ambient noise, while the raising part is mainly due to the inherent noise of the sensors.



**Figure 12.5:** Scatter plot of recorded noise spectra for a custom-designed hydrophone (a) and a commercial one (b) with a 250 Hz binning in frequency and a 1 dB binning in power. The colour coding is a representation of the rate of occurrence of the spectrum level at a given frequency. The mean spectrum for each sensor is given as solid white line, the inherent noise level recorded in the laboratory as dashed red line.

In the plot for the commercial hydrophone one individual noise spectrum is observably separated from the bulk up to frequencies of 50 kHz. The spectrum taken at the same time with the custom-designed hydrophone is lying above the bulk for the whole frequency range starting



**Figure 12.6:** Standard deviation of the recorded noise power spectrum distributions at the 1 kHz wide frequency bins from Fig. 12.5.

from 5 kHz due to saturation of the electronics. No exceptional weather conditions could be related to that time, however the weather data used are recorded at a position 30 km north of the detector position<sup>1</sup> and it is possible that e.g. a heavy rain-fall could have taken place at that time at the position of the detector.

Assuming that the ambient noise measured with the sensors and the inherent noise of the sensors is uncorrelated, the ambient noise can be evaluated up to higher frequencies by subtracting the intrinsic noise from the measured one taking into account the logarithmic nature of the power spectra. Figure 12.7 shows the average ambient noise in the sea, estimated in that way, using the averaged spectra of Fig. 12.5 and the intrinsic noise from laboratory measurements of Fig. 10.4 and compares it to the expectations for different sea-states as presented in Fig. 4.3. The difference between the mean ambient noise measured by the custom-designed sensor and the commercial one calculated at the shown frequencies is  $(6.2 \pm 2.6)$  dB (a factor of  $\approx 2$ ). This is assumed to originate from the overall sensor calibration used, which is valid for isotropic noise only (cf. Sec. 10.2.1). The difference is hence a consequence of the different directional sensitivity of the two sensor types, as the predominant part of the noise is generated at the sea surface (cf. next sections). Some small band features, e.g. at 10 kHz, add to the effect. Further studies are needed to clarify this feature.

The average sea-state derived from the wind speed measurements is SS1 to SS2. Up to  $\approx 20$  kHz, the observed ambient noise is of the level expected. Above that frequency the slope of the expected spectra flattens out due to the rising thermal noise contribution while the measured one maintains roughly the same slope. Recent studies [103] also imply a faster roll-off than the  $-6$  dB per octave of the Knudsen spectra for frequencies above 15 kHz but are limited to frequencies below 25 kHz. These studies attribute the roll-off to the sound attenuation over the noise path from the surface to the detector. The attenuation of sound waves in sea-water

<sup>1</sup>The ANTARES site is at a location of  $42^{\circ}50'N$   $6^{\circ}10'E$ , the weather station used to monitor the weather data is located at the Hyères airport at  $43^{\circ}06'N$   $6^{\circ}09'E$ .

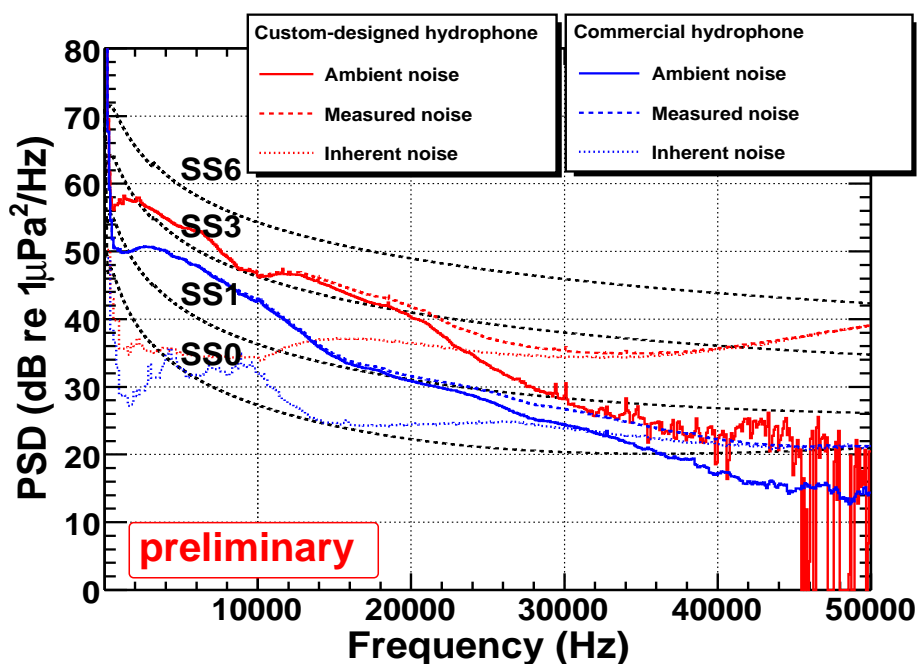


**Figure 12.7:** Measured ambient noise power density (solid lines), calculated from the measured noise spectra (dashed coloured lines) and the inherent noise (dotted coloured lines) for LTI105 (red) and HTI010 (blue). The expectation of the ambient noise (cf. Sec. 4.3.1) is shown for different sea-states as dashed black lines.

rises with the frequency and a significant damping with the depth is expected for frequencies exceeding  $\approx 10$  kHz. Also the frequency dependent sensor directionality is shown to deform the spectrum in that study. This first and preliminary analysis of the AMADEUS data seems to confirm this observation, as have already the data recorded with AMADEUS-0 (cf. Sec. 5.2.1). However, above 30 kHz the uncertainty due to the intrinsic noise of the sensors and the used sensor calibration significantly reduces the explanatory power of the data. The calibration has to be finalised for a definite statement.

The frequency band with the best signal to noise ratio between an acoustic signal of a particle cascade and the ambient noise depends on whether or not the roll-off is actually steeper than expected for frequencies above 10 kHz. That band has to be determined once the spectra have been intensively studied. In the next sections, however, it will be shown that the ambient noise might be suppressed at the sensor level. The effect of the spectral behaviour and of the level of the ambient noise on the acoustic neutrino detection method would then be significantly reduced.

## 12.2.2 Correlations in Ambient Noise

As expected, the observations of the spectra already imply that the main source of noise in the deep-sea within the frequency range of interest to acoustic particle detection is the sea surface. However, the majority of events in a possible future acoustic neutrino volume detector would

originate inside the instrumented volume or to the sides of the detector and not above it. Thus, if this noise can be reduced already on the sensor level, e.g. by rendering the sensors insensitive in the upward direction, it would lead to a highly improved detection efficiency and the threshold level for acoustic neutrino signals of 5 mPa cited in Sec. 4.3.2 could probably be lowered further. The efficiency of such a shielding is affected by the propagation features of the noise from the surface. If the emission is, at least partly, coherent and the sea surface acts as a planar source of radiation, the noise is mostly coming from directly above the detector and is partly correlated in different sensors. Such a noise emission is also reflected on the sea bed. Note that sound coming from the side has to travel longer distances and is therefore attenuated more strongly, especially at higher frequencies starting at  $\approx 10$  kHz, which leads to an improvement of the signal to noise ratio in the horizontal direction in that frequency range. A first hint to correlation in the ambient noise was found in the analysed data. The cross-correlation and auto-correlation of the data recorded with different sensors on storey 2 is shown in Fig. 12.8 for a data sample recorded at a high sea-state. As reference, sensor channel ch12 was used, which is located at the bottom of storey 2 on IL07. The cross-correlation was evaluated following the algorithm in [79] from the data of the reference hydrophone, and the data of ch13 (the one directly above it on the top of the storey) and ch15 (also at the top of storey 2, but not directly above ch12). The data used were not corrected for the hydrophone sensitivity, i.e. its power spectrum is comparable to the one shown in Fig. 11.3(b) with a maximum density at 4.9 kHz. This is the main frequency component found in all correlations shown, most pronounced in the autocorrelation.

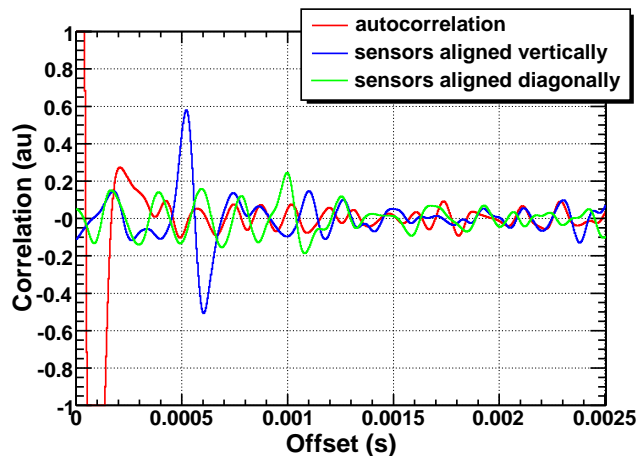


**Figure 12.8:** Auto-correlation of the sensor on ch12 (red line) and cross-correlation of ch12 with ch13 (blue line) and with ch15 (green line) for data samples of 10.5 s length recorded at sea-state SS5. The sea-state was derived from the wind observations at the time of recording.

For this plot, recorded at a high agitation of the sea surface, a bipolar structure with maximum at 0.52 ms and minimum at 0.60 ms is significantly above the background for the vertically aligned sensors. A similar, but far less prominent, structure can be seen for the diagonally aligned sensors with a maximum at 0.99 ms and a minimum at 1.08 ms. These delays correspond to

sound path lengths of 0.80 to 0.93 m (mean: 0.87 m) and 1.53 to 1.67 m (mean: 1.60 m) at the speed of sound measured at the ANTARES site of 1545 m/s. For the prominent signal, the mean path length corresponds to the distance between the sensors of 0.85 m [83], for the second no corresponding distance is found within the storey, it could be generated by a random correlation.

The same analysis was done using the upper sensor on ch15 as reference and thus looking for correlations in the noise coming from below and being potentially surface noise reflected on the sea-bed. No evidence was found for the reflection in that data. Also, the correlation analysis for the same choice of sensors as in Fig. 12.8, but for lower sea-states, provided no significant result. Correlations in data from horizontally aligned sensors could neither be found in this random test.

A complete analysis of this observation is a challenging task, as the emission is not fully coherent, the noise has a non-flat spectrum and directionality as well as attenuation play important roles. A theoretical model of the vertical directionality and the depth dependence of surface-generated ambient noise is presented in [104]. It implies that the noise arriving at a given polar angular separation from below the horizontal will be at least 10 dB lower than from the same angular separation above the horizontal. These calculations assume a dipole surface noise source radiation and a frequency of the surface generated sound of 10 kHz. This implies that a sensor insensitive in the upper hemisphere would indeed record substantially lower ambient noise. The emission of noise from the sea-surface will be studied further by the integration of one storey in the AMADEUS setup on detection line L12, where all sensors are pointing downwards. This means that these sensors are shielded from the surface sound by the mechanical arms holding them and by their insensitive lower part. The ultimate goal is to use the directionality and correlation features in the surface-generated ambient noise to efficiently suppress this main background for acoustic particle detection and thus lower the threshold for unambiguous signal identification and the energy threshold, respectively.

### 12.2.3 Correlation of the Noise Level with Weather Conditions

The ambient noise level is assumed to be mainly determined by the agitation of the sea surface, i.e. the wave height, spray and rain (cf. Sec. 4.3.1). In this section, this correlation is analysed with data from 24 days within the first month of AMADEUS data-taking in the deep-sea. For the analysis, the weather data were recorded every hour from a weather station at Hyères Airport, which was already mentioned above. This is the weather station closest to the ANTARES detector site (30 km in a northward direction) of which the data is easily accessible. There is no geological barrier between the two positions, such that at least the recorded wind data are assumed valid also for the ANTARES site, however with varying time delays due to different wind directions.

The distributions for the recorded noise level, calculated from the integral of the individual power spectra used above in Sec. 12.2 in the frequency range from 1 to 50 kHz, and the wind speed are shown in Fig. 12.9. Entries at a self-noise of 0 mPa mark time intervals where the sensors were not active, the entries at 0 kt wind speed define a calm air.



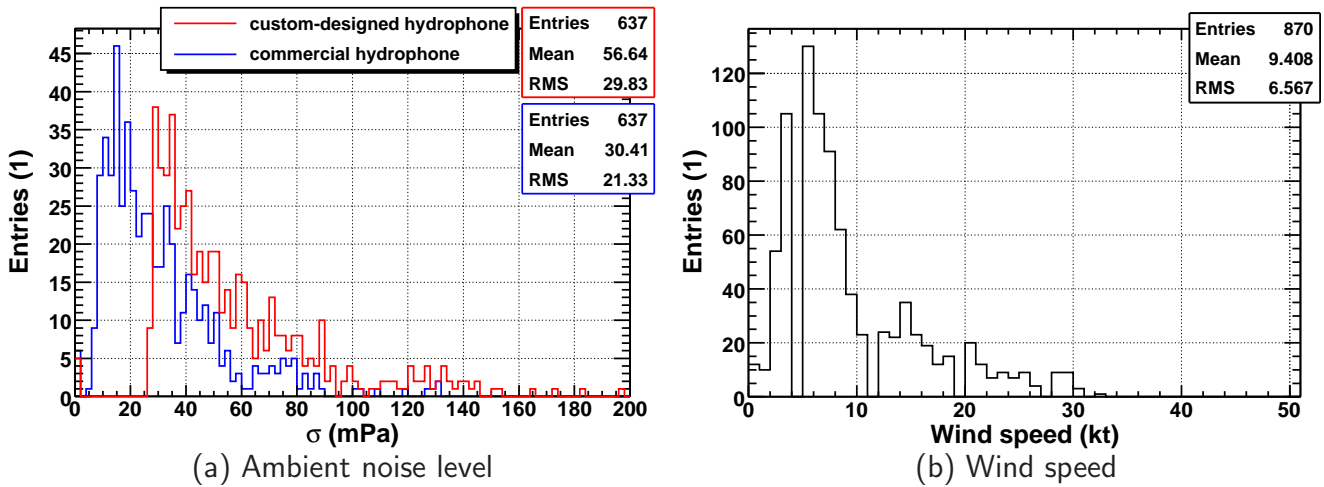


**Figure 12.9:** Distributions of the ambient noise levels (a, LTI105 (red) and HTI010 (blue)) and the wind speed (b) measured on-shore 30 km North of the ANTARES site. For both distributions the data were taken every hour for 24 days, the individual noise levels were calculated from power spectra over an 8.4 s time interval and integrated in the frequency range from 1 to 50 kHz.

Both the distribution of the noise level and the wind speed exhibit similar shapes, with a prominent peak and a long tail towards higher amplitudes. Due to the uncertainties in the sensor sensitivity mentioned in Sec. 10.2.1, the mean and standard deviation of the distributions of the noise level for the different hydrophone types differ by almost a factor of 2, as already observed with the spectra in Sec. 12.2.1. The mean wind speed of 9.4 kt implies a mean sea-state SS2, the maximum occurrence at 5 kt an SS1. These states are consistent with the sea-state derived from the observed ambient noise levels, as the mean noise levels of 57 and 30 mPa (for LTI105 and HTI010, respectively) imply SS2 to SS3 and the maximum occurrence at 28 and 14 mPa (for LTI105 and HTI010, respectively) implies SS1 to SS2 (cf. Tab. 10.1).

For the sensitivity estimates of an acoustic neutrino detector in Sec. 4.3.2 a signal detection threshold of 5 mPa was used. This threshold was defined as the lower limit at which acoustic signals from neutrinos can be unambiguously found in the background with an acoustic cluster of several sensors. The median of the measured noise level distributions lies at 47.8 and 24.7 mPa (1 – 50 kHz) for the custom-designed and commercial hydrophone, respectively. For uncorrelated noise in a storey this value would lower by a factor of  $1/\sqrt{6}$  to 19.5 and 10.1 mPa. The noise situation can be further improved by suppressing the surface noise as implied in the previous section and adapted filtering of the noise data. The ambient noise data of AMADEUS thus strengthen the assumption for the detection threshold and hint at the possibility that the value might even be lowered once the data handling is understood better.

Not only is this overall consistency was observed, but also an indication of a correlation between the wind speed and the noise level at a given time. The time evolution of the noise level and the weather conditions is given in Fig. 12.10.

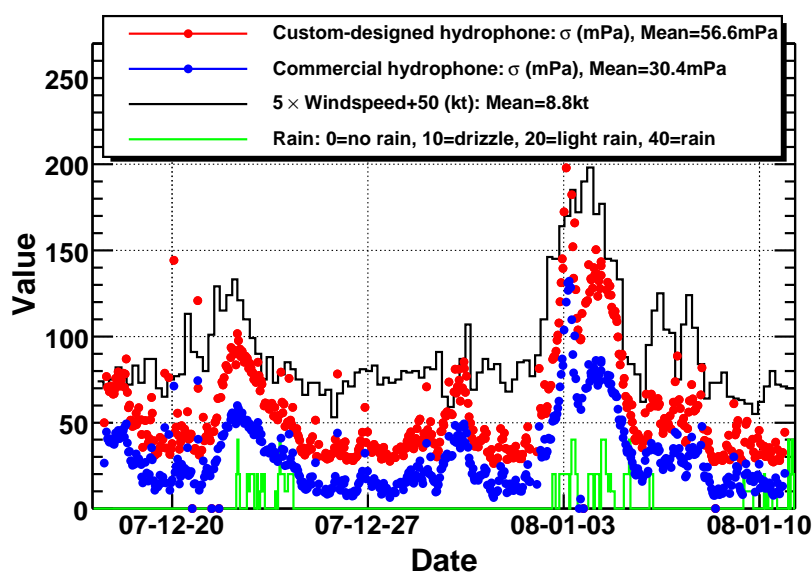


**Figure 12.10:** Time evolution of ambient noise level and weather conditions. The noise levels of LTI105 (red) and HTI010 (blue) are calculated every hour as described for Fig. 12.9. The weather conditions are represented by the wind speed (black, in kt) and the rain conditions as explained in the legend. For better visibility the wind speed is enhanced by a factor of 5 and shown with an offset of 50 kt and averaged over 5 h. The mean values for the noise and the wind speed are given in the legend as well.

Strong variations between adjacent measurement points in the noise level were observed due to short term variations, beneath one hour of length, in the ambient noise. In the randomly chosen samples analysed no transient signals were identified generating those outliers. To suppress this short term variability which can not be correlated to the wind measurements once every hour, noise levels being more than 30% higher or lower than the previous ones have been neglected in the figure. The long term variation of the wind speed, with timescales exceeding one day, tend to be followed by the noise level, for the short term variations below within one day this correlation is not observable. There are variations in the noise level not attributable to the wind measurements. This behaviour could be connected to the different positions of the wind and noise measurements, as some variations of the wind speed and direction at the weather station may not even reach the ANTARES site and vice versa.

The correlation between the wind speed and the noise level was evaluated using scatter plots, where the wind speed at a given time was plotted over the corresponding noise level. Figure 12.11 shows such intensity plots, where calm times (wind speed < 1 kt) were neglected as well as noise levels below 5 mPa (being below the inherent noise of the sensors and originating from times where the sensors were inactive). It is observable that the maximum occurrence in the noise levels lies at the maximum occurrence in the wind speed. Also, for higher noise levels the wind speed is higher. The different slopes of these tails for the two hydrophone types originate in the different sensitivities of the sensors.

A correlation factor for both of the plots in Fig. 12.11 was calculated and found to be 76% for

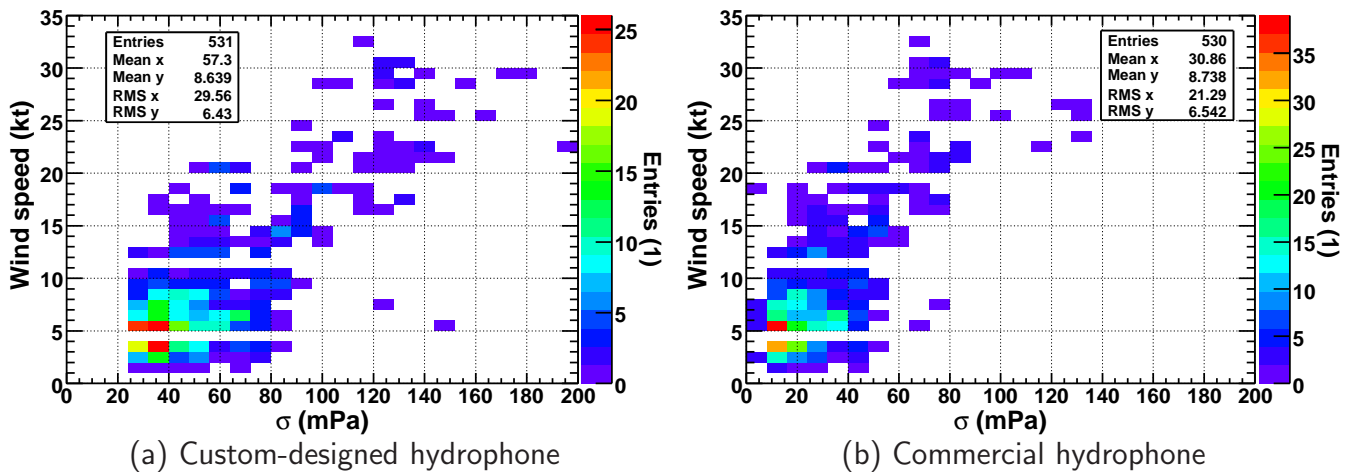


**Figure 12.11:** Scatter plot of the correlation between the wind speed and the recorded noise levels for a custom-designed hydrophone (a) and a commercial one (b). The colour coding is a representation of the occurrence of the conditions, the bin width used is 8 mPa in the noise level and 1 kt in the wind speed.

both sensors. To check for random correlations, the same correlation factor was calculated for scatter plots with the same data for the wind, but the noise data shifted in time by an offset. The resulting factors for offsets of up to  $\pm 2$  days in one hour steps is shown in Fig. 12.12.

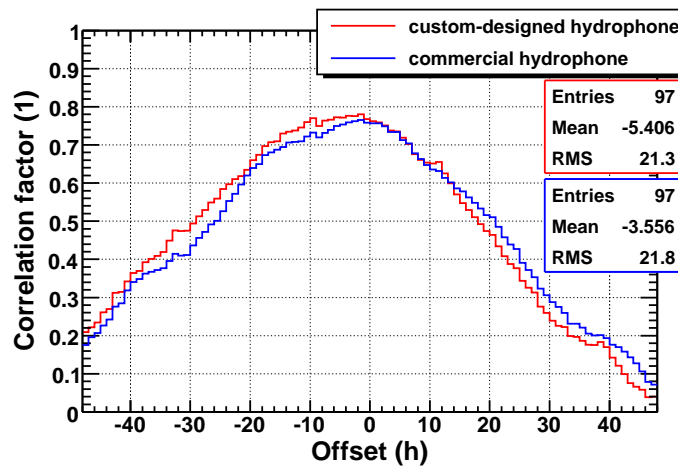


**Figure 12.12:** Correlation factors between noise level and wind speed, calculated as described in the text, where the time of the noise measurement was shifted with respect to the real time by the given offset in one hour steps with the custom-designed hydrophone (red) and the commercial one (blue).

This plot shows a falling correlation for growing offsets and thus supports the hypothesis of a correlation between the wind data and the ambient noise measured with AMADEUS. The maximum correlation factor of 78% and 77% for the custom-designed and commercial hydrophone,

respectively, lies at an offset of  $-2$  h. This offset is most probably a statistical effect but may be a consequence of the changing conditions over the distance between the site of the wind measurement and the ANTARES site (30 km). Furthermore, the time needed for the agitation of the sea surface to build up, when the wind speed has changed, may add to the offset. The good correlation of the noise levels of both hydrophone types with the weather data also implies a correlation between the noise levels measured by the two sensors. This correlation is clearly observable in Fig. 12.10.

Figure 12.13(a) shows a scatter plot of the sensor data points shown in Fig. 12.10 but without neglecting any outliers. Only periods when one sensor was inactive were neglected.

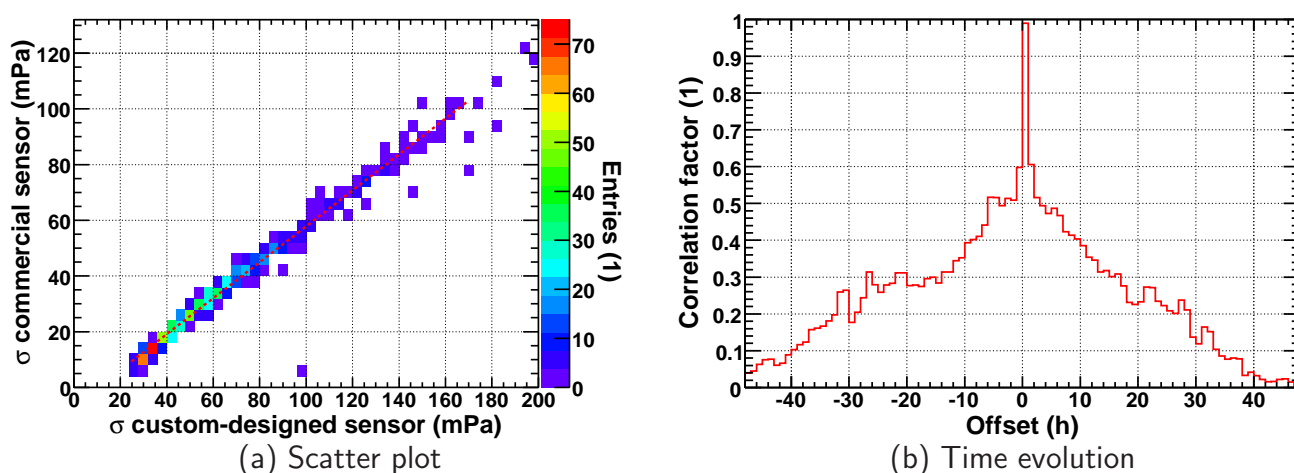


**Figure 12.13:** Scatter plot of the correlation between the noise levels measured by the custom-designed hydrophone LTI105 and the commercial one HTI010 (a) and the time evolution for the correlation factor (b) deduced from (a) in analogy to Fig. 12.12. The colour coding in (a) is a representation of the occurrence of the noise levels (binning width: 4 mPa), the dashed red line represents a linear fit with an axis intercept of  $(-6.7 \pm 0.8)$  mPa and a slope of  $0.65 \pm 0.01$  at a  $\chi^2/\text{ndf}$  of 27/32.

The correlation is well describable by a linear fit (red dotted line in Fig. 12.13(a)), the non-zero intercept is a consequence of the different remaining inherent noise fractions in the ambient noise levels. The non-unity slope is a consequence of the difference in the sensitivities of the sensors. A random correlation can be ruled out as the correlation factor is highly peaked at an offset of 0 h (cf. Fig. 12.13(b)) with a maximum value of 0.99. It can be deduced that the sensors and thus the whole system responds linearly and equally to external stimuli over a long period of time. This linear behaviour of the sensors is expected from laboratory measurements and the confirmation with the ambient noise in the sea shows again the functionality of the AMADEUS system.

This first analysis of the AMADEUS data already shows the potential of the system. However, a lot of effort is still needed to understand all the features observed and make final statements about the major questions in acoustic neutrino detection, like the behaviour of the ambient noise at the ANTARES site and the reconstruction of point sources. One of the major tasks

is the data filtering and systematic analysis of transients, which was not possible within the extent of this work.



# Chapter 13

## Summary and Conclusion

In this work an experimental study towards the acoustic detection of ultra-high energy cosmogenic neutrinos was presented which was conducted at the Erlangen Centre for Astroparticle Physics (ECAP) as part of the activities of the ANTARES Collaboration.

The search for ultra-high energy neutrinos with energies above  $10^{18}$  eV is motivated by the guaranteed flux of such neutrinos generated by cosmic rays via the *Greisen-Zatsepin-Kuzmin effect* as they propagate through the cosmic microwave background. Recent observations of cosmic-ray ground arrays and fluorescence telescopes hint to *Active Galactic Nuclei* (AGNs) as sources of the protons which are assumed to be the major component of cosmic rays at those extreme energies. In the highly energetic surrounding of the AGNs also ultra-high energy neutrinos are expected to be produced which might be detectable with a future large-scale neutrino detector. The detection of cosmogenic neutrinos in this energy range would open a new window to study the highest-energy phenomena in the cosmos and thus provide additional information for the production mechanism from the weak sector of the Standard Model of particle physics.

For the detection of those neutrinos, the optical Cherenkov technique currently used in neutrino telescopes is not suitable, as volumes exceeding  $10 \text{ km}^3$  would have to be instrumented to achieve statistically significant event rates at the predicted low fluxes. With the *acoustic technique* a promising alternative, or complement in a hybrid approach, was introduced for building a future neutrino telescope in water, especially the water of the deep-sea. This technique utilises the effect that a particle cascade originating from a neutrino interaction generates a broad-band acoustic signal of bipolar shape, which propagates through the medium in a disc-like geometry perpendicular to the cascade axis. For the maximum emission strength at 10 kHz, the attenuation length in sea water lies in the order of several kilometres, which allows for a sparsely instrumented detector. The acoustical signal is of low frequency with respect to current electronics which offers the possibility to work with a simple sensor design and read-out electronics. The drawback of the method, however, is the low amplitude of the signals (down to mPa) in a high background of ambient noise and transient signals which places high requirements on the signal processing and data filtering.

An experimental verification of the underlying effect described by the *thermo-acoustic model* was presented. This model ascribes the signal generation to the energy deposition of the cascade

in water, which is thereby heated locally. Due to the fast heating, the affected water volume undergoes an accelerated expansion, causing an acoustic pressure pulse. Due to the almost instantaneous energy deposition within the cylindrical cascade geometry (width in the order of several cm and length in the order of 10 m), the emission perpendicular to the cascade axis is coherent. This effect is responsible for the disc-like geometry of the signal propagation through the surrounding medium. The energy deposition of a cascade in the water was emulated by pulsed proton and laser beams and the recorded signal properties were compared with the expectation from the model and simulation based upon it. The obtained dependencies on the pulse energies, the sensor position and the water temperature were found to be in good agreement with the predictions, as was the signal shape. Especially the observed disappearance of the signal at 4.0 °C, where water has its maximum density, is a clear evidence for a thermo-acoustic generation process.

Based on the thermo-acoustic model, the acoustic signal of a neutrino interaction in sea water and the evolving cascade can be simulated. The peak-to-peak amplitude of the signal can be estimated to 2 mPa per 1 EeV cascade energy at 1 km distance vertical to the cascade axis. The frequency range of interest, for which the main signal components meet a low ambient noise power density in the deep-sea, lies between 1 and 50 kHz and the peak-emission around 10 kHz. Simulations of an acoustic detector, based on the theoretical model, show that a density of as low as 200 *sensor clusters* (a dense array or antenna of several sensors) per cubic-kilometre is sufficient to exploit the full detector efficiency. In these studies the effective volume of a 1 km<sup>3</sup> benchmark simulated detector surpasses its instrumented volume at energies on the order of 10<sup>19</sup> eV; the maximum effective volume reaches values of several thousand cubic-kilometres for even higher energies. The efficiency of such a future detector is ultimately limited by the threshold at which the bipolar neutrino signal can be unambiguously identified in the ambient noise in the sea and the rate of background signals mimicking such a signal. The minimum threshold in these studies, motivated by the expectation for the ambient noise in the deep-sea, was assumed to be 5 mPa per acoustic cluster.

To evaluate the background situation and thus the feasibility of a future acoustic detector for ultra-high energy neutrinos, the *AMADEUS* project in ANTARES was initiated by the ECAP acoustics group. In this project, both the software and hardware infrastructure of the ANTARES neutrino telescope are used to install and read-out 36 acoustic sensors in six local clusters on two *lines* in the deep-sea at depths between 2050 and 2300 m below the surface. Each cluster matches one *storey* of the ANTARES detector with sensor spacings in the order of 1 m. The detector site is located 40 km off the southern coast of France, near the town of Toulon, at a water depth of 2500 m. The *AMADEUS* setup is installed in two phases, where in each case 18 sensors on three storeys are installed on one line of the detector. In the final installation the range of distances between sensors is from below 1 m within one storey up to 340 m between different clusters. At these different length scales, comparable to those needed in a future detector, studies of background behaviour, like correlation length or surface noise attenuation with depth, are possible. Also studies of background transients concerning e.g. rate, pointing accuracy and detectability in the background can be conducted. These transient signals can be caused by anthropogenic and marine sources and by measuring them it is also possible to study the deep-sea acoustical environment.



Two major components had to be developed to include acoustic sensors and their read-out into the ANTARES detector: the sensors themselves and the off-shore data-acquisition hardware. Three types of sensors are installed in AMADEUS, one custom-designed and one commercial *hydrophone* type with sensitive piezo-electrical elements coated in plastics, and the new concept of *Acoustic Modules* with piezo-electrical elements glued to the inside of glass-spheres. The sensors have an average sensitivity of  $-140$  to  $-145$  dB re  $1\text{V}/\mu\text{Pa}$  ( $0.05$  to  $0.1\text{V}/\text{Pa}$ ) with an inherent noise power density of  $-105$  to  $-120$  dB re  $1\text{V}^2/\text{Hz}$  ( $1$  to  $5\mu\text{V}/\sqrt{\text{Hz}}$ ) and are sensitive in the range of  $1$  to  $50$  kHz (up to  $100$  kHz for the Acoustic Modules).

Within the scope of the work presented here, the acoustic data-acquisition hardware in form of the *AcouADC board* has been developed, tested and calibrated. This board filters and amplifies the sensor signals at the storeys in the sea, digitises and formats the data and sends it to a computer cluster at the shore station via the ANTARES data processing chain. For the investigation of the not well-known acoustic properties of the deep-sea, the board has a flexible design. Several parameters in the amplification, filtering and digitisation are adjustable from the on-shore detector control: the gain factor can be varied between  $1$  and  $562$  in  $12$  steps, the digitisation frequency can be chosen between  $125$ ,  $250$  and  $500$  kSamples/s ( $62.5$ ,  $125$  and  $250$  kHz), and two different input ranges for the digitisation can be selected. A programmable processor on the board allows for off-shore data preprocessing. Appropriate band-pass filters suppress the low-frequency components of the ambient noise below  $1$  kHz and the aliasing relevant high-frequency components, mainly caused by the inherent noise of the system. Due to the small input signals, the board was designed to reach an inherent noise of  $-150$  dB re  $1\text{V}^2/\text{Hz}$  ( $0.05\mu\text{V}/\sqrt{\text{Hz}}$ ), at least a factor of  $30$  lower than the sensor inherent noise.

All parameters of the board have been calibrated and were found to be well described by parametrised system transfer functions. The filter response of the board was parametrised in the frequency domain for both amplitude and phase using power functions and the digitisation non-linearities were evaluated using a histogram method and demonstrated to be negligible. The design parameters of the boards were confirmed, in the calibration measurements never a deviation exceeding  $10\%$  was encountered. These deviations can be adjusted in the calibration of the data such that the uncertainties in the individual parameters are on the  $1 - 2\%$  level. Therefore the uncertainties in the calibration of the individual board are insignificant compared to the uncertainties in the sensor calibration. In the same order of magnitude is the spread of parameters between the individual boards and thus an overall calibration set can be used for all  $18$  boards in the AMADEUS setup. From these parametrisations of the system transfer functions, the response of the board to a sensor signal and ambient noise can be fully calculated to a high precision.

Intensive tests showed no significant deviations in performance of the system due to inherent noise, system instabilities or externally induced noise. For example a dynamical range of almost  $60$  dB (factor  $1000$ ) is reached, e.g. at a gain factor of  $10$  signals can be recorded with amplitudes from about  $5$  mPa (being the inherent noise of the sensors) up to  $5$  Pa – equivalent to the acoustic signals of cascades with energies between  $2 \cdot 10^{18}$  and  $2 \cdot 10^{21}$  eV at  $1$  km distance. Frequency distortions produced in the board were found to be insignificant, as well as the crosstalk between the two sensor read-out channels implemented on one board. The DAQ system was proved not to be electro-magnetically vulnerable to high-frequent noise pulses induced from the

outside and found to be operating stably over large times, with variations in the inherent noise level below 1%. With these tests it could be shown that the system, inaccessible within the complex ANTARES data-acquisition system once operated in the sea, does not influence the data quality significantly.

In December 2007 the first phase of the AMADEUS project started to take data in the sea with 18 sensors on the instrumentation line IL07. A first and preliminary analysis of the data recorded in the first month of operation was performed. The system operated stably and took data continuously over the whole period, only one out of the 18 sensors turned out to be defective. Two different hydrophone types were included in that part of the project, and the amplitude distributions of data samples were found to be in good agreement for the sensors of the same type. The noise levels measured with the two sensor types at a given time are linearly correlated with correlation factors of 99% showing the linear and equal response of the sensors to external stimuli. Between the sensor types the recorded noise levels differed by a factor of  $\approx 2$  due to the preliminary calibration used, which is a very satisfying agreement.

Samples of strong transients were analysed and it was confirmed that all sensors respond to them with signals comparable in shape and amplitude. A reconstruction of the direction of sources with individual storeys showed uncertainties below  $2^\circ$ . The system proved to be sensitive to the ambient noise of the deep-sea up to frequencies of at least 30 kHz with a possibility of improvement from better inherent noise treatment. The average noise levels lie in the same order of magnitude as expected from a comprehensive parametrisation of the ambient noise in the sea. This noise is assumed to be primarily produced by the agitation of the sea-surface. The noise levels detected vary in a broad range from  $\approx 5$  mPa to above 200 mPa. The median noise level for 24 days was found to be at  $\approx 20$  mPa (in the frequency range from 1 to 50 kHz) at the one sensor level, with a possible improvement using the data of the six sensors on one storey and by shielding the noise from the surface. The assumed detection threshold of 5 mPa in the simulations of an acoustic detector, mentioned above, seems sensible and reachable. A first hint to coherent emission of noise from the surface was presented, consistent with the correlation factors of 75% found between the recorded noise level and the wind speed at the surface.

The AMADEUS project provides a unique opportunity to study the questions of acoustic neutrino detection in a setup and on a timescale comparable to a future neutrino detector, though much smaller in scale. The operation within a neutrino telescope not only provides the technical infrastructure for continuous operation but also the opportunity to test the potential of a hybrid detection with the optical and acoustical method. On different length scales, from the local cluster with spacings of 1 m to cluster spacings of almost 350 m, the behaviour of ambient noise and background transients can be studied, and the major questions of acoustic particle detector can be addressed. Sensor studies can be done with three different sensor types to find a suitable design for the acoustic detection. With the full data sample accessible anytime at the shore, signal processing techniques and data filters for an efficient identification of signals in the background can be studied within wide amplitude and frequency ranges.

# Kapitel 14

## Zusammenfassung

Im Rahmen der vorgestellten Arbeit wurde eine experimentelle Studie zur *akustischen Detektion ultra-hochenergetischer Neutrinos aus dem Kosmos* durchgeführt. Diese Studie wurde als Teil der Aktivitäten der ANTARES Gruppe am Erlangen Centre for Astroparticle Physics (ECAP) erarbeitet.

In der Astroteilchenphysik werden Elementarteilchen astronomischen Ursprungs untersucht (z.B. *Kosmische Strahlung, Gammastrahlung* und *Neutrinos*). Dazu werden Nachweismethoden benutzt, die in der Teilchenphysik entwickelt wurden, z.B. für Detektoren an Teilchenbeschleunigern. Aber auch neue Techniken werden entwickelt, um die notwendige Nachweissensitivität für die kosmischen Teilchen zu erreichen.

Die Detektion von Neutrinos mit Energien jenseits von  $10^{18}$  eV würde ein neues Fenster zur Untersuchung der höchstenergetischen Phänomene im Kosmos eröffnen. Die physikalische Relevanz kann unter anderem mit dem garantierten Neutrinofluss begründet werden, der bei der Propagation Kosmischer Strahlung extremer Energien durch den Mikrowellenhintergrund mittels des *Greisen-Zatsepin-Kuzmin Effekt* [6,7] entsteht. Neuere Veröffentlichungen auf diesem Gebiet durch das Pierre-Auger Projekt [4,9] und das HiRes Experiment [10] deuten darauf hin, dass Protonen, die aus *Aktiven Galaktischen Kernen (AGNs)* stammen, die Hauptkomponente der Kosmischen Strahlen bei diesen extremen Energien ( $\geq 10^{19}$  eV) bilden. In der hochenergetischen Umgebung von AGNs wird auch die Produktion von ultra-hochenergetischen Neutrinos in Fluss-Regionen vorhergesagt, die mit zukünftigen großvolumigen Detektoren nachweisbar sein könnten.

Zum Nachweis dieser Neutrinos ist die optische Cherenkov-Technik, die gegenwärtig in (optischen) Neutrino-Teleskopen genutzt wird, nicht oder nur eingeschränkt geeignet. Es müssen Volumina von (weit) über  $10 \text{ km}^3$  instrumentiert werden, um bei den vorhergesagten niedrigen Flüssen statistisch signifikante Ereignisraten zu erreichen. Die vorgestellte akustische Technik bietet eine vielversprechende Alternative bzw. Ergänzung für den Bau zukünftiger Neutrino-Teleskope, insbesondere auch im Wasser der Tiefsee. Diese Nachweismethode nutzt die Tatsache, dass ein Teilchenschauer, der in einer Neutrino-Wechselwirkung im Wasser entsteht, ein breitbandiges akustisches Signal bipolarer Form erzeugt. Dieses Signal dehnt sich im Medium mit einer scheibenförmigen Geometrie senkrecht zur Schauerachse aus. Die Abschwächlänge für Schall im Meerwasser liegt im Bereich mehrerer Kilometer für das Maximum der Emission

bei ca. 10 kHz und ermöglicht damit den Bau eines dünn instrumentierten Detektors. Im Vergleich dazu liegt die Abschwächlänge für das bei der optischen Methode genutzte Spektrum des Cherenkov-Lichts bei etwa 100 m. Das im Bezug auf elektronische Weiterverarbeitung niederfrequente akustische Signal erlaubt zudem einen relativ einfachen Sensoraufbau und eine einfache Ausleseelektronik. Diese Vorteile müssen jedoch durch die anspruchsvolle Suche nach einem schwachen Signal (mit Amplituden im mPa Bereich) in einem breitgefächerten Untergrund von Umgebungsrauschen und transienten Signalen erkauft werden. Diese Voraussetzungen stellen hohe Ansprüche an die Signalverarbeitung und Datenfilterung und setzen insbesondere ein gutes Verständnis der Untergrundbedingungen in der Tiefsee voraus.

Eine verfeinerte Analyse der experimentellen Überprüfung des zugrundeliegenden Effekts [18–20], beschrieben durch das *thermoakustische Modell* [21–23], wurde vorgestellt. Dieses Modell führt die Signalerzeugung auf die Energiedeposition des bei einer Neutrino-Interaktion entstehenden Schauers im Wasser zurück, welches dadurch lokal erwärmt wird. Durch die annähernd instantane Erwärmung dehnt sich das kommt es zu einer beschleunigten Expansion des betroffenen Wasservolumens, was zu einem akustischen Druckpuls führt. Durch die langgestreckte zylindrische Schauerform und die schnelle Energiedeposition erfolgt die Schallemission senkrecht zur Schauerachse kohärent; die Schauerform ist damit auch verantwortlich für die scheibenförmige Geometrie der Schallausbreitung im umgebenden Medium. Zur Überprüfung des Modells im Labor wurde die Energiedeposition eines Schauers in Wasser durch gepulste Protonen- und Laserstrahlen nachgestellt. Die Eigenschaften der mittels akustischer Sensoren (*Hydrophonen*) aufgezeichneten Signale stimmen gut mit den Erwartungen des Modells und darauf basierenden Simulationen überein. Abhängigkeiten der Signalamplitude, Signallänge und Signalform von den betrachteten Pulsenergien, der Sensorposition und der Wassertemperatur wurden untersucht und in allen Fällen die Vorhersagen des Modells bestätigt. Insbesondere der Verlauf der Signalamplitude mit der Wassertemperatur, die wie vorhergesagt dem Grüneisen-Parameter folgt und das Verschwinden des Signals bei 4.0 °C sind klare Hinweise auf einen thermoakustischen Signalerzeugungsprozess (siehe Abb. 14.1).

Aufbauend auf dem thermoakustischen Modell kann das akustische Signal eines wechselwirkenden Neutrinos bzw. dasjenige des dabei entstehenden Schauers simuliert werden [36]. Die resultierende Signalamplitude vom Maximum zum Minimum des etwa 15  $\mu\text{s}$  langen Signals kann abgeschätzt werden zu  $\approx 2 \text{ mPa}$  pro 1 EeV Schauerenergie bei einem vertikalen Abstand von 1 km zur Schauerachse (siehe Abb. 14.2(a)). Die Amplitude steigt linear mit der Schauerenergie und fällt wie  $1/\sqrt{r}$  bzw.  $1/r$  im Nah- bzw. Fernfeld mit dem Abstand  $r$  zur Quelle ab. Der für akustische Neutrinodetektion relevante Frequenzbereich, in dem der Hauptanteil auf eine niedrige Leistungsdichte des Umgebungsrauschens in der Tiefsee trifft, liegt zwischen 1 und 50 kHz und die maximale Emission um 10 kHz (siehe Abb. 14.2(b)).

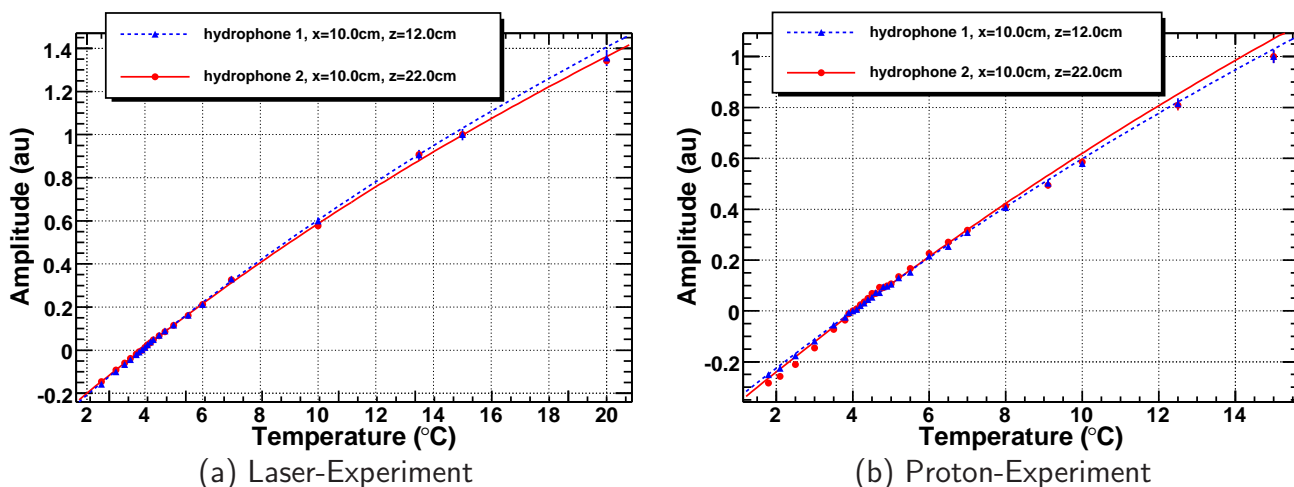


**Abbildung 14.1:** Temperaturabhängigkeit der Signalamplituden bei Laser- (a) und Protonen-Experimenten (b). Zur besseren Vergleichbarkeit wurden die Amplituden so skaliert, dass sie bei 15.0°C auf 1 normiert sind. Die eingezeichneten Linien zeigen den Fit der Modellerwartung.

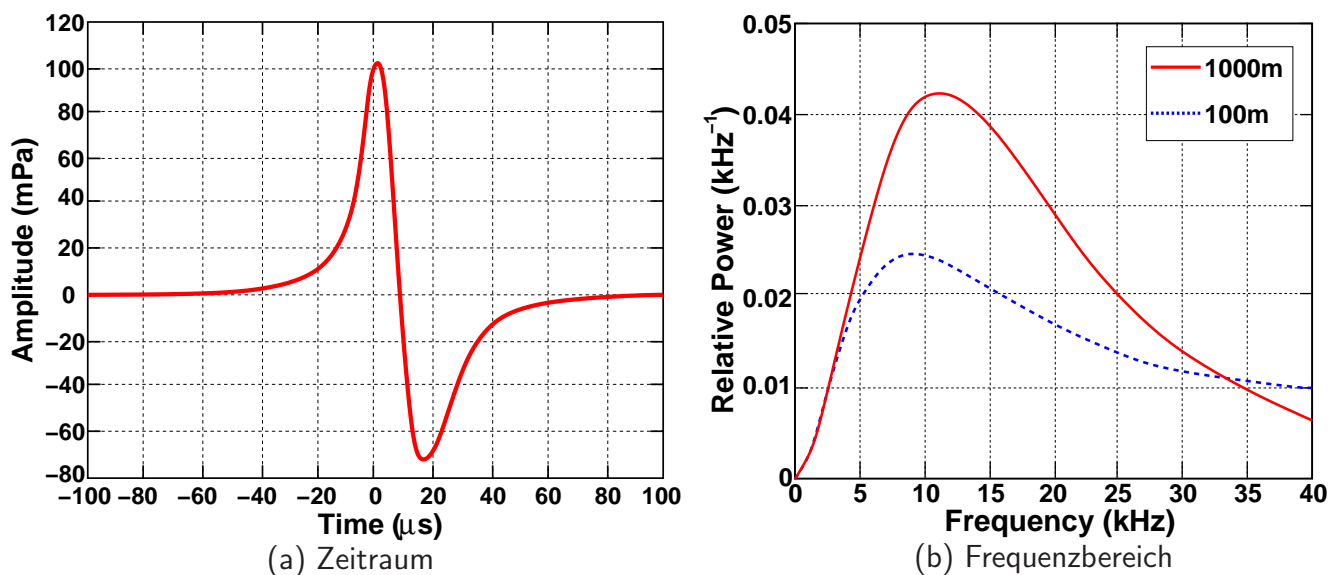


**Abbildung 14.2:** Simuliertes akustisches Signal eines  $10^{20}$  eV Teilchenschauers bei einem Abstand von 1 km zum Schauerzentrum (a). Im Frequenzbereich (b) ist das relative Leistungsspektrum des Signals für verschiedene Abstände zur Quelle aufgetragen (Signalenergie normiert auf 1). Die Abbildungen basieren auf [36].

Simulationen akustischer Detektoren zeigen [15], dass mit geringen Sensordichten von 200 *Sensorguppen* (einer dichten Anordnung oder Antenne bestehend aus mehreren Einzelsensoren) pro Kubikkilometer fast die gesamte Detektoreffizienz ausgeschöpft werden kann. Für einen optischen Detektor sind dazu Sensordichten in der Größenordnung von mehreren 1000 Sensoren

notwendig. Das effektive Volumen eines  $1 \text{ km}^3$  großen akustischen Bezugsdetektors beispielsweise erreichte in diesen Studien sein instrumentiertes Volumen bei Energien in der Größenordnung von  $10^{19} \text{ eV}$ ; das maximale effektive Volumen erreichte einige tausend Kubikkilometer. Die Nachweiseffizienz eines möglichen akustischen Neutrinodetektors ist letztlich begrenzt durch zwei Faktoren: den Schwellenwert, oberhalb dessen das bipolare Neutrinosignal eindeutig im Umgebungsrauschen nachgewiesen werden kann, und die Rate von Untergrundsignalen mit einer von Neutrinoereignissen nicht unterscheidbaren Signatur. Der minimale Schwellenwert wurde in den Studien zu  $5 \text{ mPa}$  in einer Sensorgruppe angenommen, motiviert durch die Erwartung für das Umgebungsrauschen in der Tiefsee. Die Rate von Untergrundsignalen kann nur durch experimentelle Studien bestimmt werden.

Um die Untergrundsituation in der Tiefsee und damit die Machbarkeit eines zukünftigen akustischen Neutrinodetektors zu evaluieren, wurde am ECAP das Projekt *AMADEUS* initiiert. In diesem Projekt wird die Software- und Hardware-Infrastruktur des optischen Neutrinoteleskops ANTARES [56] genutzt, um 36 akustische Sensoren auf zwei sogenannten *Lines* (vertikalen Strukturen des ANTARES-Detektors) in der Tiefsee zu installieren und auszulesen (siehe Abb. 14.3).

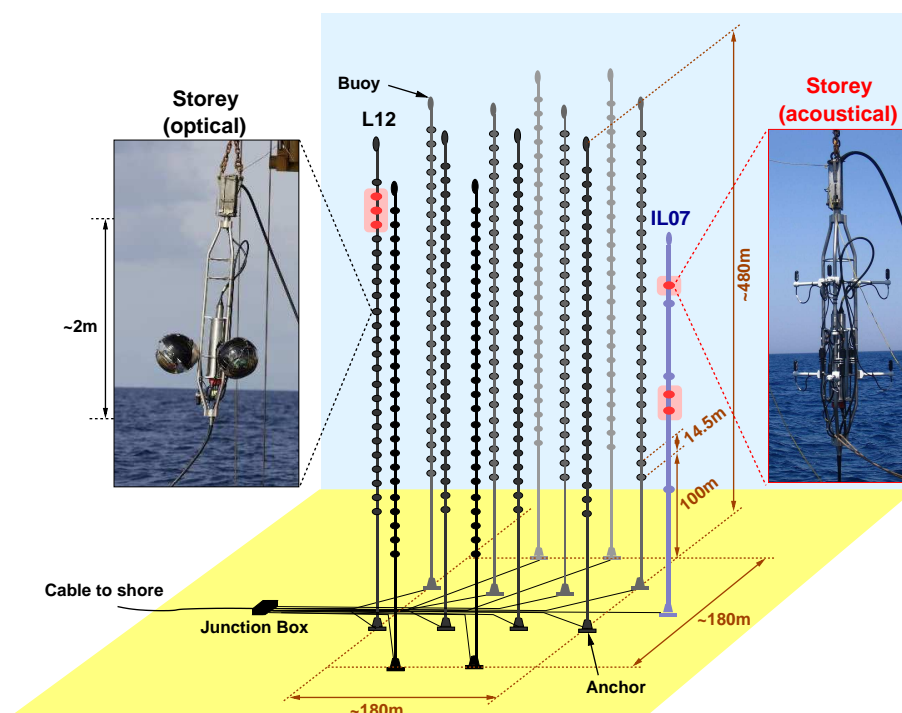


**Abbildung 14.3:** Schematische Darstellung des ANTARES-Detektors mit seiner akustischen Erweiterung AMADEUS (in rot). Der Detektor besteht aus 12 vertikalen *Lines* mit optischen Sensoren (schwarz) und einer Line zur Untersuchung der Tiefseenumgebung (blau). Die *Stockwerke* (*storeys*) sind durch Kreise angedeutet und jeweils ein Beispiel eines optischen und eines akustischen Stockwerks ist im Bild gezeigt.

Der Detektor befindet sich 40 km vor der Küste von Südfrankreich in der Nähe der Stadt Toulon, in einer Meerestiefe von 2500 m. Die akustischen Stockwerke befinden sich in Wassertiefen zwischen 2050 und 2300 m. Die akustischen Sensoren sind in 6 lokalen Gruppen mit Sensorabständen um 1 m angeordnet, dabei entspricht jede Sensorgruppe einem ANTARES-Stockwerk, auf dem sich sechs Sensoren und Weiterverarbeitungselektronik für die Daten befinden. Das AMADEUS-Setup wird in zwei Phasen aufgebaut, in denen jeweils 18 Sensoren auf 3 Stockwerken auf einer Line des Detektors (L12 und IL07) installiert werden. Im finalen Aufbau liegen die Abstände zwischen den Sensoren im Bereich von 1 m innerhalb der Stockwerke und bis zu 340 m zwischen Stockwerken auf den zwei Lines. Dieser Aufbau ist zur Untersuchung der Methode der akustischen Neutrinodetektion bisher einzigartig. Auf Längenskalen, die vergleichbar sind mit den in einem zukünftigen Detektor benötigten, können Studien zum Untergrundverhalten durchgeführt werden. Zu diesen Studien gehören unter anderem die Bestimmung von Korrelationslängen im Untergrundrauschen und von Untergrundsignalen oder die Vermessung der Abschwächung von Oberflächenrauschen mit der Tiefe. Vom Oberflächenrauschen, das durch die Agitation der Meeresoberfläche erzeugt wird, wird angenommen, dass es den Großteil des Umgebungsrauschen ausmacht. Aber auch Studien der Untergrundsignale bezüglich ihrer Rate, der Richtungsgenauigkeit der Quellenbestimmung und der Nachweisbarkeit im Umgebungsrauschen werden durchgeführt. Diese transienten Signale können von anthropogenen und marinen Quellen erzeugt werden; damit ist auch eine Untersuchung der unterseeischen akustischen Umgebung mit AMADEUS möglich.

Um akustische Sensoren und deren Auslese in den ANTARES Detektor integrieren zu können mussten zwei wesentliche Komponenten entwickelt werden: die Sensoren an sich und die im Stockwerk befindliche Datennahmehardware. Drei Typen von Sensoren sind im AMADEUS-Aufbau integriert: Jeweils ein speziell entwickelter und ein kommerziell erhältlicher *Hydrophon*-Typ, mit sensitiven piezo-elektrischen Elementen, die in Kunststoff eingehüllt sind, und das neuartige Konzept eines *akustischen Moduls* [48,80]. In Letzterem werden die Piezo-Elemente an die Innenseite von Glassphären angeklebt. Die Sensoren haben eine mittlere Sensitivität von  $-140$  bis  $-145$  dB re  $1\text{V}/\mu\text{Pa}$  ( $0.05$  bis  $0.1\text{V}/\text{Pa}$ ) bei einem Eigenrauschen von  $-105$  bis  $-120$  dB re  $1\text{V}^2/\text{Hz}$  ( $1$  bis  $5\mu\text{V}^2/\text{Hz}$ ) und sind sensitiv im Frequenzbereich von  $1$  bis  $50$  kHz (bis  $100$  kHz bei den akustischen Modulen).

Im Zuge der vorliegenden Arbeit wurde die Datennahmehardware in Form der sogenannten *AcouADC-Karte* entwickelt, getestet und kalibriert. Diese Karte filtert und verstärkt die Signale von jeweils zwei Sensoren direkt auf dem Stockwerk, d.h. noch im Meer. Anschließend werden die Signale digitalisiert und formatiert über die ANTARES Datennahmekette zu einem Computer-Cluster an Land gesendet, wo die Daten weiterverarbeitet werden. Da die akustischen Eigenschaften der Tiefsee nicht gut bekannt sind, wurde das Design der Karte flexibel gestaltet, und mehrere Parameter in der Verstärkung, Filterung und Digitalisierung sind von der Detektorkontrolle an der Küste aus einstellbar: Verstärkungsfaktoren zwischen  $1$  und  $562$  können in  $12$  Schritten gewählt werden, die Digitalisierungsfrequenz liegt bei  $125$ ,  $250$  oder  $500$  kSamples/s ( $62.5$ ,  $125$  und  $250$  kHz) und zwei verschiedene Eingangsspannungsbereiche der Digitalisierung können vorgegeben werden. Ein programmierbarer Prozessor auf der Karte erlaubt eine Datenvorverarbeitung im Meer. Passende Bandpass-Filter unterdrücken sowohl die irrelevanten niederfrequenten Anteile des Umgebungsrauschens unter  $1$  kHz, als auch die für

das Aliasing relevanten hochfrequenten Komponenten, die primär durch das Eigenrauschen des Systems verursacht werden. Aufgrund der geringen Eingangsamplituden wurde die Karte auf ein Eigenrauschen von  $-150 \text{ dB re } 1 \text{ V}^2/\text{Hz}$  ( $0.05 \mu\text{V}/\sqrt{\text{Hz}}$ ) ausgelegt. Letzteres ist damit mehr als einen Faktor 30 kleiner als das der Sensoren.

Alle Parameter der AcouADC-Karte wurden kalibriert und sind durch parametrisierte System-Transferfunktionen gut beschreibbar. Die Amplituden- und Phasenantwort des Filters wurde im Frequenzbereich durch rationale Funktionen und Potenzfunktionen parametrisiert (siehe Abb. 14.4). Die Nichtlinearitäten der Digitalisierungen wurden ausgewertet und stellten sich als vernachlässigbar heraus. Die Designparameter konnten sehr genau verifiziert werden, die geringen vorhandenen Abweichungen können durch Kalibration der Daten ausgeglichen werden, so dass die Unsicherheiten in den einzelnen Parametern bei  $1 - 2\%$  liegen. Damit sind die Unsicherheiten in der Kartenkalibration vernachlässigbar gegenüber denjenigen der Sensorkalibration. Die Parameter der einzelnen Karten variieren ebenso im Prozentbereich, weswegen ein Satz von Parametern für alle 18 Karten des AMADEUS-Aufbaus verwendet werden kann. Ausgehend von den ermittelten Transferfunktionen kann die Antwort der Karten auf transiente Signale oder das Umgebungsrauschen vollständig mit hoher Präzision berechnet werden.

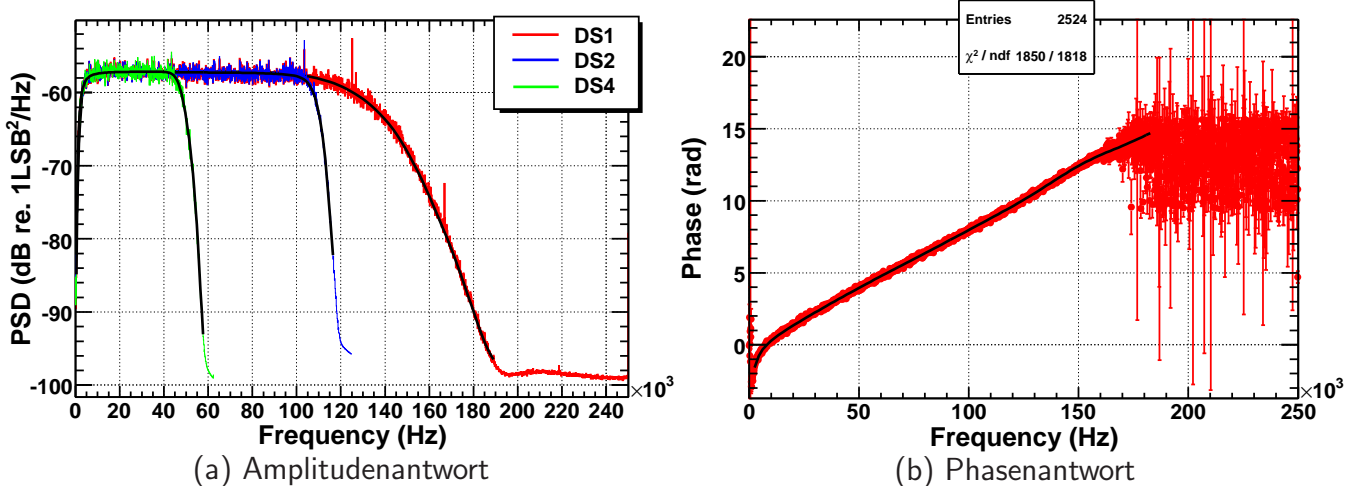


**Abbildung 14.4:** Filterantwort der AcouADC-Karte auf externe Signale mit angepasster Parametrisierung der Transferfunktion (schwarze Linie). Die Amplitudenantwort (a) wird für die drei möglichen Digitalisierungsfrequenzen gezeigt (DS1  $\hat{=}$  250 KHz, DS2  $\hat{=}$  125 KHz und DS4  $\hat{=}$  62.5 kHz), die Phasenantwort (b) ist für DS1 dargestellt.

Intensive Tests des Systems zeigten keine signifikanten Einschränkungen der Systemleistung durch Eigenrauschen, Instabilitäten oder durch von extern eingekoppeltes Rauschen, und eine Leistungsfähigkeit des Systems, die die Erwartungen und Designziele erfüllt. Zum Beispiel wird ein dynamischer Bereich von 60 dB (Faktor 1000) erreicht. Somit können beispielsweise bei einem Verstärkungsfaktor von 10 Signale mit Amplituden von 5 mPa – entsprechend dem Eigenrauschen der Sensoren – bis 5 Pa aufgezeichnet werden – äquivalent akustischer Signale



von Schauern mit Energien zwischen  $2 \cdot 10^{18}$  und  $2 \cdot 10^{21}$  eV bei 1 km Abstand. Verzerrungen der Signale durch die Karte sind nicht signifikant, ebensowenig wie Nebensignaleffekte zwischen den zwei Sensorkanälen auf einer Karte. Das Datennahmesystem wurde erfolgreich auf elektromagnetische Kompatibilität auch bei extremen Bedingungen getestet und ist damit nicht durch hochfrequente Störquellen von außen angreifbar. Es wurde über lange Zeiträume stabil betrieben, mit Variationen im Eigenrauschniveau unter 1%. Mit diesen Tests konnte gezeigt werden, dass das System stabil und ohne die Datenqualität zu beeinflussen agiert, während es von außen unerreichbar innerhalb des komplexen ANTARES Datennahmesystems über Jahre hinweg betrieben wird.

Im Dezember 2007 begann das AMADEUS-Projekt in seiner ersten Phase die Datennahme in der Tiefsee mit 18 Hydrophonen. Eine erste, vorläufige Analyse der im ersten Monat aufgezeichneten Daten wurde durchgeführt. Es konnte bestätigt werden, dass sich das System auch im Meer stabil verhält und eine kontinuierliche Datennahme über die gesamte Zeitspanne möglich war. Nur einer der 18 Sensoren zeigte sich fehlerhaft. Die Amplitudenverteilungen von Stichproben der Daten ist zwischen Sensoren gleichen Typs sehr ähnlich. Das zu gleichen Zeiten mit Sensoren verschiedenen Typs aufgenommene Rauschniveau ist linear korreliert mit einem Korrelationsfaktor von 99% und zeigt das lineare und vergleichbare Ansprechverhalten der Sensoren auf externe Stimuli. Die Rauschniveaus zwischen den Sensortypen unterscheiden sich nur um einen Faktor 2, was auf Unsicherheiten in der vorläufigen Sensorkalibration zurückzuführen ist. Eine Auswahl an starken transienten Signalen wurden betrachtet. Diese Signale konnten in den Daten aller Sensoren mit vergleichbarer Ausprägung und Amplitude nachgewiesen werden. Eine Richtungsrekonstruktion von Quellen mit einzelnen Stockwerken ergab Unsicherheiten von weniger als  $2^\circ$  und zeigte damit eine der Möglichkeiten des Konzepts der Sensorgruppen auf: lokale Vorrekonstruktion von Ereignissen und damit ein potentieller Geschwindigkeitsgewinn in der Datenverarbeitung.

Das System stellte sich als sensitiv gegenüber dem Umgebungsrauschen bis zu Frequenzen von mindestens 30 kHz heraus, mit der Möglichkeiten zur Verbesserung mit einer verfeinerten Eigenrauschbehandlung. Die Umgebungsrauschniveaus variierten über den betrachteten Zeitraum stark im Bereich von  $\approx 5$  mPa bis über 200 mPa. Das mittlere gemessene Umgebungsrauschniveau liegt im erwarteten Bereich einer Parametrisierung des oberflächengenerierten Rauschens. Im Median war das Rauschniveau der Einzelsensoren in dem betrachteten Zeitraum  $\approx 20$  mPa (im Frequenzbereich von 1 bis 50 kHz). Dieser Wert kann durch Verwendung der Daten der Sensorgruppen und durch Abschirmung des Oberflächenrauschens potentiell noch weiter gesenkt werden. Damit stellt sich der angenommene Detektionsschwellenwert von 5 mPa als vernünftig und erreichbar dar. Ein erster Hinweis auf kohärente Emission des Rauschens von der Oberfläche konnte gefunden werden, konsistent mit einem Korrelationsfaktor von 75% zwischen den aufgezeichneten Rauschniveaus und der Geschwindigkeit des an der Oberfläche herrschenden Windes (siehe Abb. 14.5).

Das Setup von AMADEUS ist im Aufbau und im angelegten Zeitrahmen vergleichbar mit einem zukünftigen Neutrinodetektor, wenn auch bedeutend kleiner. Der erfolgreiche Betrieb innerhalb eines bestehenden Neutrinoteleskops bietet nicht nur die Infrastruktur für einen kontinuierlichen Betrieb über mehrere Jahre, sondern ermöglicht auch Studien zum hybriden Nachweis von Neutrinos mit optischer und akustischer Nachweismethode. Auf unterschiedlichen Längenskalen,

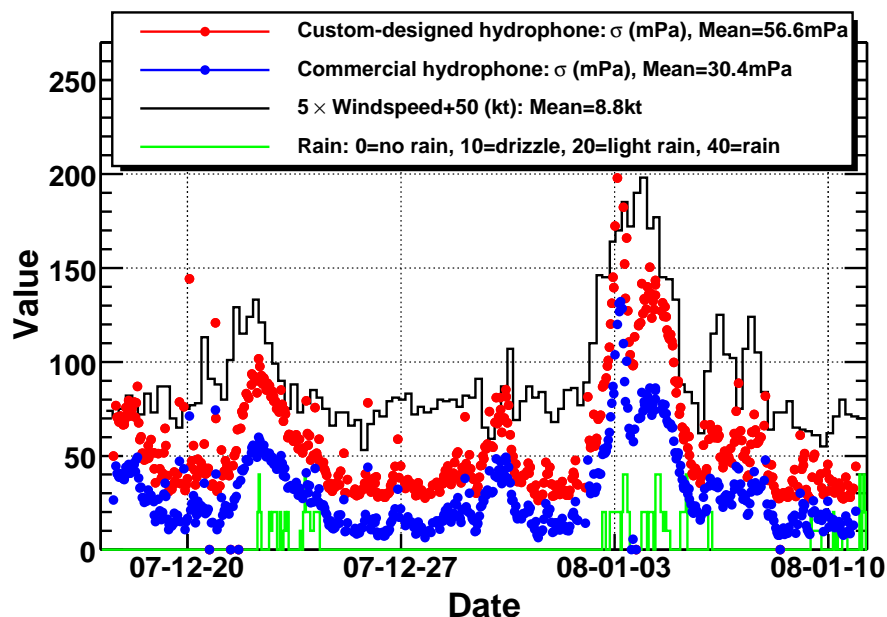


**Abbildung 14.5:** Zeitverlauf des Umgebungsrauschens und der Wetterbedingungen. Das gezeigte Rauschen wurde mit je einem Hydrophon der zwei verwendeten Typen aufgezeichnet, die Unterschiede in den Rauschniveaus zwischen den Sensoren sind kalibrationsbedingt. Die Wetterbedingungen an der Meeresoberfläche werden durch die Messung der Windgeschwindigkeit und Regenstärke in einer Wetterstation 30 km nördlich des Detektorstandortes wiedergegeben. Die Auftragung der Werte und die Mittelwerte sind in der Legende beschrieben.

von 1 m Sensorabstand innerhalb der Stockwerke bis zu Gruppenabständen von 340 m, kann das Verhalten des Umgebungsrauschens und der Untergrundsignale untersucht werden. Sensorstudien können mit drei verschiedenen Typen durchgeführt werden, um das geeignetste Design zu eruieren. Mit dem vollen Datensatz, der jederzeit an der Küste zur Verfügung steht, können Signalverarbeitungstechniken und Datenfilter zum effektiven Signalnachweis im Untergrund in einem großen Amplituden- und Frequenzbereich studiert werden.

Das AMADEUS-Projekt bietet somit eine einzigartige Möglichkeit, die Fragen, die sich im Rahmen der akustischen Neutrinodetektion stellen, zu untersuchen und die Machbarkeit eines zukünftigen großvolumigen Neutrinodetektors in einer experimentellen Studie zu überprüfen.

# Appendix A

## Distribution of Gain Factors

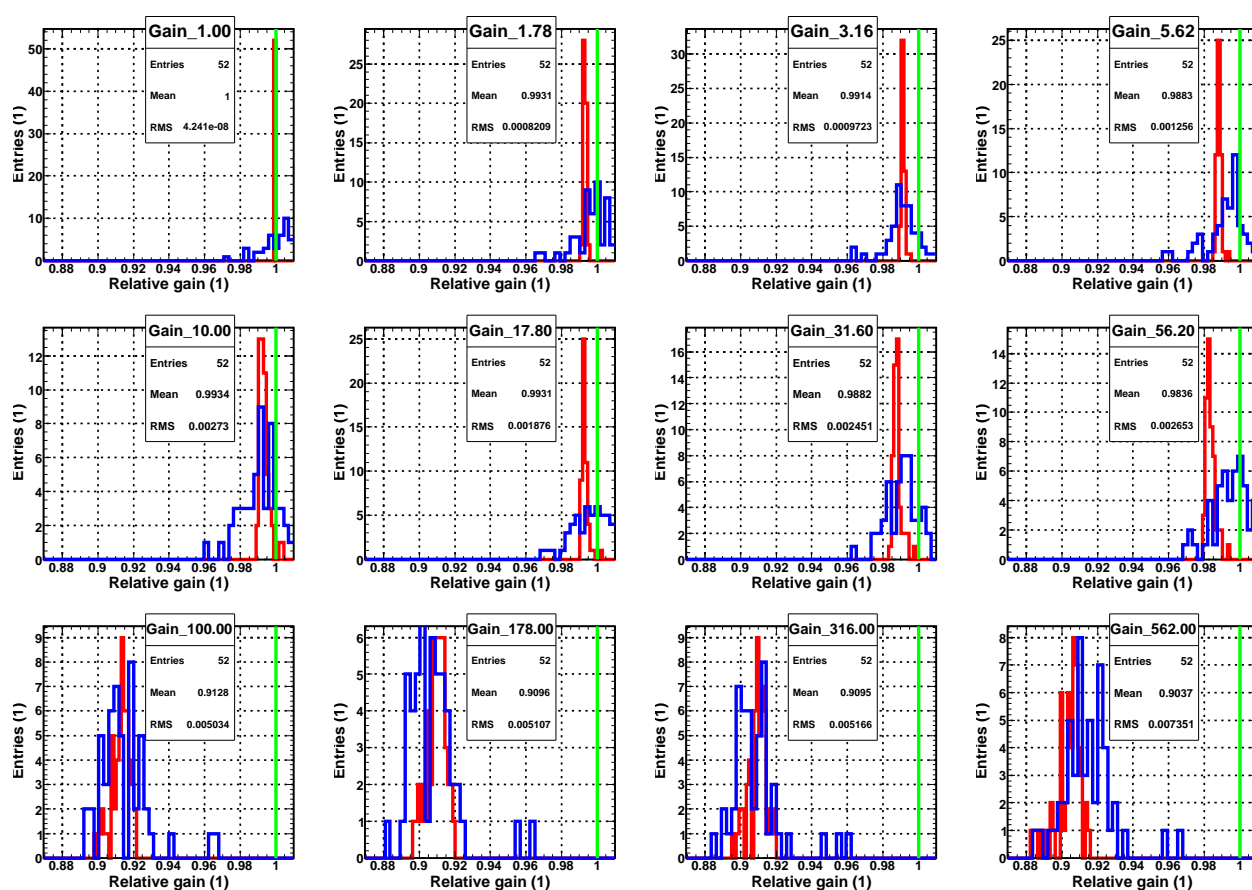


**Figure A.1:** Distributions of the relative gains (measured gain divided by nominal one) for each calibrated sensor channel, separately for each setting from 1.00 to 562 (given in the legend). The gain is calculated from data recorded with the AcouADC boards (red) and data measured with an oscilloscope (blue) as described in Sec. 8.3. The optimum is shown as a green vertical line at a relative gain of 1.



# List of Figures

2.1	UHE Cosmic ray spectra . . . . .	6
2.2	Sky map of cosmic rays . . . . .	8
2.3	Cosmic neutrino flux predictions . . . . .	9
3.1	Exemplary signals of proton and laser experiment . . . . .	13
3.2	Signal amplitude dependencies on sensor position and pulse energy . . . . .	15
3.3	Temperature dependence of signal amplitudes of proton and laser experiment . . . . .	16
4.1	Simulated signal of a UHE cascade . . . . .	18
4.2	Signal Directionality and Attenuation . . . . .	19
4.3	Ambient noise spectra . . . . .	22
4.4	Simulated effective volumes of an acoustic detector . . . . .	24
5.1	Location of the ANTARES detector . . . . .	30
5.2	Schematic of the ANTARES detector . . . . .	31
5.3	ANTARES off-shore DAQ hardware, schematic and photograph . . . . .	34
5.4	The AMADEUS-0 system . . . . .	37
5.5	AMADEUS-0 data: histogram of amplitudes and noise spectra . . . . .	38
6.1	AMADEUS Setup: Schematic and Photograph of Storeys . . . . .	40
6.2	Photographs of acoustic sensors . . . . .	41
6.3	Overall sensitivity of AMADEUS hydrophones . . . . .	42
6.4	Directional sensitivity of a hydrophone . . . . .	43
6.5	Response of a hydrophone to a bipolar signal . . . . .	43
6.6	Photograph of LCM for acoustic storeys . . . . .	45
6.7	AMADEUS off-shore DAQ hardware, schematic and photograph . . . . .	46
7.1	Schematic of the calibration setup for the AcouADC boards . . . . .	54
7.2	Signal of a $\delta$ -pulse used in the board calibration . . . . .	55
7.3	Distribution of gaussian white noise used in the board calibration . . . . .	56
7.4	Signal of sine waveform used in the board calibration . . . . .	57
8.1	Histograms of sine waveform in ADC calibration . . . . .	61
8.2	Average ADC transfer curve . . . . .	61

8.3	Average INL and DNL histograms of ADC transfer curve . . . . .	62
8.4	Exemplary frequency response of the filter with fit . . . . .	66
8.5	Residuals of the filter transfer function fit . . . . .	67
8.6	Measured distribution of gain factors at setting 1.00 . . . . .	68
8.7	Averaged measured gains for all settings . . . . .	69
9.1	PSD of sine waveform for evaluation of SFDR . . . . .	72
9.2	SINAD and SFDR Distributions . . . . .	72
9.3	Inherent noise and channel crosstalk for different gain settings . . . . .	74
9.4	Spectral features of inherent noise and crosstalk . . . . .	75
9.5	Channel crosstalk for a sine waveform . . . . .	75
9.6	Setup for EMV tests . . . . .	76
9.7	Signal amplitudes measured in EMV tests . . . . .	77
9.8	Frequency spectra measured in EMV tests . . . . .	78
9.9	Sine waveform with fit . . . . .	79
9.10	Mean and $\sigma$ of inherent noise amplitude distributions . . . . .	80
9.11	System response to a bipolar pulse . . . . .	81
9.12	System response to gaussian noise . . . . .	82
10.1	Mean and $\sigma$ of sensor self-noise amplitude distributions . . . . .	86
10.2	Amplitude distributions of hydrophone inherent noise . . . . .	87
10.3	Equivalent noise level of the sensors . . . . .	88
10.4	Power spectrum density of the sensor intrinsic noise . . . . .	89
11.1	Amplitude distributions of sea data for different gains . . . . .	92
11.2	Typical amplitude distributions of sea data . . . . .	93
11.3	Typical power spectra of sea data . . . . .	94
11.4	Mean of sea-data for each sensor . . . . .	95
11.5	$\sigma$ of sea-data for each sensor . . . . .	96
12.1	Signal of pingers of the acoustic positioning signals . . . . .	98
12.2	Amplitude distributions for pinger signals . . . . .	99
12.3	Spectra and spectrograph of acoustic positioning signals . . . . .	100
12.4	Signal and result of a beam-forming algorithm for a exemplary transient . . . . .	101
12.5	Scatter plot of recorded noise power spectra . . . . .	102
12.6	Standard deviation of recorded noise power spectra . . . . .	103
12.7	Comparison of measured ambient noise with predictions . . . . .	104
12.8	Correlation of sensor data for a high sea-state . . . . .	105
12.9	Distribution of ambient noise levels and wind speed . . . . .	107
12.10	Time evolution of ambient noise level and weather conditions . . . . .	108
12.11	Scatter plot of correlation between ambient noise level and wind speed . . . . .	109
12.12	Correlation factor between noise level and wind speed . . . . .	109
12.13	Correlation between ambient noise level of two sensors . . . . .	110

---

14.1	Temperaturabhängigkeit der Signalamplituden bei Laser und Protonen Experimenten	119
14.2	Simuliertes akustisches Signal eines Teilchenschauers . . . . .	119
14.3	Schematische Darstellung des ANTARES Detektors . . . . .	120
14.4	Filterantwort der AcouADC-Karte auf externe Signale . . . . .	122
14.5	Zeitverlauf des Umgebungsrauschens und der Wetterbedingungen . . . . .	124
A.1	Distributions of the gains for each AcouADC channel . . . . .	125





# Bibliography

- [1] V.F. Hess, *Durchdringende Strahlung bei sieben Freiballonfahrten*, Phys. Zeitschr. **XIII** (1912) p.1084
- [2] K. Koyama et al., *Evidence for shock acceleration of high-energy electrons in the supernova remnant SN1006*, Nature **378** (1995) p. 255
- [3] F. Aharonian et al., *High-energy particle acceleration in the shell of a supernova remnant*, Nature **432** (2004) p. 75, arXiv:astro-ph/0411533v1
- [4] The Pierre Auger Collaboration, *Correlation of the highest energy cosmic rays with nearby extragalactic objects*, Science **318** (2007) p. 939, arXiv:astro-ph/0711.2256v1
- [5] J.W. Cronin, *The highest-energy cosmic rays*, arXiv:astro-ph/0402487v1 (2004)
- [6] K. Greisen, *End to the cosmic ray spectrum?*, Phys. Rev. Lett. **16** (1966) p. 748
- [7] G.T. Zatsepin and V.A. Kuz'min, *Upper limit of the spectrum of cosmic rays*, JETP Lett. **4** (1966) p. 78, *Ž. Èksp. Teor. Fiz.* (1966) 114
- [8] W.-M. Yao, et al., *Review of Particle Physics*, J. Phys. **G 33** (2006) p. 1
- [9] T. Yamamoto et al., *The UHECR spectrum measured at the Pierre Auger Observatory and its astrophysical implications*, in *Proceedings of the 30th International Cosmic Ray Conference, Merida*, (2007), arXiv:astro-ph/0707.2638v3
- [10] R.U. Abbasi et al., *Observation of the GZK Cutoff by the HiRes Experiment*, RU-PNA-002 (2007), arXiv:astro-ph/0703099
- [11] M. Takeda et al., *Energy determination in the Akeno Giant Air Shower Array experiment*, Astropart. Phys. **19** (2003) p. 447
- [12] T.K. Gaisser, *TeV Particle Astrophysics II: Summary comments*, in *Proceedings of the TeV Particle Astrophysics II Workshop*, ed. F. Halzen et al., J. Phys. Conf. Ser. **60** (2007) p. 72
- [13] M.S. Longair, *High Energy Astrophysics, Vol. 2* (Cambridge University Press, Cambridge, second edition, 1994)

- [14] C. Grupen, *Astroparticle Physics* (Springer Verlag, Berlin Heidelberg, 2005)
- [15] T. Karg, *Detection of ultra high energy neutrinos with an underwater very large volume array of acoustic sensors: A simulation study*, Doctoral Thesis, Univ. Erlangen-Nürnberg, (2006, FAU-PI4-DISS-06-002), arXiv:astro-ph/0608312
- [16] R. Nahnauer and S. Böser (Eds.), *Acoustic and Radio EeV Neutrino Detection Activities (ARENA 2005)*, World Scientific Publishing, Singapore, Int. J. Mod. Phys. **A21** (2006)
- [17] L.F. Thompson (Ed.), *ARENA 2006 – Acoustic and Radio EeV Neutrino Detection Activities*, IOP Publishing, Philadelphia, J. Phys. Conf. Ser. **81** (2007)
- [18] K. Graf et al., *Testing Thermo-Acoustic Sound Generation in Water with Proton and Laser Beams*, in *Acoustic and Radio EeV Neutrino Detection Activities (ARENA 2005)*, ed. R. Nahnauer and S. Böser, Int. J. Mod. Phys. **A21** (2006) p. 127
- [19] K. Graf, *Teststrahlmessungen zur akustischen Neutrinodetektion: Thermoakustische Schallerzeugung in Wasser*, Diplomathesis, Univ. Erlangen-Nürnberg, (2004, FAU-PI1-DIPL-04-002)
- [20] S. Schwemmer, *Testmessungen zur akustischen Neutrinodetektion mit einem Nd:YAG-Lase*, Diplomathesis, Univ. Erlangen-Nürnberg, (2005, FAU-PI1-DIPL-05-002)
- [21] G.A. Askariyan, *Hydrodynamic Radiation From the Tracks of Ionizing Particles in Stable Liquids*, Sov. J. At. En. **3** (1957) p. 921
- [22] G.A. Askariyan, B.A. Dolgoshein et al., *Acoustic Detection of High Energy Particle Showers in Water*, Nucl. Instrum. Methods **164** (1979) p. 267
- [23] J.G. Learned, *Acoustic Radiation by Charged Atomic Particles in Liquids: An Analysis*, Phys. Rev. **19** (1979) p. 3293
- [24] L. Sulak, T. Armstrong et al., *Experimental Studies of the Acoustic Signature of Proton Beams Traversing fluid media*, Nucl. Instrum. Methods **161** (1979) p. 203
- [25] L.D. Landau and E.M. Lifshitz, *Course of Theoretical Physics, Vol. 6: Fluid Mechanics* (Pergamon Press, Oxford, 1959)
- [26] S.D. Hunter, W.V. Jones et al., *Acoustic Signals of Nonthermal Origin from High Energy Protons in Water*, J. Acoust. Soc. Am. **69** (1981) p. 1557
- [27] S.D. Hunter, W.V. Jones et al., *Nonthermal Acoustic Signals from Absorption of a Cylindrical Laser Beam in Water*, J. Acoust. Soc. Am. **69** (1981) p. 1563
- [28] V.I. Albul, V.B. Bychkov et al., *Measurements of the Parameters of the Acoustic Radiation Accompanying the Moderation of an Intense Proton Beam in Water*, Instr. Exp. Tech. **44** (2001) p. 327

- [29] V.B. Bychkov et al., *Experimental Study of the Acoustic Field Generated by a 50 MeV Electron Beam in Water*, arXiv:physics/0610241 (2006)
- [30] V.S. Demidov et al., *ITEP Investigation of Acoustic Phenomena from High Energy Particles*, in *Acoustic and Radio EeV Neutrino Detection Activities (ARENA 2005)*, ed. R. Nahnauer and S. Böser, Int. J. Mod. Phys. **A21** (2006) p. 122
- [31] A. Capone and G. de Bonis, *Preliminary Results on Hydrophones Calibration with Proton Beam*, in *Acoustic and Radio EeV Neutrino Detection Activities (ARENA 2005)*, ed. R. Nahnauer and S. Böser, Int. J. Mod. Phys. **A21** (2006) p. 112
- [32] N. Bilaniuk and G.S.K. Wong, *Speed of sound in pure water as a function of temperature*, J. Acoust. Soc. Am. **93** (1993) p. 1609
- [33] K. Mecke, 2008, private communication
- [34] J. Vandenbroucke, G. Gratta and N. Lehtinen, *Experimental Study of Acoustic Ultra-high-Energy Neutrino Detection*, Astrophys. J. **621** (2005) p. 301, arXiv:astro-ph/0406105
- [35] V. Niess and V. Bertin, *Underwater Acoustic Detection of Ultra High Energy Neutrinos*, Astropart. Phys. **26** (2006) p. 243, arXiv:astro-ph/0511617v3
- [36] S. Bevan et al., *Simulation of Ultra High Energy Neutrino Interactions in Ice and Water*, Astro. Part. Phys. **28** (2007) p. 366, arXiv:astro-ph/0704.1025v1
- [37] L.D. Landau and I.J. Pomeranchuk, *Electron-cascade processes at very high energies*, Dokl. Akad. Nauk SSSR **92** (1953) p. 735
- [38] A.B. Migdal, *Bremsstrahlung and Pair Production in Condensed Media at High Energies*, Phys. Rev. **103** (1956) p. 1811
- [39] A.V. Butkevich, L.G. Dedenko et al., *Prospects for Radio-wave and Acoustic Detection of Ultra- and Superhigh-Energy Cosmic Neutrinos*, Phys. Part. Nucl. **29** (1998) p. 266
- [40] F.H. Fisher and V.P. Simmons, *Sound Absorption in Sea Water*, J. Acoust. Soc. Am. **62** (1977) p. 558
- [41] M.A. Ainslie and J.G. McColm, *A simplified formula for viscous and chemical absorption in sea water*, J. Acoust. Soc. Am. **103** (1998) p. 1671
- [42] R.J. Urick, *Principles of Underwater Sound* (Peninsula publishing, Los Altos, USA, 1983)
- [43] R.J. Urick, *Ambient Noise in the Sea* (Peninsula publishing, Los Altos, USA., 1986)
- [44] J.A. Nystuen et al., *Underwater Sound Generated by Heavy Rainfall*, J. Acoust. Soc. Am. **93** (1993) p. 3169
- [45] Intergovernmental Oceanographic Commission, <http://ioc.unesco.org>

- [46] V.O. Knudsen, R.S. Alford and J.W. Emling, *Underwater ambient noise*, J. Mar. Res. **3** (1948) p. 410
- [47] N.G. Lehtinen et al., *Sensitivity of an Underwater Acoustic Array to Ultra-high Energy Neutrinos*, Astropart. Phys. **17** (2002) p. 279, arXiv:astro-ph/0104033
- [48] C.L. Naumann, *Development of Sensors for the Acoustic Detection of Ultra High Energy Neutrinos in the Deep Sea*, Doctoral Thesis, Univ. Erlangen-Nürnberg, (2007)
- [49] J. Perkin, *ACoRNE Simulation Work*, in *Acoustic and Radio EeV Neutrino Detection Activities (ARENA 2005)*, ed. R. Nahnauer and S. Böser, Int. J. Mod. Phys. **A21** (2006) p. 207
- [50] The IceCube homepage, <http://icecube.wisc.edu/>
- [51] The KM3NeT homepage, <http://www.km3net.org/>
- [52] Francis Halzen and Dan Hooper, *IceCube-Plus: an ultra-high-energy neutrino telescope*, JCAP **01** (2004), arXiv:astro-ph/0310152v3
- [53] J.A. Vandenbroucke et al., *Simulation of a Hybrid Optical/Radio/Acoustic Extension to IceCube for EeV Neutrino Detection*, in *Acoustic and Radio EeV Neutrino Detection Activities (ARENA 2005)*, ed. R. Nahnauer and S. Böser, Int. J. Mod. Phys. **A21** (2006) p. 259, arXiv:astro-ph/0512604
- [54] M. Neff, *Studie zur akustischen Teilchendetektion im Rahmen des ANTARES-Experiments: Entwicklung und Integration von Datennahmesoftware*, Diplomathesis, Univ. Erlangen-Nürnberg, (2007, FAU-PI1-DIPL-07-003)
- [55] F. Deffner, *Studie zur akustischen Neutrinodetektion: Analyse und Filterung akustischer Daten aus der Tiefsee*, Diplomathesis, Univ. Erlangen-Nürnberg, (2007, FAU-PI1-DIPL-07-001)
- [56] The ANTARES Collaboration, *A Deep Sea Telescope for High Energy Neutrinos*, arXiv:astro-ph/9907432 (1999)
- [57] P.A. Cherenkov, *Visible Emission of Clean Liquids by Action of Radiation*, Dokl. Akad. Nauk SSSR **2** (1934) p. 451, reprint: Usp. Fiz. Nauk **93** (1967), 385
- [58] The AMANDA homepage, <http://amanda.uci.edu/>
- [59] The ANTARES homepage, <http://antares.in2p3.fr/>
- [60] The BAIKAL homepage, <http://www.ifh.de/baikal/baikalhome.html>
- [61] The NEMO homepage, <http://nemoweb.lns.infn.it/>
- [62] The Nestor homepage, <http://www.nestor.org.gr/>

- [63] R. Lahmann et al., *Integration of Acoustic Detection Equipment into ANTARES*, in *Acoustic and Radio EeV Neutrino Detection Activities (ARENA 2005)*, ed. R. Nahnauer and S. Böser, Int. J. Mod. Phys. **A21** (2006) p. 227
- [64] J.A. Aguilar et al., *Study of large hemispherical photomultiplier tubes for the ANTARES neutrino telescope*, Nucl. Instrum. Methods **A 555** (2005) p. 132
- [65] P. Amram et al., *The ANTARES optical module*, Nucl. Instrum. Methods **A 484** (2001) p. 369
- [66] J.A. Aguilar et al., *First results of the Instrumentation Line for the deep-sea ANTARES neutrino telescope*, Astropart. Phys. **26** (2006) p. 314, arXiv:astro-ph/0606229
- [67] R. Lahmann, *Description of the Instrumentation Line 2007 (IL07)*, ANTARES internal note 3-INS-05-09-A, 2007
- [68] V. Niess, *Underwater acoustic positioning in Antares*, in *29th International Cosmic Ray Conference, Pune*, **5** (2005) p. 155
- [69] M. Ageron et al., *The Antares optical beacon system*, Nucl. Instrum. Methods **A 578** (2007) p. 498
- [70] J.A. Aguilar et al., *The data acquisition system for the ANTARES neutrino telescope*, Nucl. Instrum. Methods **A 570** (2007) p. 107
- [71] P. Amram et al., *Background light in potential sites for the ANTARES undersea neutrino telescope*, Astropart. Phys. **13** (2000) p. 127, arXiv:astro-ph/9910170
- [72] F. Feinstein et al., *The analogue ring sampler: A front-end chip for ANTARES*, Nucl. Instrum. Methods **A 504** (2003) p. 258
- [73] R. Lahmann et al., *Proposal for the Integration of Acoustic Sensors into the ANTARES Experiment*, ANTARES internal note ANTARES-PHYS-2007-008, 2007
- [74] L.F. Thompson, *The Acoustic Detection of Ultra-High Energy Neutrinos - a Status Report*, in *Proceedings of the TeV Particle Astrophysics II Workshop*, ed. F. Halzen et al., IOP Publishing, Philadelphia, J. Phys. Conf. Ser. **60** (2007) p. 52
- [75] M. Ageron et al., *Studies of a full scale mechanical prototype line for the ANTARES neutrino telescope and tests of a prototype instrument for deep-sea acoustic measurements*, Nucl. Instrum. Methods **A 581** (2007) p. 695
- [76] K. Graf et al., *Integration of Acoustic Neutrino Detection Methods into ANTARES*, in *Proceedings of the ARENA 2006 (Acoustic and Radio EeV Neutrino Detection Activities) Conference*, ed. L.F. Thompson, J. Phys. Conf. Ser. **81** (2007)

- [77] K. Graf et al., *Towards Acoustic Detection of UHE Neutrinos in the Mediterranean Sea - The AMADEUS Project in ANTARES*, in *Proceedings of the TeV Particle Astrophysics II Workshop*, ed. F. Halzen et al., J. Phys. Conf. Ser. **60** (2007) p. 296
- [78] K. Salomon, *Simulation und Messung verschiedener Hydrophonkomponenten zur akustischen Teilchendetektion*, Doctoral Thesis, Univ. Erlangen-Nürnberg, (2007)
- [79] C. Richardt, *Acoustic Particle Detection: Strategies for data reduction and source reconstruction*, Diplomathesis, Univ. Erlangen-Nürnberg
- [80] G. Anton et al., *Study of piezo based sensors for acoustic particle detection*, *Astropart. Phys.* **26** (2006) p. 301
- [81] P. Kollmannsberger, *Studien zur akustischen Detektion ultrahochenergetischer Neutrinos mit Hilfe des piezoelektrischen Effekts*, Diplomathesis, Univ. Erlangen-Nürnberg
- [82] High Tech, Inc., <http://home.att.net/~hightechinc/>
- [83] C. Richardt and R. Lahmann, *Assembly and Metrology of the Acoustic Storeys on the IL07*, ANTARES internal note 3-INS-07-01-A, January 2008
- [84] R. Lahmann, *Specifications of the Acoustic ADC and Data Processing Board (AcouADC Board)*, ANTARES internal note 3-INS-07-02, 2007
- [85] GCD Printlayout GmbH, <http://www.gcd-printlayout.de/>
- [86] K. Graf and R. Lahmann, *Power Consumption of the AcouADC Board*, ANTARES internal note 3-INS-07-03, 2007
- [87] Centre de Calcul de l'Institut National de Physique Nucléaire et de Physique des Particules, [cc.in2p3.fr](http://cc.in2p3.fr)
- [88] J. Doernberg et al., *Full-Speed Testing of A/D Converters*, *IEEE J. SC* **12** (1984) p. 820
- [89] R.C. Martins and A.M. da Cruz Serra, *Automated ADC Characterization Using the Histogram Test Stimulated by Gaussian Noise*, *IEEE Trans. Instr. Meas.* **48** (1999) p. 471
- [90] N. Björnsell and P. Händel, *Truncated Gaussian noise in ADC histogram tests*, *Meas.* **40** (2007) p. 36
- [91] The Institute of Electrical and Electronics Engineers, Inc., *IEEE Standard for Terminology and Test Methods for Analog-to-Digital Converters*, *IEEE Std 1241-2000*, 2001
- [92] S.D. Stearns and D.R. Hush, *Digital Signal Analysis* (R. Oldenbourg Verlag, München Wien, 7<sup>th</sup> edition, 1999)
- [93] A.V. Oppenheim, R.W. Shafer and J.R. Buck, *Discrete-Time Signal Processing* (Prentice-Hall, Englewood Cliffs, second edition, 1999)

- [94] Linear Technology Corporation, *Linear Phase, DC Accurate, Tunable, 10th Order Lowpass Filter (LTC 1569-7)*, 1998, sn15697, available at <http://www.linear-tech.com>
- [95] Xilinx, Inc., *XILINX LogiCORE FIR Compiler v1.0*, 2006, DS534, available at <http://www.xilinx.com>
- [96] MAXIM, *The ABCs of ADCs: Understanding How ADC Errors Affect System Performance*, Maxim Integrated Products, 2007, Appnote 748, available at [http://www.maxim-ic.com/appnotes.cfm/appnote\\_number/748/](http://www.maxim-ic.com/appnotes.cfm/appnote_number/748/)
- [97] Burr-Brown Products from Texas Instruments, *16-Bit, 500kSPS, microPower Sampling ANALOG-TO-DIGITAL CONVERTER (ADS8323)*, 2001, SBAS224B, available at <http://www.ti.com>
- [98] R. Mancini, *Op Amps For Everyone*, Texas Instruments Inc., 2002, SLOD006B, available at <http://www.ti.com>
- [99] *Electromagnetic compatibility (EMC) - Part 4: Test and measuring methods - Main section 6: Cable-propagated interference factors, induced by high frequency fields*, 1996, Norm No. DIN EN 61000-4-6, IEC 61000-4-6:1996
- [100] S.A. Fry, *Department of Defense Dictionary of Military and Associated Terms*, Department of Defense, USA, 2007, JP 1-02, available at <http://www.dtic.mil/doctrine/jel/doddict>
- [101] The CPPM homepage, <http://marwww.in2p3.fr/>
- [102] The IFREMER homepage, <http://www.ifremer.fr/>
- [103] N. Kurahashi and G. Gratta, *High-Frequency Ambient Noise as Background to Deep Ocean Transient Signal Detection*, arXiv:astro-ph/0712.1833v1 (2007)
- [104] J.R. Short, *High-Frequency Ambient Noise and Its Impact on Underwater Tracking Ranges*, IEEE J. Ocean. Eng. **30** (2005) p. 267





# Danksagung

Ich möchte mich bei allen bedanken, die mich bei meiner Dissertation unterstützt und damit diese Arbeit möglich gemacht haben; leider kann ich nicht alle Beteiligten namentlich aufführen. All diejenigen, die ich nicht erwähnen konnte, mögen dies verzeihen.

An erster Stelle bedanke ich mich bei Prof. Dr. Uli Katz dafür, dass er mir die Arbeit an diesem spannenden Thema ermöglichte und trotz all seines Arbeitspensums stets Zeit und Anregungen für mich fand. Prof. Dr. Klaus Helbing hat sich freundlicherweise bereit erklärt, das Zweitgutachten zu meiner Arbeit zu verfassen, wofür ich ihm herzlich danke.

Außerdem danke ich allen Mitgliedern der Akustik-Gruppe des ECAP; nur durch den Einsatz und die Begeisterung aller war es uns möglich AMADEUS so erfolgreich aufzubauen und zu betreiben. Auch wenn ich eigentlich keine Einzelpersonen herausstellen möchte, muss doch das AMADEUS-Kernteam um Dr. Robert Lahmann, Dr. Jürgen Höbl, Dr. Christopher Naumann, Carsten Richardt und Max Neff erwähnt werden. Besonders muss ich mich bei Dr. Robert Lahmann bedanken. Ohne ihn wären weder der Inhalt der Arbeit noch die Arbeit selbst in dieser Art gelungen. Herrn Dr. Timo Karg gebührt herzlicher Dank für die Simulationsarbeiten und Friederike Schöck für die Auswertung der AMADEUS\_0 Daten. Beide Studien haben Grundlagen und viele Denkansätze für diese Arbeit geliefert. Stefanie Schwemmer danke ich für die gemeinsame Arbeit an der Signalerzeugung im Labor.

Den gesamten Mitgliedern der Erlanger Astroteilchen-Gruppe und dem zur Zeit in Amerika weilenden Dr. Alexander Kappes danke ich für die gute Arbeitsatmosphäre und die interessante und schöne Zeit, die wir zusammen verbringen durften. Für das sorgfältige Korrekturlesen danke ich Felix Fehr und Dr. Bettina Hartmann.

Mein besonderer Dank gilt meiner Familie, die mich bei meiner Dissertation stets mit vollem Einsatz unterstützt hat. Für die logistische und vor allem die moralische Unterstützung während der Anfertigung dieser Arbeit kann ich Bettina Hartmann gar nicht genug danken. Ohne ihren Beistand wäre die Arbeit kaum zu schaffen gewesen.

I would like to thank all the colleagues of the ANTARES collaboration. They have created an always friendly and fruitful atmosphere to work in together. My special thanks go to Dr. Vincent Bertin and Dr. Valentin Niess.



# Lebenslauf

---

## Persönliches

---

Name: Kay Graf  
Adresse: Gerhart-Hauptmann-Straße 11, 91058 Erlangen  
Telefon: 09131 - 804149  
E-Mail: kay.graf@physik.uni-erlangen.de  
Geburtsdatum: 19. Dezember 1977  
Geburtsort: Fürth

---

## Bildung

---

*Universität Erlangen-Nürnberg*  
**Promotionsstudium** 2004 – 2008  
am Physikalischen Institut I bei Prof. Dr. U. Katz  
**Diplomarbeit** 2003 – 2004  
Thema: „Teststrahlungsmessungen zur akustischen Neutrinodetektion“  
am Physikalischen Institut I bei Prof. Dr. U. Katz  
**Studium** 1998 – 2004  
Studienfach: Physik mit Studienziel Diplom (Univ.)  
Diplom mit Gesamtnote 1,05 2004  
Vordiplom mit Gesamtnote 1,15 2000

*Imperial College of Science London, Großbritannien*  
**Auslandssemester** 2000 – 2001  
gefördert durch das EU SOKRATES/ERASMUS Program

*Willibald-Gluck-Gynasium Neumarkt i.d.Opf.*  
**Schulbildung** 1988 – 1997  
Abitur mit Gesamtnote 1,6 1997

---

## Praktika und Preise

---

**Promotionsstipendium** 2006 – 2008  
gefördert durch die Studienstiftung des Deutschen Volkes

**Ohm Preis** 2005  
Preis für die beste Diplomarbeit im Bereich Physik

**Helmholtz-Nachwuchspreis für Astroteilchenphysik** 2004  
Preis für die beste Diplomarbeit im Gebiet der Astroteilchenphysik

*DESY Hamburg*  
**Sommerstudent** 2002  
Teilnahme am *International Summer Student Program*